Lithogeochemistry and Hydrothermal Alteration of the Pine Cove Orogenic Gold Deposit, Baie Verte Peninsula, Newfoundland, Canada

By Samuel Ybarra

A Thesis submitted to the School of Graduate Studies in partial fulfillment of the requirements for the degree of

Master of Science, Department of Earth Sciences

Memorial University of Newfoundland

2020

St. John's, Newfoundland and Labrador

Abstract

The Pine Cove gold mine is hosted within Ordovician gabbro sills and volcano-sedimentary rocks of the Venam's Bight and Bobby Cove formations, Snooks Arm Group, Baie Verte Peninsula, Newfoundland Appalachians, Canada. The deposit is located approximately 50 to 200 m above the Scrape thrust fault, a brittle-ductile structure associated with Silurian transpression. Gold mineralization occurs as microscopic native Au inclusions in pyrite disseminated in the selvages of quartz-calcite-chlorite±albite breccia-veins. Multiple generations of overlapping veins are enveloped by sericite-rutile-calcite-pyrite alteration selvages.

Mineralized quartz breccia veins are most abundant at the contacts of gabbro sills and volcanosedimentary strata. Ore-grade mineralization predominantly occurs within Fe-rich gabbros and basalts of the Venam's Bight Formation. These relationships suggest that there were two fundamental controls on mineralization: 1) hydrofracturing assisted by anisotropic deformation of rigid gabbro sills within more ductile country rocks; and 2) sulfidation of the Fe-rich gabbros and basalts. Comparatively, the volcaniclastic rocks of the Bobby Cove Formation lack abundant gabbro intrusions and are relatively Fe-poor, and were thus a less receptive host rock to gold mineralization at Pine Cove.

Three distinct alteration assemblages are identified at Pine Cove: proximal sericite-rutile-chlorite-calcite, intermediate carbonate-chlorite, and distal epidote-titanite-chlorite-calcite. Mass balance calculations for altered wall rock show enrichments in CO_2, K_2O, S, Rb, W, In, Pb, Bi, Te, Se, Cs, and Ba, and depletions in As, Sb, and Na_2O. REE, HFSE, Al_2O_3, and most transition metals were generally immobile during alteration. There are distal to proximal elemental variations in relation to gold mineralization, and the generalized sequence of geochemical variation includes (from distal to proximal - 50m to 1m): CO_2 enrichment + As-Sb depletion → K-Rb enrichment → Na depletion → W±Pb±Ba enrichment → Au. The alkali-carbonate index $K_2O + CO_2$ / $K_2O + CO_2 + Na_2O + Al_2O_3$ coupled with As-Sb depletion is considered the most consistent metric of ore-related alteration at Pine Cove.

Combined short wave infrared (SWIR) spectrometry and electron microprobe analysis (EMPA) of white micas show that Tschermak substitution ($Al^{VI} + Al^{IV} \leftrightarrow [Fe^{2+},Mg]^{VI} + Si^{IV}$) and K/Na content correlate with AlOH absorption wavelengths. White mica compositions progress from phengite → paragonitic muscovite → muscovite approaching mineralization. A new potential SWIR index for orogenic gold exploration in greenschist facies rocks is the quantity Fe^{2+} slope/MgOH-depth extracted from reflectance spectra of altered rock. At Pine Cove, this index measures the relative proportion of (Fe-carbonate + sericite)/chlorite, and correlates with the alkali-carbonate alteration index $K_2O + CO_2/K_2O + CO_2 + Na_2O + Al_2O_3$ and Au mineralization. Although the physico-chemical conditions during mineralization in orogenic gold deposits may vary from deposit to deposit, the collective visual, geochemical, and SWIR indices identified at Pine Cove represent potential vectoring tools for the discovery of similar deposits in orogenic Au camps globally.

Acknowledgements

This thesis has been greatly improved through the help of many individuals. First and foremost, I would like to thank my advisor, Dr. Stephen Piercey, for his endless support. His enthusiasm and humor helped make this a thoroughly enjoyable project, and continually increased my interest in understanding orogenic gold deposits. I appreciate his patience and the amount of time he spent providing advice and mentorship to me.

I would also like to thank Dr. Graham Layne for being a patient, helpful, and enlightening advisor. He was always available to discuss my project whenever I had questions and taught me a great deal about mineralogy and microanalytical techniques. Many thanks to all my peers within the geology department and colleagues who provided valuable advice and very insightful conversations.

This project was made possible by Anaconda Mining Inc., who provided logistical support and allowed me to study the Pine Cove deposit. Specifically, I would like to thank Paul McNeil and Dave Copeland, who provided critical resources and insights, and were instrumental in directing this project.

Financial support for this project was provided by Anaconda Mining, Inc. and the GeoExplore program from the Research and Development Corporation of Newfoundland and Labrador (RDC). Dr. Piercey is also supported by an NSERC Discovery Grant.

Last but certainly not least, I would like to thank all my family and friends; you have all kept me positive and sane throughout this process. My parents, Jerry and Sharon, have provided never-ending support. I would also like to thank my partner, Sarah, whose patience and encouragement have greatly helped me in this endeavor.

Table of Contents

List of Tables and Figures

Tables

Chapter 2

Figures

Chapter 1

Chapter 2

List of Abbreviations

ab	albite
ACI	alkali + carbonate alteration index
amyg	amygdaloidal
ank	ankerite
ap	apatite
apfu	atom per formula unit
BCF-ABLT	Bobby Cove Formation amygdaloidal basalt lapilli tuff
BCF-CCLT	Bobby Cove Formation clinopyroxene crystal-lapilli tuff
BDL	below detection limit
BSE	back scattered electron
BVBL	Baie Verte-Brompton Line
BVOT	Baie Verte Oceanic Tract
BVP	Baie Verte Peninsula
CAB	calc-alkaline basalt
cal	calcite
carb	carbonate
chl	chlorite
cp	chalcopyrite
cpx	clinopyroxene
CV_{avg}	average coefficient of variation
E-MORB	enriched mid ocean ridge basalt
epid	epidote
Fm	Formation
g/t	grams per ton
HFSE	high field strength element
HQ	hull quotient
IAB	island arc basalt
ICP-AES	Inductively coupled plasma atomic emission spectroscopy
ICP-MS	inductively coupled plasma mass spectrometry
ilm	ilmenite
km	kilometer
LOI	loss on ignition
LKT	low-K tholeiite
mag	magnetite
m	meter

mm	milimeter
mol	molar
nm	nanometer
N-MORB	normal mid ocean ridge basalt
OFB	ocean floor basalt
OIB	ocean island basalt
po	pyrrhotite
ppm	parts per million
py	pyrite
qz	quartz
RD	relative difference
REE	rare earth element
RSD	relative standard deviation
rt	rutile
SEM	scanning electron microscope
ser	sericite
SWIR	short wave infrared
Ti-mag	titaniferous magnetite
tit	titanite
VBF	Venam's Bight Formation
wt %	weight percent

List of Appendices

Chapter 1: Introduction to the Pine Cove orogenic gold deposit, Baie Verte Peninsula, Newfoundland, Canada

The Baie Verte Peninsula, Newfoundland is host to numerous orogenic gold occurrences (Evans, 2004). While the geology of orogenic gold deposits in the Baie Verte Peninsula has been summarized by Evans (2004), hydrothermal alteration patterns and the lithostratigraphy of these deposits have not been comprehensively documented. It is therefore difficult to assess factors that influenced the formation of these deposits or apply alteration models during exploration in the district. In light of recent tectonostratigraphic studies on the Baie Verte Peninsula (Skulski et al., 2010) and global models for orogenic gold deposits (e.g., Dubé and Gosselin, 2007), characterization of alteration patterns and the stratigraphic setting of mineralization could significantly improve exploration targeting in the region. Studies of hydrothermal alteration around orogenic gold deposits in other terrains have defined mineralogical and geochemical criteria (e.g., anomalous CO_2, K, S, As and Sb) useful for exploration target evaluation (Bierlein, 2000; Eilu and Groves, 2001; Eilu et al., 2001; Christie & Braithwaite, 2003), and it is anticipated that this will prove effective on the Baie Verte Peninsula, as well.

Gold mineralization on the Baie Verte Peninsula is hosted predominantly in Ordovician ophiolite rocks and submarine volcano-sedimentary rocks of the Baie Verte oceanic tract (Evans, 2004; van Staal, 2007). Significant deposits and prospects include: Pine Cove (Dimmell and Hartley, 1991), Deer Cove (Patey and Wilton, 1993), Romeo & Juliet (Meade et al., 1997), and Stog'er Tight (Ramezani, 2002). This study characterizes wall-rock alteration and lithostratigraphy at the currently-operating Pine Cove deposit. As an economically viable deposit, Pine Cove presents an excellent case study to evaluate the alteration patterns and stratigraphic setting of gold mineralization. Owned and operated by Anaconda Mining Inc., resource estimates as of 2017 were 863,500 tonnes @ 2.07 g/t Au Indicated and 476,300 tonnes @ 1.39 g/t Au Inferred (Cullen et al., 2017). Previous production is 118, 028 ounces of gold from 2,511,000 tonnes of ore since 2011 (Anaconda Mining Inc. internal reporting). The structure and geology of the deposit have been described by Dimmell and Hartley (1991) and Duncan and Graves (1992), but no detailed studies of the lithology, mineralogy, or geochemistry of the deposit have previously been conducted.

Objectives of this study are to use a multi-method approach involving core logging, mapping, lithogeochemistry, mineral spectroscopy, petrography, scanning electron microscopy (SEM), and electron microprobe analysis (EMPA) to: 1) characterize host rock composition, chemistry, and stratigraphy; 2) characterize the mineralogy, chemistry, and extent of wall-rock alteration as a function of lithology and distance to ore; 3) develop a model of alteration patterns constructed upon a primary lithologic framework; and 4) define mineralogical and geochemical criteria useful for exploration target evaluation. The following sections provides an overview of orogenic gold deposits, geologic setting of the deposit, and methods of the proposed research for this thesis.

1.1 Orogenic Gold Deposits

The Pine Cove gold deposit has characteristics typical of greenstone-hosted quartz-carbonate vein (also called orogenic, mesothermal, or lode gold) deposits (Evans, 2004;

Dubé and Gosselin, 2007) herein referred to as orogenic gold deposits after Groves et al. (1998). The following summary of orogenic gold deposits is based upon the syntheses of Groves et al. (1998), Poulsen et al. (2000), and Dubé & Gosselin (2007).

Orogenic gold deposits are structurally controlled, epigenetic gold deposits typically hosted in deformed greenschist-facies (greenstone) metamorphic belts. They are characterized by quartz-carbonate ± gold veins within brittle-ductile shear zones and faults. These faults and shear zones are commonly second-order structures that are splays off major crustal-scale faults. The controlling structures of vein systems are highly variable in type and geometry. Fault-fill, stockwork, and/or hydrothermal breccia veins may form dependent on the geological and structural setting. Internal stress regimes produced by layer anisotropy or competency contrast, such as rigid sill bodies surrounded by softer sedimentary rocks, can also significantly influence the type, geometry, and localization of vein systems.

Orogenic Au deposit vein mineralogy is dominantly quartz, with lesser amounts of carbonate (ankerite, dolomite, siderite, and calcite) and sulfide minerals. Variable amounts of white mica, chlorite, tourmaline, and scheelite may also comprise vein fill. Mineralization occurs predominantly as native gold, with decreasing amounts of auriferous pyrite, pyrrhotite, and chalcopyrite. Arsenopyrite commonly occurs in metasedimentary or amphibolitic rocks. Sulfides can occur in the veins and/or within the surrounding host rock. Ore geochemical signatures can exhibit enrichments in As, Ag, B, Bi, Hg, Sb, Te, and W, with only slightly elevated Cu, Pb, and Zn.

Wall-rock alteration mineral assemblages vary by composition, competence, and metamorphic grade of the host lithology. Typical alteration assemblages within greenschist-facies rocks proximal to veins include sericite, carbonate, chlorite, pyrite, and albite. Distal alteration assemblages comprise chlorite, calcite, and sometimes magnetite. At deeper crustal levels (including amphibolite-facies rocks), alteration assemblages can consist of amphibole, biotite, diopside, garnet, pyrite and/or arsenopyrite. Chromium- or vanadium-rich green micas are common alteration products in, or proximal to, ultramafic rocks. Alteration geochemical patterns include enrichment of CO_2, K_2O, S, H_2O, SiO_2, and large-ion lithophile elements (LILE). Either leaching or addition of Na_2O may also occur in alteration zones.

Although currently a subject of debate, the ore-forming fluids are commonly interpreted to have been derived from crustal dehydration of subducted volcano-sedimentary terranes during prograde metamorphism (Jia et al., 2003; Pitcairn et al., 2006; Mernagh and Bierlein, 2008; Phillips and Powell, 2010; Goldfarb and Groves, 2015; Pitcairn et al., 2015). These metamorphic fluids become mobilized along major faults or deformation zones to higher crustal levels; in turn dissolving and scavenging various components, notably gold, from country rock along flow pathways. Alternative models emphasize the influence of magmatic activity, either as a source of the fluids (Xue et al., 2013) or the thermal engine that drives fluid circulation (Goldfarb and Groves, 2015).

Ore-forming fluids are generally low salinity, near neutral, $H_2O\text{-}CO_2 \pm CH_4$ fluids. At temperatures below 350°C, gold is transported as HS^- complexes, either $Au(HS)^o$ or $Au(HS)_2^-$; whereas $AuCl_2^-$ predominates at higher temperatures (Mikucki, 1998; Williams-

Jones et al., 2009). Gold deposition occurs due to changes in physicochemical conditions, such as pH, oxygen fugacity (fO_2), pressure, or the sulfidation of iron-bearing minerals in wall rocks, resulting in decreased activity of HS^- (Williams-Jones et al., 2009).

1.2 Regional Geology and Tectonic Evolution

Williams (1979) identified four tectonostratigraphic zones within Newfoundland; these are the Avalon, Gander, Dunnage, and Humber zones from east to west, respectively (Fig. 1.1a). Each zone represents spatially and geologically distinct terranes that were sutured together during the Appalachian orogenesis. The amalgamation of these tectonostratigraphic zones is the result of diachronous Paleozoic accretionary orogenies during the closing of the Iapetus and Rheic Oceans; which culminated in the collision of Laurentia and Gondwana to form the supercontinent Pangea (van Staal, 2007; van Staal and Barr, 2012).

The Humber Zone represents the ancient North American passive continental margin onto which subsequent terranes were accreted (Williams, 1979; Williams et al., 1999). The Dunnage Zone is comprised of vestiges of oceanic and continental arc terranes developed within the ancient Iapetus Ocean, and is further subdivided into the peri-Laurentian Notre Dame subzone and peri-Gondwanan Exploits subzone, to distinguish between terranes formed on opposite sides of Iapetus (Williams, 1979; Williams et al., 1988). Notre Dame subzone terranes were accreted to the Laurentian margin during the Cambrian-Ordovician Taconic orogeny, whereas Exploits subzone terranes were accreted to the Gander margin during the overlapping Ordovician Penobscot orogeny (van Staal and

Barr, 2012). The Gander and Avalon zones are interpreted to represent outboard peri-Gondwanan microcontinents that were accreted to the composite Laurentian margin during the Silurian Salinic and Devonian Acadian orogenies, respectively (Williams et al., 1999; van Staal and Barr, 2012).

1.3 Geology of the Baie Verte Peninsula

The Baie Verte Peninsula straddles a suture belt between the Humber Zone and Notre Dame subzone, termed the Baie Verte-Brompton Line, or simply Baie Verte Line (BVL) in Newfoundland (Fig. 1.1b). The Baie Verte-Brompton Line extends through much of the Canadian Appalachians as a belt of disrupted ultramafic bodies and mélanges along a steeply-dipping structural zone interpreted to represent the tectonic interface between the Laurentian continent and the Iapetus ocean (Williams and St. Julien, 1982). On the Baie Verte Peninsula, the BVL is a north-northeast to east trending fault zone that juxtaposes oceanic terranes of the Notre Dame Subzone against continentally-derived rocks of the Humber Zone (Hibbard, 1983).

To the west of the BVL, the Humber Zone consists predominantly of intensely deformed schists and gneisses of the Mesoproterozoic East Pond Metamorphic Suite overlain by metaclastic schists of the Hadrynian to Middle Ordovician Fleur de Lys Supergroup. East Pond Metamorphic Suite rocks are interpreted as supracrustal strata that were deposited on Grenvillian crystalline basement, and the Fleur de Lys Supergroup represents basin fill and submarine slope deposits along the continental margin (Hibbard, 1983; van Staal et al., 2013).

East of the BVL, the Notre Dame subzone consists of ophiolite complexes and volcano-sedimentary cover sequences of the Baie Verte oceanic tract (Hibbard, 1983; van Staal, 2007; van Staal and Barr, 2012)). The four ophiolite suites are identified as the Advocate Complex, the Point Rousse Complex, the Betts Cove Complex, and the Pacquet Harbour Group (Fig. 1.1b). Although the ophiolite suites are named individually, Hibbard (1983) considered them to be isolated remnants of a single generation of oceanic crust (see Local Stratigraphy below); this has been tested and confirmed using detailed petrology, geochemistry, and geochronology by Skulski et al. (2010). Terranes on both sides of the BVL are intruded by Ordovician to Silurian granitic to gabbroic intrusive rocks (Hibbard, 1983).

Castonguay et al. (2009) defined four deformation events that affected rocks on the Baie Verte Peninsula. The first deformation event (D_1) is mainly preserved as a micaceous schistosity in the Fleur de Lys Supergroup, but is mostly overprinted by later deformation elsewhere. This phase is associated with the obduction of the Baie Verte Oceanic Tract during the Taconic orogeny. Later-D_2 fabrics are associated with north-dipping, south-directed faults and shear zones. The D_2 deformation event is responsible for burial of ophiolites and exhumation of the Fleur de Lys Supergroup during Silurian Salinic sinistral transpression (Castonguay et al., 2009; Skulski et al., 2010). D_3 deformation is expressed as recumbent folds and south-dipping extensional shear zones; these are attributed to Devonian dextral transtension to transpression (Anderson et al., 2001). D_4 structures comprise crossfolds that are not uniformly developed across the peninsula.

Epigenetic gold mineralization in the Baie Verte Peninsula is spatially associated with brittle-ductile D_2 faults, such as the Scrape thrust and Deer Cove Sole Thrust (Dimmell and Hartley, 1991; Dube et al., 1993; Evans, 2004). Radiometric age determinations from various deposits and this spatial association between gold and Silurian D_2 faults suggests that gold mineralization was coeval with Silurian-Devonian orogenesis (Ritcey et al.,1995; Ramezani, 2002; Castonguay et. al, 2009; Kerr & Selby, 2011; Castonguay et. al, 2014).

1.4 Stratigraphy of the Betts Cove Ophiolite

The Betts Cove Complex and overlying Snooks Arm Group are the best preserved of the Ordovician oceanic terranes on the Baie Verte Peninsula. Skulski et. al (2010) established that the stratigraphy defined by Bedard et. al (2000) for the Betts Cove area can be used as a stratigraphic template for the other sequences on the peninsula. The units of the stratigraphic template as defined by Skulski et. al (2010, and references therein) are show in Figure 1.2, and their features are briefly summarized here in stratigraphic succession.

The lower ophiolite section is characterized by ultramafic cumulates overlain by gabbros, sheeted dykes, and low- to intermediate-Ti boninites. These rocks are overlain by the Mount Misery Formation, consisting of island-arc tholeiitic pillow basalts and intermediate-Ti boninites.

The lowest part of the Snooks Arm Group is the Scrape Point Formation, and is comprised of a local basal conglomerate cemented by jasper, overlain by red siltstones and iron-formation called the Nugget Pond, or Goldenville, horizon. These rocks are overlain by siltstone, greywacke, mafic tuffs, and tholeiitic, high-Ti basalt. The Bobby Cove Formation is composed of calc-alkaline volcanic rocks and volcaniclastic turbidites, and includes a lower distinctive clinopyroxene-phyric tuff termed the East Pond member. The Venam's Bight Formation consists of tholeiitic, high-Ti basalts with interbedded volcanic breccia and hematitic mudstone. The Balsam Bud Cove Formation dominantly consists of felsic tuff, rhyolite, tholeiitic basalt, and debris flow deposits, with lower mafic epiclastic rocks and black graptolitic shale. The Round Harbor Formation is composed of tholeiitic high-Ti basalt interbedded with minor chert.

Skulski et. al (2010) recognized similar stratigraphic sequences within the Point Rousse Complex, Advocate Complex, and the Pacquet Harbour Group, with local variations. Some of the formations within the cover sequences have similar volcanic components, but correlations can be made based on regionally extensive marker units, such as the East Pond member and Nugget Pond horizon, and the composition and geochemistry of the volcanic units. This template provides the framework to correlate the stratigraphic and structural position of the host rocks at Pine Cove.

1.5 Pine Cove Deposit Geology

The following is a summary of a report on the geology of the Pine Cove deposit by Dimmell and Hartley (1991). The host rocks at Pine Cove are greenschist-facies sedimentary and mafic volcanic and intrusive rocks of the Point Rousse Complex. The Point Rousse Complex has been thrust over greenschist-facies mafic to intermediate volcanic rocks of the Pacquet Harbour Group along the Scrape thrust fault. The Scrape thrust fault is a 30- to 35-degree northward dipping fault that follows an arcuate trend from northeast to east-southeast through the Pine Cove area (Fig. 1.3). Mineralized zones occur within the hanging wall of the Scrape thrust fault and are estimated to occur 50 to 200 m above this fault. Gold is associated with pyrite in quartz veins and disseminated pyrite in altered wall rock. Alteration consists of quartz and chlorite alteration. Quartz veins occur as a set of steeply-dipping, E-W striking dilational veins and a second set of massive to brecciated veins that dip moderately to steeply northward. The quartz veins are interpreted to be geometrically controlled by mixed brittle-ductile deformation developed from movement along the Scrape thrust.

A subsequent report by Duncan and Graves (1992) describes the lithology and alteration of the Pine Cove deposit in more detail. These authors separate seven lithologies within the Point Rousse Complex, irrespective of stratigraphic sequence. A brecciated and strongly contorted quartz-chlorite-carbonate unit lies directly above the Scrape thrust. Above this unit is an extensively carbonate-altered mafic volcanic unit inferred to be basalt, diabase, or a mafic tuff. Overlying and intercalated with the mafic volcanic rocks is a sequence of interbedded crystal-lithic volcaniclastic sedimentary rocks, red-purple argillite, and shale. These sedimentary rocks exhibit poor intrabed grading that indicate fining directions down hole in drill core (i.e., inverse grading). Leucoxene-bearing gabbroic sills intrude the above units. Low-angle quartz-chlorite breccia-veins cross-cut the mafic volcanic rocks, sedimentary sequence, and gabbro sills. These veins contain auriferous pyrite, albite, hematite, minor calcite, ankerite, and rare chalcopyrite. Alteration selvages of the quartz veins contain quartz, sericite, and locally albite alteration. Pervasive chlorite alteration is present in the wall rocks. The uppermost unit, with respect to surface, is comprised of mafic tuffs and flows, epidote altered lapilli tuff, amygdaloidal basalt, and epidote altered flow breccia.

Duncan and Graves (1992) concluded that mineralization is hosted predominantly within a main gabbro sill, suggesting that brittle fracturing and high Fe-content produced mechanically and chemically favorable conditions for pyrite formation and gold precipitation. The presence of albite was also suggested to correlate with strongly mineralized zones. It should be noted that all the above descriptions are based on macroscopic observations and did not include petrographic data.

A report by Wilton (1990) described limited petrographic and scanning electron microscopy results from some sections of mineralized zones. This work confirmed the presence of albite and that gold occurs as mono-elemental grains intergrown with pyrite and as fracture fillings.

1.6 Research Methodology

Core logging and mapping: A key component of this research involved detailed macroscopic descriptions and mapping of stratigraphic and intrusive units and alteration types. Examination of drill core and surface exposures were accomplished at the mine site and in the field. This work provided the foundation for lithogeochemistry, petrography, scanning electron microprobe (SEM), electron microprobe analysis (EMPA), and shortwave infrared (SWIR) spectroscopy studies. A total of 23 drill holes were logged for lithology, structure, alteration, and mineralization (Fig. 1.3). Drill holes were selected for logging to define key cross sections through the deposit and surface exposures were mapped within and lateral to the mine pit. Hand-written logs were created to document lithology, alteration, structure, and mineralization in drill core. A semi-quantitative scale (0 = absent to 4 = complete replacement of protolith minerals) was employed for recording the relative abundance of alteration minerals (e.g., chlorite, rutile) for ease of integration with geologic software.

Lithogeochemistry: Representative samples from drill core and surface were selected for whole rock and trace element chemistry analysis to characterize the signature of ore-grade mineralization, proximal alteration and distal alteration, and least-altered primary background for each rock type. A total of 253 core samples were collected at approximately 10 to 20 m intervals for geochemical analyses. Drill core samples were also augmented by 29 surface samples from areas of limited or no drilling. Samples were analyzed at ALS Inc. Geochemistry Laboratory in North Vancouver, Canada, with the complete characterization package (CCP-PKG01). This analysis package provides a comprehensive suite of major and trace elements, including the full rare earth element (REE) suite, using a combination of analytical methods. Major elements are provided from a lithium borate fusion, four-acid digestion, and inductively coupled plasma atomic emission spectroscopy (ICP-AES) analysis. Trace elements, including REEs, are acquired from a lithium borate fusion, four-acid digestion and inductively coupled plasma mass spectroscopy (ICP-MS) analysis. Base metals are reported from a four-acid digestion and ICP-AES finish, and volatile elements are acquired from an aqua regia digestion and ICP-MS analysis. Samples were analyzed for gold separately by fire assay and ICP-AES (Au-ICP21 package).

Representative samples were taken at generally no greater than 20 m intervals to acquire a downhole profile of each drill hole logged. Sampling targeted specific criteria, such as lithology, alteration type, alteration intensity, and/or mineralization. Standards were also analyzed every 20 samples to ensure accuracy and precision. Samples were cut and cleaned at the Pine Cove mine site, then shipped to the ALS Inc. laboratory.

Mineral spectroscopy: Hyperspectral data measurements of drill core were made concurrent with logging using an ASD, Inc. TerraSpec^{TM} mineral spectrometer that records spectra in the 350- to 2,500 nm wavelength range with a spectral resolution of 10 nm. Measurements were taken at 1 to 5 m intervals dependent on alteration and lithologic changes, and at every geochemical sample. A total of 827 sample measurements were collected using a contact probe to ensure consistent illumination conditions. Analysis targeted mostly areas of wall rock and vein alteration halos. Optimization was done at the start of every analysis run, and white references were collected every ~ 20 minutes to avoid drifts in data.

Absorption feature parameters (scalars) were extracted from reflectance and hull quotient-corrected spectra at Memorial University using The Spectral Geologist software. Scalars targeted absorption features related to white mica, chlorite, and carbonate. Scalars for epidote were created but not analyzed due to the low number of samples containing diagnostic 1550 nm absorption features. The scalar for the AlOH absorption feature position was created using a 5th-order polynomial fitting curve applied to the reflectance spectrum over the range 2174-2230 nm and focused between 2184-2224 nm. A spectral feature depth filter of 0.02% was applied to remove background noise. White mica crystallinity was calculated from the depth of the 2200 nm feature divided by the depth of the 1900 nm feature. The Fe-slope scalar was calculated from the mean value at 1650 nm divided by the mean value at 1350 nm taken from the reflectance spectrum.

Petrography, SEM and EPMA: 19 samples were selected to characterize lithology and alteration types and were sent to Vancouver Petrographics for fabrication of polished thin sections. The mineralogy and textures of the samples were examined and documented using a Nikon LV100POL petrographic microscope at Memorial University. SEM analysis were undertaken at Memorial University's CREAIT-Micro-Analysis Facility, Bruneau Centre for Research and Innovation, using the FEI MLA 650F SEM to examine finer-scale textures, trace minerals, and semi-quantitative mineral chemistry. Electron microprobe analysis (EMPA) of 11 polished thin sections was conducted to investigate mineral chemical variations in chlorites, carbonates, and white micas. EMPA was conducted at the Memorial University Electron Microprobe Analyzer Laboratory using a JEOL JXA-8230 Electron Probe Microanalyzer.

Software for geological modeling and vizualization: Geologic, geochemical, and hyperspectral data were integrated with Reflex ioGas, ESRI ArcGIS, and Geosoft Target for ArcGIS software for analysis and modeling. Tectonostratigraphic units were attributed in ioGAS based on drill logs and immobile element chemistry. Tectonostratigraphy and alteration patterns were modeled in Target for ArcGIS using strip logs and cross sections.

1.7 Co-Authorship Statement

The design of this research project is attributed to Dr. Stephen J. Piercey. The author conducted the primary research, which included the core logging, sample collection, optical microscopy, hyperspectral analysis, and software modeling aspects of the project. Scanning electron microscopy was conducted by the author under the supervision of Dr. David Grant, and electron microprobe analysis was conducted by the author and Dr. Wanda Aylward. The primary editor of this thesis was Dr. Stephen J. Piercey, with secondary editing performed by Dr. Graham Layne and thesis examiners (to be determined).

1.8 Thesis Presentation

This thesis consists of three chapters plus supplementary appendices. Chapter 1 serves as an introductory chapter that presents the purpose and format of this thesis by providing background information about the regional and local geology, previous work on the deposit, and the methods used in this study.

Chapter 2 is the main body of the thesis and is intended for publication in Economic Geology or a similar scientific journal. This chapter contains detailed descriptions of the lithology and alteration assemblages, and presents evidence pertaining to the tectonostratigraphic setting, a complete deposit alteration model, and its genesis.

Chapter 3 is a summary of the conclusions drawn from Chapter 2 and additional evidence provided in the appendices. This chapter also discusses unresolved questions and directions for future research.

References

Anderson, S. D., Jamieson, R. A., Reynolds, P. H., & Dunning, G. R. (2001). Devonian Extension in Northwestern Newfoundland: ^{40}Ar/^{39}Ar and U-Pb Data from the Ming's Bight Area, Baie Verte Peninsula. *The Journal of Geology*, *109*(2), 191-211.

Bédard, J. H. (2000). *Betts Cove ophiolite and its cover rocks, Newfoundland* (No. 550). Natural Resources Canada.

Bierlein, F.P., Arne, D.C., McKnight, S., Lu, J., Reeves, S., Besanko, J., Marek, J. and Cooke, D. (2000). Wall-rock petrology and geochemistry in alteration halos associated with mesothermal gold mineralization, central Victoria, Australia. *Economic Geology*, *95*(2), 283-311.

Bradbury, K. (2008). Newfoundland and Labrador: Moving ahead in tough times. *CIM Magazine-Canadian Institute of Mining Metallurgy and Petroleum*, *3*(8), 46.

Brueckner, S. M., Piercey, S. J., Sylvester, P. J., Maloney, S., & Pilgrim, L. (2014). Evidence for syngenetic precious metal enrichment in an Appalachian volcanogenic massive sulfide system: The 1806 Zone, Ming Mine, Newfoundland, Canada. *Economic Geology*, *109*(6), 1611-1642.

Castonguay, S., Skulski, T., van Staal, C., & Currie, M. (2009). New insights on the structural geology of the Pacquet Harbour group and Point Rousse complex, Baie Verte peninsula, Newfoundland; *in Current Research, Newfoundland and Labrador Department of Natural Resources, Geological Survey, Report 09-1*, 147-158.

Castonguay, S., van Staal, C. R., Joyce, N., Skulski, T., & Hibbard, J. P. (2014). Taconic Metamorphism Preserved in the Baie Verte Peninsula, Newfoundland Appalachians: Geochronological Evidence for Ophiolite Obduction and Subduction and Exhumation of the Leading Edge of the Laurentian (Humber) Margin During Closure of the Taconic Seaway. *Geoscience Canada*, *41*(4), 459-482.

Christie, A. B., & Brathwaite, R. L. (2003). Hydrothermal alteration in metasedimentary rock-hosted orogenic gold deposits, Reefton goldfield, South Island, New Zealand. *Mineralium deposita*, *38*(1), 87-107.

Dimmell, P., & Hartley, C. (1991). Gold Mineralization and Exploration Potential of the Pine Cove Property, Baie Verte Peninsula. *Ore Horizons, 1*, 51-62.

Dubé, B., Lauzière, K., & Poulsen, H. K. (1993). The Deer Cove deposit: an example of" thrust"-related breccia-vein type gold mineralization in the Baie Verte Peninsula, Newfoundland; *in Current Research, Part D; Geological Survey of Canada, Paper 93-1D,* 1-10.

Dube, B., & Gosselin, P. (2007). Greenstone-hosted quartz-carbonate vein deposits. *Mineral Deposits of Canada: A synthesis of major deposit-types, district metallogeny, the evolution of geological provinces, and exploration methods: Geological Association of Canada, Mineral Deposits Division, Special Publication*, *5*, 49-73.

Duncan, D.R. and Graves, R.M. (1992). 1992 Assessment Report (7th year work), Geology and diamond drilling on the Pine Cove property Baie Verte Peninsula, Newfoundland. *Novagold Resources. Newfoundland Department of Mines and Energy, Geological Survey, 012H/16/1278*, 43 pages.

Eilu, P., & Groves, D. I. (2001). Primary alteration and geochemical dispersion haloes of Archaean orogenic gold deposits in the Yilgarn Craton: the pre-weathering scenario. *Geochemistry: Exploration, Environment, Analysis*, *1*(3), 183-200.

Eilu, P., Mikucki, E. J., & Dugdale, A. L. (2001). Alteration zoning and primary geochemical dispersion at the Bronzewing lode-gold deposit, Western Australia. *Mineralium Deposita*, *36*(1), 13-31.

Evans, D.T.W. (2004). Epigenetic gold occurrences, Baie Verte Peninsula, (NTS 12H/09, 16 and 12I/01), Newfoundland. *Government of Newfoundland and Labrador, Department of Natural Resources, Geological Survey. Mineral Resource Report #11*, 157 pages.

Goldfarb, R.J. and Groves, D.I. (2015). Orogenic gold: Common or evolving fluid and metal sources through time. *Lithos*, *233*, pp.2-26.

Groves, D. I., Goldfarb, R. J., Gebre-Mariam, M., Hagemann, S. G., & Robert, F. (1998). Orogenic gold deposits: a proposed classification in the context of their crustal distribution and relationship to other gold deposit types. *Ore Geology Reviews*, *13*(1), 7-27.

Halley, S., Dilles, J. H., & Tosdal, R. M. (1999). Footprints: Hydrothermal Alteration and Geochemical Dispersion Around Porphyry Copper Deposits. *SEG Newsletter*, *100*(p. 1), 12-17.

Hibbard, J. (1983). Geology of the Baie Verte Peninsula, Newfoundland. *Mineral Development Division, Department of Mines and Energy, Government of Newfoundland and Labrador.* Memoir 2, 279 pages.

Jia, Y., Kerrich, R., & Goldfarb, R. (2003). Metamorphic origin of ore-forming fluids for orogenic gold-bearing quartz vein systems in the North American Cordillera: Constraints from a reconnaissance study of δ15N, δD, and δ18O. Economic Geology, *98*(1), 109-123.

Kerr, A., & Selby, D. (2012). The timing of epigenetic gold mineralization on the Baie Verte Peninsula, Newfoundland, Canada: new evidence from Re–Os pyrite geochronology. *Mineralium Deposita*, *47*(3), 325-337.

Meade, J., Evans, D. T. W., & Wilton, D. H. C. (1998). Romeo and Juliet Prospect, Baie Verte Peninsula, Newfoundland. *in Current Research, Newfoundland Department of Mines and Energy, Geological Survey, Report 98-1*, 77-83.

Mernagh, T. P., & Bierlein, F. P. (2008). Transport and precipitation of gold in Phanerozoic metamorphic terranes from chemical modeling of fluid-rock interaction. Economic Geology, 103(8), 1613-1640.

Mikucki, E. J. (1998). Hydrothermal transport and depositional processes in Archean lode-gold systems: a review. *Ore Geology Reviews*, *13*(1), 307-321.

Patey, K. S., & Wilton, D. H. (1993). The Deer Cove deposit, Baie Verte Peninsula, Newfoundland, a Paleozoic mesothermal lode-gold occurrence in the northern Appalachians. *Canadian Journal of Earth Sciences*, *30*(7), 1532-1546.

Phillips, G. N., & Powell, R. (2010). Formation of gold deposits: a metamorphic devolatilization model. Journal of Metamorphic Geology, 28(6), 689-718.

Pitcairn, I. K., Teagle, D. A., Craw, D., Olivo, G. R., Kerrich, R., & Brewer, T. S. (2006). Sources of metals and fluids in orogenic gold deposits: insights from the Otago and Alpine Schists, New Zealand. Economic Geology, 101(8), 1525-1546.

Pitcairn, I. K., Craw, D., & Teagle, D. A. (2015). Metabasalts as sources of metals in orogenic gold deposits. Mineralium Deposita, 50(3), 373-390.

Poulsen, K. H., Robert, F., & Dubé, B. (2000). Geological classification of Canadian gold deposits. *Geological Survey of Canada*, *540*, 1-106.

Ramezani, J., Dunning, G. R., & Wilson, M. R. (2000). Geologic setting, geochemistry of alteration, and U-Pb age of hydrothermal zircon from the Silurian Stog’er Tight gold prospect, Newfoundland Appalachians, Canada. *Exploration and Mining Geology*, *9*(3-4), 171-188.

Ritcey, D. H., Wilson, M. R., & Dunning, G. R. (1995). Gold mineralization in the Paleozoic Appalachian Orogen; constraints from geologic, U/Pb, and stable isotope studies of the Hammer Down Prospect, Newfoundland. *Economic Geology*, *90*(7), 1955-1965.

Skulski, T., Castonguay, S., van Staal, C. R., Rogers, N., McNicoll, V., Kerr, A., & Escayola, M. (2009). Baie Verte Peninsula: an evolving geological story. *Geological Association of Canada, Newfoundland and Labrador Section Annual Fall Field Trip Guide. Geological Association of Canada,* 60 pages.

Skulski, T., Castonguay, S., McNicoll, V., van Staal, C., Kidd, W., Rogers, N., Morris, W., Ugalde, H., Slavinski, H., Spicer, W. and Moussallam, Y. (2010). Tectonostratigraphy of the Baie Verte oceanic tract and its ophiolite cover sequence on the Baie Verte Peninsula. *Newfoundland and Labrador Department of Natural Resources, Geological Survey, Report*, *1*, 315-337.

Thompson, A. J., Hauff, P. L., & Robitaille, A. J. (1999). Alteration mapping in exploration: application of short-wave infrared (SWIR) spectroscopy. *SEG Newsletter*, *39*(p. 1), 16-27.

van Staal, C. R. (2007). Pre-Carboniferous tectonic evolution and metallogeny of the Canadian Appalachians. *Mineral Deposits of Canada: a synthesis of major deposit-types, district metallogeny, the evolution of geological provinces, and exploration methods. Edited by WD Goodfellow. Geological Association of Canada, Mineral Deposits Division, Special Publication*, (5), 793-818.

van Staal, C. R., & Barr, S. M. (2012). Lithospheric architecture and tectonic evolution of the Canadian Appalachians and associated Atlantic margin. *Tectonic Styles in Canada: The LITHOPROBE Perspective. Edited by JA Percival, FA Cook, and RM Clowes. Geological Association of Canada, Special Paper*, *49*, 55.

van Staal, C.R., Chew, D.M., Zagorevski, A., McNicoll, V., Hibbard, J., Skulski, T., Castonguay, S., Escayola, M.P. and Sylvester, P.J. (2013) Evidence of Late Ediacaran Hyperextension of the Laurentian Iapetan Margin in the Birchy Complex, Baie Verte Peninsula, Northwest Newfoundland: Implications for the Opening of Iapetus, Formation of PeriLaurentian Microcontinents and Taconic–Grampian Orogenesis. *Geological Association of Canada, Geoscience Canada*; (40) 94-117.

Williams, H. (1979). Appalachian orogen in Canada. *Canadian Journal of Earth Sciences*, *16*(3), 792-807.

Williams, H., & St-Julien, P. (1982). The Baie Verte-Brompton line: early Paleozoic continent-ocean interface in the Canadian Appalachians. *Major structural zones and faults of the northern Appalachians: Geological Association of Canada Special Paper*, *24*, 177-208.

Williams H., Colman-Sadd, S.P., Swinden, H.S. (1988). Tectonostratigraphic divisions of central Newfoundland; *in Current Research, Part B; Geological Survey of Canada, Paper 88-1B,* 91-98.

Williams, H., Dehler, S. A., Grant, A. C., & Oakey, G. N. (1999). Tectonics of Atlantic Canada. *Geoscience Canada*, *26*(2).

Williams-Jones, A. E., Bowell, R. J., & Migdisov, A. A. (2009). Gold in solution. *Elements*, *5*(5), 281-287.

Xue, Y., Campbell, I., Ireland, T. R., Holden, P., & Armstrong, R. (2013). No mass-independent sulfur isotope fractionation in auriferous fluids supports a magmatic origin for Archean gold deposits. Geology, *41*(7), 791-794.

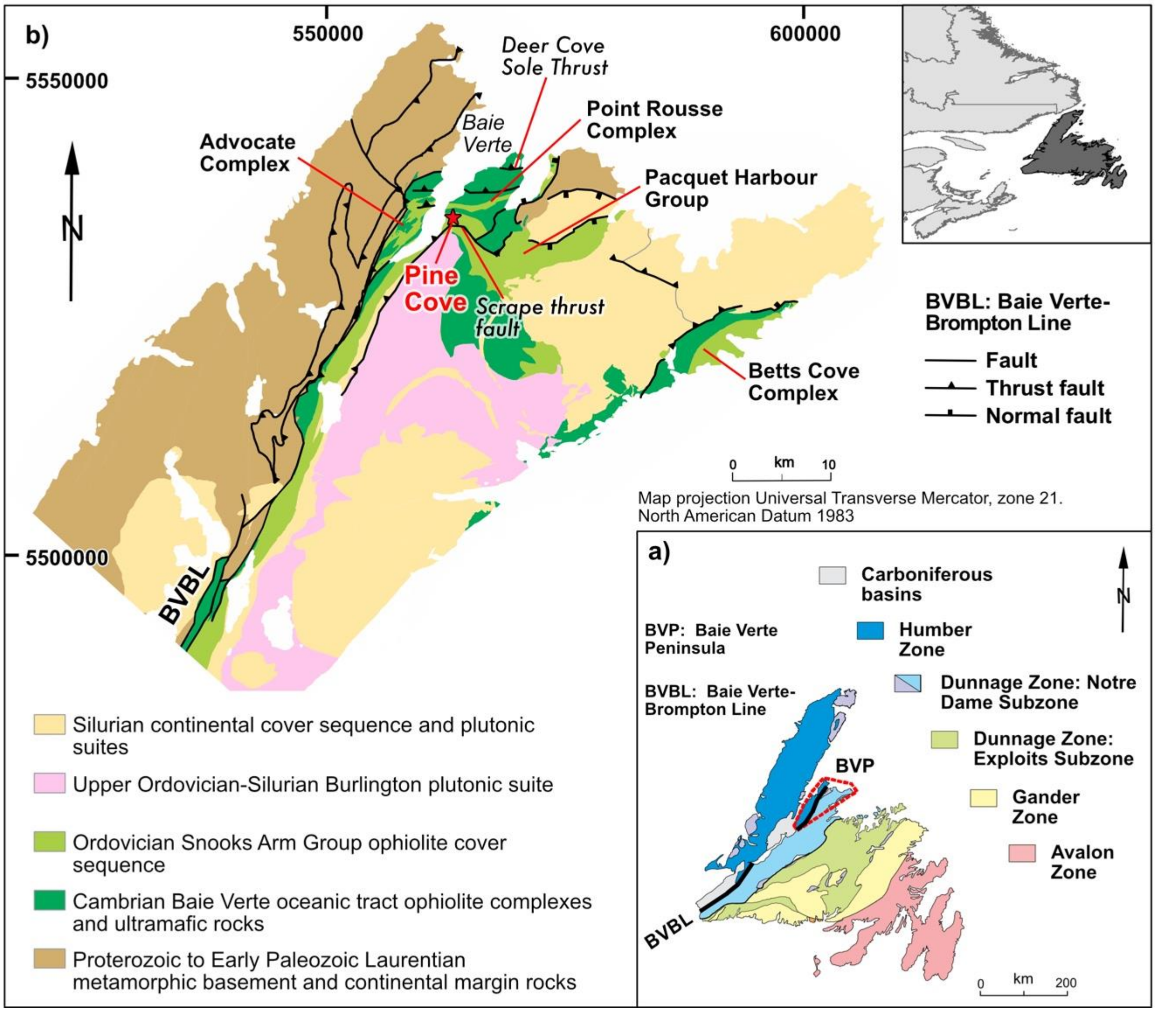

Figure 1.1. a) Simplified geologic map of Newfoundland. Modified from Skulski et al. (2017). b) Geologic map of the Baie Verte Peninsula. Modified from Skulski et al. (2017).

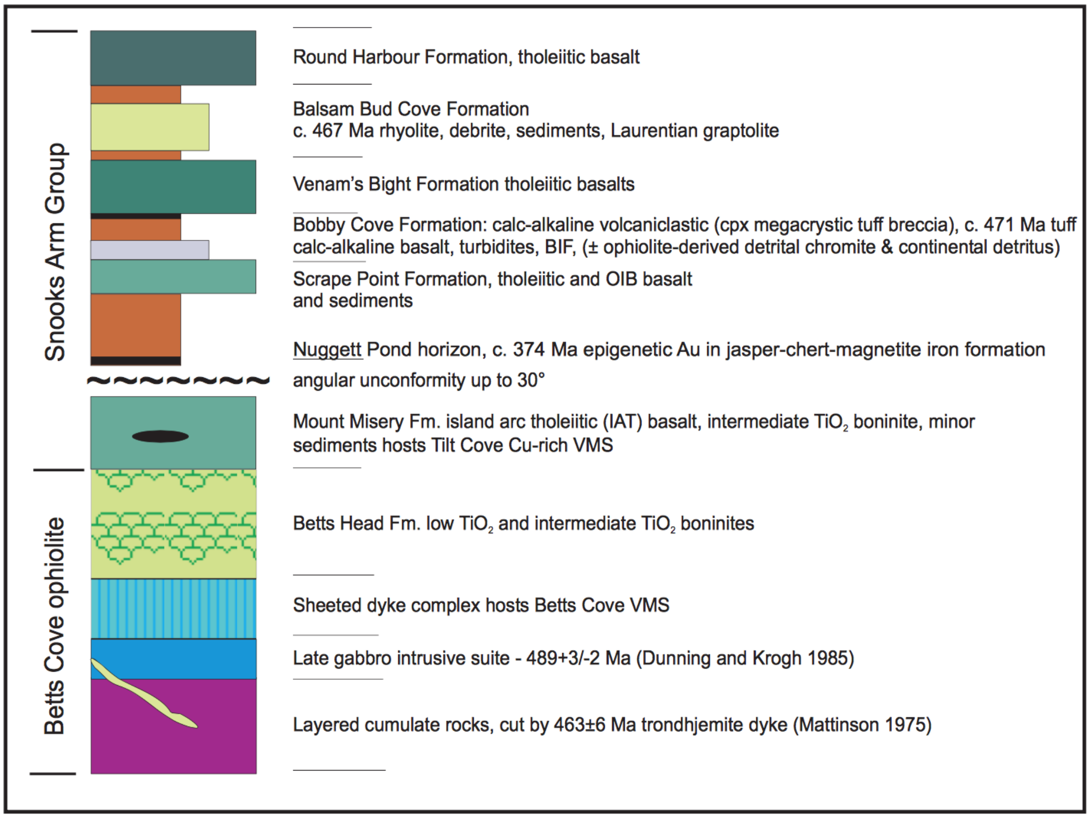

Figure 1.2. Stratigraphy of Betts Cove Complex and Snooks Arm Group. From Skulski et al. (2010).

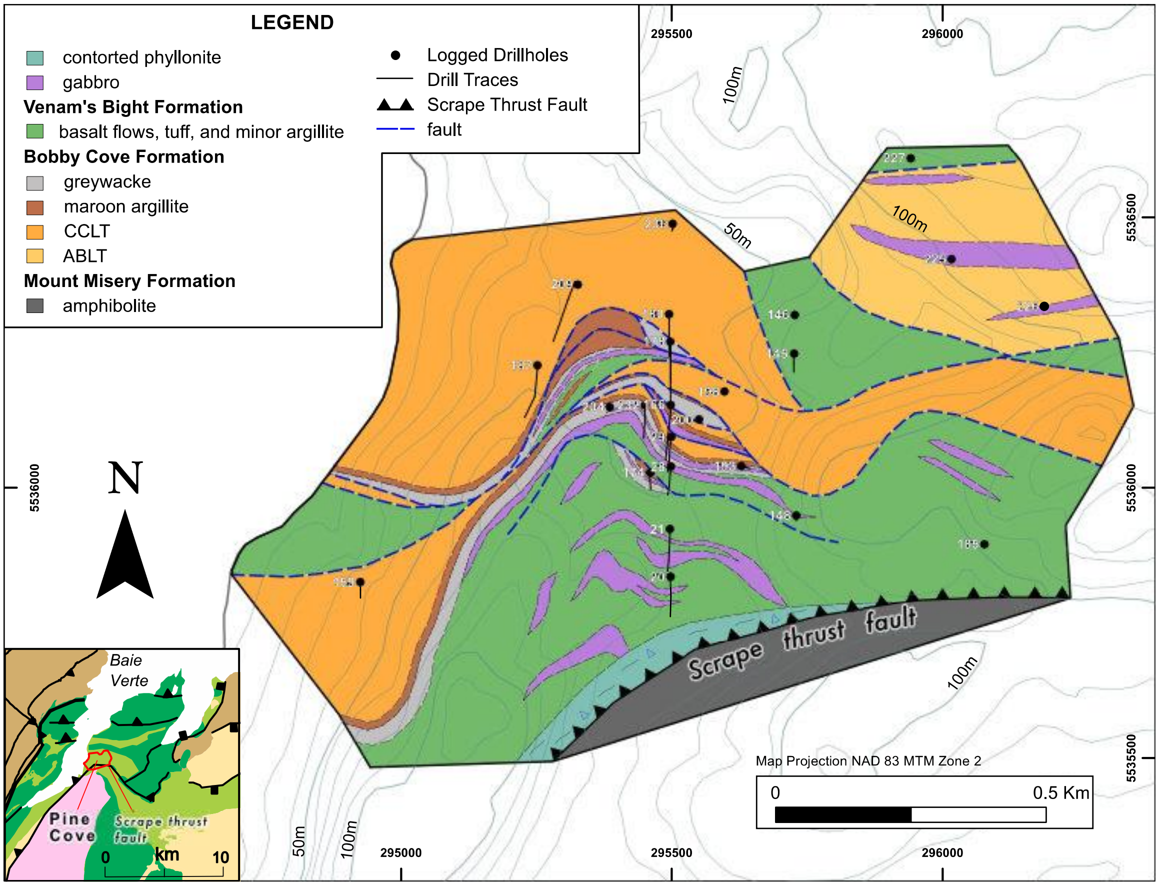

Figure 1.3. Pine Cove deposit geology plan map with mineralization lenses projected vertically to pre-mine surface. Drill holes shown on map were selected for logging and lithogeochemical analysis. Modified from unpublished mapping by Anaconda Mining. Extent of geology map shown with red outline in inset figure at bottom left. Legend for inset on Figure 1.

Chapter 2: Lithogeochemistry and Hydrothermal Alteration of the Pine Cove Orogenic Gold Deposit, Baie Verte Peninsula, Newfoundland, Canada

2.1 Abstract

The Pine Cove gold mine is hosted within Ordovician gabbro sills and volcano-sedimentary rocks of the Venam's Bight and Bobby Cove formations, Snooks Arm Group, Baie Verte Peninsula, Newfoundland Appalachians, Canada. The deposit is located approximately 50 to 200 m above the Scrape thrust fault, a brittle-ductile structure associated with Silurian transpression. Gold mineralization occurs as microscopic native Au inclusions in pyrite disseminated in the selvages of quartz-calcite-chlorite±albite breccia-veins. Multiple generations of overlapping veins are enveloped by sericite-rutile-calcite-pyrite alteration selvages.

Mineralized quartz breccia veins are most abundant at the contacts of gabbro sills and volcanosedimentary strata. Ore-grade mineralization predominantly occurs within Fe-rich gabbros and basalts of the Venam's Bight Formation. These relationships suggest that there were two fundamental controls on mineralization: 1) hydrofracturing assisted by anisotropic deformation of rigid gabbro sills within more ductile country rocks; and 2) sulfidation of the Fe-rich gabbros and basalts. Comparatively, the volcaniclastic rocks of the Bobby Cove Formation lack abundant gabbro intrusions and are relatively Fe-poor, and were thus a less receptive host rock to gold mineralization at Pine Cove.

Three distinct alteration assemblages are identified at Pine Cove: proximal sericite-rutile-chlorite-calcite, intermediate carbonate-chlorite, and distal epidote-titanite-chlorite-calcite. Mass balance calculations for altered wall rock show enrichments in CO_2, K_2O, S, Rb, W, In, Pb, Bi, Te, Se, Cs, and Ba, and depletions in As, Sb, and Na_2O. REE, HFSE, Al_2O_3, and most transition metals were generally immobile during alteration. There are distal to proximal elemental variations in relation to gold mineralization, and the generalized sequence of geochemical variation includes (from distal to proximal - 50m to 1m): CO_2 enrichment + As-Sb depletion → K-Rb enrichment → Na depletion → W±Pb±Ba enrichment → Au. The alkali-carbonate index $K_2O + CO_2$ / $K_2O + CO_2 + Na_2O + Al_2O_3$ coupled with As-Sb depletion is considered the most consistent metric of ore-related alteration at Pine Cove.

Combined short wave infrared (SWIR) spectrometry and electron microprobe analysis (EMPA) of white micas show that Tschermak substitution ($Al^{VI} + Al^{IV} \leftrightarrow [Fe^{2+},Mg]^{VI} + Si^{IV}$) and K/Na content correlate with AlOH absorption wavelengths. White mica compositions progress from phengite → paragonitic muscovite → muscovite approaching mineralization. A new potential SWIR index for orogenic gold exploration in greenschist facies rocks is the Fe^{2+} slope/MgOH-depth. At Pine Cove, this index measures the relative proportion of (Fe-carbonate + sericite)/chlorite, and correlates with the alkali-carbonate alteration index $K_2O + CO_2/K_2O + CO_2 + Na_2O + Al_2O_3$ and Au mineralization. Although the physico-chemical conditions during mineralization in orogenic gold deposits may vary from deposit to deposit, the collective visual, geochemical, and SWIR indices identified at Pine Cove represent potential vectoring tools for the discovery of similar deposits in orogenic Au camps globally.

2.2 Introduction

The Baie Verte Peninsula (BVP), Newfoundland, Canada, is host to numerous orogenic gold occurrences (Evans, 2004). Significant deposits include the past-producing Pine Cove (Dimmell and Hartley, 1991), Deer Cove (Patey and Wilton, 1993), Romeo & Juliet (Meade et al., 1997), and producing Stog'er Tight (Ramezani, 2002) deposits. Studies of orogenic gold deposits in other terrains have defined geochemical, mineralogical, and stratigraphic criteria useful for exploration target evaluation (e.g., Bierlein, 2000; Eilu and Groves, 2001; Eilu et al., 2001; Christie & Braithwaite, 2003; Dinel et al., 2008; Wang et al., 2017), but these techniques have not yet been tested on the Baie Verte Peninsula, and have only been tested in a cursory fashion in the Appalachian-Caledonide orogen as a whole. It is therefore difficult to assess factors that influenced the formation of these deposits quantitatively or to apply alteration models during exploration in this district, or elsewhere in the orogen. In light of recent tectonostratigraphic studies on the Baie Verte Peninsula (Skulski et al., 2010) and global models for orogenic gold deposits (Groves et al., 1998; McCuaig and Kerrich, 1998; Goldfarb et al., 2001; Dubé and Gosselin, 2007; Mernagh and Bierlein, 2008), characterization of alteration patterns and the stratigraphic setting of mineralization could significantly improve exploration targeting in the region.

This study characterizes the wall-rock alteration and lithostratigraphy at the recently-operating Pine Cove deposit. Owned and operated by Anaconda Mining Inc., mineral resource estimates as of 2017 were 863,500 tonnes @ 2.07 g/t Au Indicated and 476,300 tonnes @ 1.39 g/t Au Inferred (Cullen et al., 2017). Previous production is 118, 028 ounces of gold from 2,511,000 tonnes of ore since 2011 (Anaconda Mining Inc., 2018). The structural setting and geology of the deposit have been described by previous workers (Calon and Weicke, 1990; Dimmell and Hartley, 1991; Duncan and Graves, 1992), but no detailed studies of the lithology, mineralogy, or chemistry of the deposit have been conducted. As an economically viable deposit, Pine Cove presents an excellent case study to evaluate the alteration patterns and lithostratigraphic setting of gold mineralization on the Baie Verte Peninsula and greenstone-associated gold in the Appalachian orogen.

In this paper, a multi-method approach has been undertaken involving fieldwork (core logging and mapping), lithogeochemistry, short-wave infrared (SWIR) spectroscopy, petrography, scanning electron microscopy (SEM), and electron microprobe analysis (EMPA). This paper presents the geologic setting of gold mineralization and the characteristics of the associated hydrothermal alteration at Pine Cove. Our results provide both descriptive data, and insights into the hydrothermal footprint and alteration processes and genesis of orogenic Au in the Baie Verte Peninsula. The results have potential implications for orogenic deposits on the Baie Verte Peninsula, but also similar districts globally.

2.3 Geologic Setting

The Newfoundland Appalachians are comprised of four tectonostratigraphic zones; these are the Avalon, Gander, Dunnage, and Humber zones from east to west, respectively (Williams, 1979; Fig. 2.1A). The amalgamation of these tectonostratigraphic zones is the result of diachronous Paleozoic accretionary orogenesis that occurred during the closing of the Iapetus and Rheic Oceans, which culminated in the collision of Laurentia and Gondwana to form the supercontinent Pangea (van Staal, 2007; van Staal and Barr, 2012).

The Baie Verte Peninsula straddles a suture belt between the Humber Zone and Notre Dame subzone of the Dunnage Zone (Fig. 2.1B), termed the Baie Verte-Brompton Line (BVBL). The Baie Verte-Brompton Line extends through much of the Canadian Appalachians as a belt of disrupted ultramafic bodies and mélanges along a steeply-dipping structural zone interpreted to represent the tectonic interface between the Laurentian continent and the ancient Iapetus ocean (Williams and St. Julien 1982). On the Baie Verte Peninsula, the BVBL is a north-northeast to east trending fault zone that juxtaposes Ordovician oceanic terranes of the Notre Dame subzone against continentally-derived rocks of the Humber Zone (Hibbard 1983).

Gold mineralization on the Baie Verte Peninsula is predominantly hosted in Cambro-Ordovician ophiolite suites of the Baie Verte oceanic tract and their respective submarine volcano-sedimentary cover rocks (Evans, 2004; van Staal, 2007; Skulski et al., 2010; Skulski et al., 2015). The best preserved of these oceanic terranes on the Baie Verte Peninsula is the Betts Cove ophiolite and overlying Snooks Arm Group (Fig. 2; Hibbard, 1983; Bédard et al., 2000; Skulski et al., 2010). Skulski et al. (2010) recognized that the stratigraphy of the Betts Cove Complex correlates within other disrupted ophiolite sequences across the Baie Verte Peninsula. As such, the stratigraphy defined by

Bédard et al. (2000) for the Betts Cove area provides a template to correlate the stratigraphic and structural position of the host rocks at Pine Cove. Below is a brief description of the Betts Cove ophiolite and Snooks Arm Group; detailed descriptions of units can be found in Bédard et al. (2000), Cousineau and Bédard (2000), and Kessler and Bédard (2000).

The Betts Cove ophiolite is comprised of a lower ultramafic cumulate section, overlain by gabbros, sheeted dykes, and pillowed boninites (Bédard et al. 2000; Skulski et al, 2010). The Betts Cove ophiolite is interpreted to be the product of seafloor spreading in a fore-arc basin (Bédard et al. 2000). The ophiolite sequence is unconformably overlain by the Snooks Arm Group, which is subdivided into the Scrape Point Formation, Bobby Cove Formation, Venam's Bight Formation, Balsam Bud Cove Formation, and Round Harbour Formation, in stratigraphic succession (Bédard et al., 2000; Skulski et al, 2010). The Scrape Point Formation is predominantly tholeiitic, high-Ti basalts interbedded with sedimentary rocks; locally the sedimentary member consists of iron formation and ferruginous sedimentary rocks (Bédard et al., 2000). The overlying calc-alkaline Bobby Cove Formation contains a lower volcaniclastic member, which includes a distinctive clinopyroxene-phyric tuff termed the East Pond member (Skulski et al., 2010), and an upper member composed of epiclastic volcanogenic turbidites interbedded with pelagic mudstone (Cousineau and Bédard, 2000). The Venam's Bight Formation consists of tholeiitic, high-Ti basalts with minor interbedded volcanic breccia and hematitic mudstone (Skulski et al., 2010). The Balsam Bud Cove Formation predominantly consists of felsic tuff, rhyolite, tholeiitic basalt, and debris flow deposits, with lower mafic epiclastic rocks and black graptolitic shale (Bédard et al., 2000; Kessler and Bédard, 2000; Skulski et al., 2010). The Round Harbor Formation is composed of tholeiitic high-Ti basalt interbedded with minor chert (Bédard et al., 2000). Collectively, the Snooks Arm Group represents repeated cycles of arc-related tholeiitic volcanism and volcanogenic sedimentation, punctuated by calc-alkaline volcanism and periods of erosion during volcanic quiescence (Bédard et al., 2000; Cousineau and Bédard, 2000; Kessler and Bédard, 2000).

The Baie Verte Peninsula has been subject to four deformation events (D_1, D_2 (and D_{2b}), D_3, and D_4; Castonguay et al. 2009). The first deformation event (D_1) is mainly preserved as a micaceous schistosity in Humber Zone rocks west of the BVBL, but is mostly overprinted by later deformation elsewhere. This phase is associated with the obduction of Ordovician oceanic terranes during the Ordovician Taconic orogeny (van Staal, 2007; Castonguay et al. 2009). D_2 is the main tectonometamorphic phase on the Baie Verte Peninsula, and is responsible for burial of the ophiolites and crustal thickening during Silurian sinistral transpression associated with the Salinic orogeny (Dunning et al., 1990; Castonguay et al., 2009; Skulski et al., 2010). D_2 fabrics are associated with north-dipping, south-directed faults and shear zones, such as the Scrape thrust fault. D_3 deformation is expressed as recumbent folds and south-dipping extensional shear zones attributed to Devonian dextral transtension to transpression (Anderson et al., 2001). D_4 deformation is characterized by NNE-trending, upright crossfolds that are variably developed across the peninsula (Castonguay et al. 2009).

Epigenetic gold mineralization in the Baie Verte Peninsula region is spatially associated with brittle-ductile D_2 faults, such as the Scrape thrust and Deer Cove sole thrust faults (Dimmell and Hartley, 1991; Dube et al., 1993; Evans, 2004). Radiometric age determinations from various deposits, and the spatial association between gold and Silurian D_2 faults, suggests that gold mineralization was coeval with Silurian-Devonian orogenesis (Ritcey et al., 1995; Ramezani, 2002; Castonguay et. al, 2009; Kerr & Selby, 2011; Castonguay et. al, 2014).

2.4 Deposit Geology

The Pine Cove deposit occurs immediately north, and within the hanging wall, of the Scrape thrust fault (Fig. 2.3). An interpretative cross section through the center of the deposit illustrating the sub-surface spatial extent of units is shown Figure 2.4. In the Pine Cove deposit, the Scrape thrust fault is a brittle-ductile deformation zone characterized by 25 to >90 m of greenschist phyllonite juxtaposed over amphibolite (Fig. 2.5A). The amphibolitic rocks below the Scrape thrust fault are correlated with rocks of the Pacquet Harbour Group of Hibbard (1983), Dimmell and Hartley (1991), and Skulski et al. (2010). The hangingwall phyllonite is a variably-deformed quartz-chlorite-sericite-carbonate-rutile schist with abundant, gently-inclined to recumbent, open to tight mesoscopic folds (Fig. 2.5B). Fold styles vary from smooth parallel to asymmetric kink folds. Small-scale axial planar shear zones and an axial planar crenulation cleavage are locally developed where folding is most intense. The phyllonite contains abundant folded and/or boudinaged barren quartz veins, and ductile deformation features are locally overprinted by brecciation and gouge zones. The phyllonite transitions upwards into pervasively carbonate-chlorite altered mafic volcanic rocks (Fig. 2.5C) with locally interbedded argillite. Primary textures and mineralogy are mostly destroyed by alteration and deformation, but these rocks are interpreted to be basalt flows and tuffs of the Venam's Bight Formation (VBF) based on immobile element lithogeochemistry (see section 2.6 Lithogeochemistry).

Overlying the Venam's Bight Formation is ≤ 45 m of thinly-bedded, turbiditic, polymictic greywacke (Fig. 2.5D). The greywacke locally exhibits inverse grading and contains distinctive mm-scale, sub-round clasts of symplectic granite, grains of quartz, and aggregates of leucoxene in an albite-quartz matrix. The greywacke is overlain by ≤ 50 m of laminated to thinly-bedded, maroon argillite (Fig. 2.5E). This argillite consists of hematitic-siliceous layers interbedded with green tuffaceous layers.

Above these sedimentary rocks are predominantly volcaniclastic rocks comprised of clinopyroxene-phyric basaltic tuff and lapilli tuff, with interbedded epiclastic wacke and green mudstone (Fig. 2.5F). Tuffs are commonly massive, and lapilli fragments are characteristically clinopyroxene-phenocrystic, sub-rounded to sub-angular, and similar in composition to enveloping basaltic tuffs. Chromite locally occurs as an accessory mineral. These volcaniclastic rocks are interpreted to correlate with clinopyroxene crystal tuff and lapilli tuff within the Bobby Cove Formation (herein labeled BCF-CCLT).

East-northeast of the deposit is locally underlain by lapilli tuff, heterolithic tuff, wacke, and minor mudstone (Fig. 2.5G). This unit locally contains pebble- to lapilli-sized clasts of amygdaloidal basalt, mudstone, and fine-grained mafic tuff. Lapilli-sized fragments typically comprise plagioclase±pyroxene-porphyritic basalt with zeolite-quartz±chlorite-filled amygdules. Where less deformed, lithic fragments are more angular than those in the clinopyroxene crystal-lapilli tuff. This unit does not occur in the main deposit sequence and the stratigraphic relation to other units is not known, but it is inferred to overlie and/or interfinger with the clinopyroxene-phyric lapilli tuff unit. The amygdaloidal basalt clast-bearing lapilli tuff and associated clastic rocks are also interpreted to be a unit within the Bobby Cove Formation (herein labeled BCF-ABLT).

High Fe-Ti gabbro sills (Fig. 2.5H) intrude all other units along bedding and between contacts. These gabbros characteristically contain approximately 10 to 15% titanomagnetite that is typically altered to skeletal leucoxene. Contacts between units within the deposit are commonly faulted, though para-conformable to intercalated where less deformed.

The Pine Cove area exhibits a complex structural history resulting from regional D_2 and D_3 (of Castonguay et al., 2009) deformation concentrated along the Scrape thrust fault, and regional D_4 folding. The interference of at least three regional to macroscopic fold systems are described in detail by Calon and Weick (1990) and summarized below. Early polyphase deformation (D_1, D_2, and D_3 of Calon and Weick, 1990; D_2 of Castonguay et. al, 2009) resulted in a penetrative, north-dipping regional cleavage and mineral elongation that is generally parallel to bedding. Pressure solution during early D_2 deformation produced barren, recrystallized quartz veinlets sub-parallel to the regional foliation. The composite D_2 deformation produced a south-directed fold and thrust system associated with development of the Scrape thrust fault (Calon and Weick, 1990).

D_2 folding is associated with brittle/plastic shearing sub-parallel to fold axial surfaces and the emplacement of quartz vein networks at various orientations. The dominant auriferous vein set consists of a moderately north-dipping, quartz±chlorite-carbonate breccia/ vein swarm. These gently-inclined breccia veins represent injections into shear zones parallel to the axial surfaces of D_2 folds (Calon and Weick, 1990). Later D_3 deformation produced shallowly-inclined to recumbent, open to tight folds. The low over high metamorphic grade relationship across the Scrape thrust fault is attributed to reactivation of the Scrape thrust as a D_3 extensional fault (Castonguay et al., 2009). D_4 deformation (D_4 of Calon and Weick, 1990; D_4 of Castonguay et. al, 2009) produced gently to steeply north-plunging regional folds. A D_4 antiform is expressed in the arcuate pattern of the Scrape thrust fault through the study area.

2.5 Alteration and Mineralization

2.5.1 Mineralization

The Pine Cove ore body occurs within lenses 50 to 200 m above and broadly parallel to the north-dipping Scrape thrust fault, and gold mineralization occurs almost exclusively within sericite-chlorite-carbonate±rutile altered host rocks (Fig. 2.6). Ore lenses are predominantly hosted within basalts of the Venam's Bight Formation, greywacke of the Bobby Cove Formation, and gabbros, although mineralization occurs within all observed units in the deposit.

Mineralization occurs as microscopic native Au inclusions in pyrite (Fig. 2.7A). Au-hosting pyrite has a “grungy” appearance due to abundant calcite±rutile and quartz microveinlets and inclusions of rutile-quartz±carbonate±monazite (Fig. 2.7B). Pyrite occurs mainly within alteration selvages of overlapping, multi-generational quartz-chlorite-calcite±albite breccia-veins (Fig. 2.7C-D; Type V of Witt, 1993), but also as clusters along foliation or rarely within the quartz veins. Pyrite is typically restricted to within 1 to 2 meters around the breccia veins, but in some cases is disseminated in the wall rock up to several meters from the veins, particularly in the more porous sedimentary units (Fig. 2.7E).

Gold and pyrite content commonly increases with the abundance of quartz breccia-veins; however, some quartz breccia-veins lack any associated increase in Au or pyrite mineralization. Other sulphides that occur in trace amounts include chalcopyrite, galena, and cobaltite. Chalcopyrite and galena occur as both inclusions in pyrite and filling fractures in pyrite.

Quartz breccia veins are predominantly gently-inclined and are most abundant along and near the contact between gabbro sills and country rock. Veins crosscut or parallel the D_2 foliation/lineation, and locally intrude subparallel to axial planes of gently-inclined folds (Fig. 2.7F).

2.5.2 Alteration

Alteration assemblages at Pine Cove include: 1) distal epidote-chlorite±carbonate; 2) intermediate carbonate-chlorite; and 3) proximal sericite-rutile-chlorite-carbonate. In detail, alteration patterns are irregular, overlapping, and likely both controlled and displaced by numerous subsidiary faults along the Scrape thrust fault. Alteration facies reflect relative distance to mineralization, but this distance is highly variable. The progressive changes in alteration mineralogy away from ore, described below, are relatively consistent. However, it is important to note that alteration zonation at Pine Cove is complicated by the lithologic control of alteration mineralogy (e.g., titanite/rutile are restricted to rocks that originally had titanomagnetite or ilmenite) that are commonly sub-parallel to ore zones. Additionally, pervasive sericite-rutile-chlorite alteration is concentrated in the hanging wall phyllonite of the Scrape thrust fault, whereas alteration in the footwall amphibolite varies from unaltered to weak chlorite-carbonate±sericite and lacks epidote alteration, which produces an asymmetry in the alteration halo.

Distal alteration is visually distinguished by the occurrence of green epidote and chlorite (Fig. 2.8A) and pale grey titanite (Fig. 2.8B). Distal assemblages include epidote-chlorite-carbonate±albite that replace feldspars and pyroxenes (Fig. 2.8C), and titanite that has partially to completely replaced titanomagnetite (Fig 2.8D). The dominant veins in this alteration zone contain quartz and/or calcite and locally chlorite±albite. Pyrite±chalcopyrite are also locally disseminated along foliations in host rocks. Further, this alteration assemblage locally contains up to 5% disseminated pyrite; however, Au content is generally low (Au up to 0.014 ppm, but generally <0.005 ppm). Pyrite in this assemblage is anhedral to euhedral and generally inclusion free, but is locally fractured, with chalcopyrite infilling fractures. Within this zone, calcite alteration increases with proximity to Au mineralization. Hematite coating of fracture surfaces is also common throughout this zone, and, locally, magnetite porphyroblasts rimmed by hematite occur proximal to Au mineralization. In some cases, the intensity of epidote-chlorite alteration increases with proximity to sericite-rutile-chlorite alteration and Au mineralization. The epidote-chlorite-titanite assemblage occurs between ~1 m to >50 m away from Au mineralization, and while the assemblage is widespread the extent of this zone is not well-constrained. Nevertheless, gabbro with primary feldspar-titanomagnetite and minimal epidote alteration occurs approximately 500 m east-northeast from the main ore zones, suggesting that the extent of alteration is less than 500 m from mineralization.

Intermediate assemblages contain increased carbonate-chlorite alteration coupled with the absence of epidote. Carbonate alteration occurs as pervasive alteration of silicates and/or as mm-scale ankerite porphyroblasts (Fig. 2.9A). Locally, alternating mm-scale layers of carbonate-quartz-albite and chlorite-carbonate±rutile±titanite±titanomagnetite parallel the D_2 foliation causing the rocks to have the appearance of banding (Fig. 2.9B). Subhedral to euhedral pyrite and magnetite are locally disseminated in both carbonate- and chlorite-dominant layers (Fig. 2.9C). Magnetite is commonly partially replaced by hematite. The dominant Ti-bearing phase is typically titanite, but it is partially replaced by rutile with increasing carbonate alteration (Fig. 2.9D). The dominant veins in this zone are 1-5 mm quartz±carbonate veinlets parallel to D_2 foliation. Gold values are typically <0.04 ppm in this alteration zone, although rare Au mineralization up to 0.15 ppm occurs with disseminated pyrite. This alteration zone can be absent in some areas of the deposit, and is typically best developed in fine-grained tuffaceous and sedimentary rocks of the Venam's Bight Formation, where it can extend as much as 25m away from proximal alteration.

Proximal alteration is marked by the occurrence of tan muscovite (Fig. 2.10A) and pale orange-weathering rutile (Fig. 2.10B) and coincides with increasing schistosity in host rocks. Muscovite is most apparent in the greywacke and volcanic rocks of

Venam's Bight Formation, whereas rutile is the most visibly significant alteration mineral in gabbro. Muscovite alteration occurs along foliation and typically increases with proximity to breccia-veins. Rutile occurs predominantly as pseudomorphs of titanomagnetite (Fig. 2.10C) and disseminated along foliation. A distinct generation of rutile occurs as subhedral crystals in calcite veinlets that cut foliation (Fig. 2.10D) and locally infill fractures in pyrite. The dominant carbonate species in this zone is calcite, but ankerite and rare magnesian siderite also occur. Where present, ankerite porphyroblasts are commonly overprinted by pervasive carbonate alteration (Fig 2.10E). Porphyroblastic pyrite commonly has calcite and/or chlorite pressure shadows and abundant inclusions of rutile-calcite-quartz±monazite±chalcopyrite (Fig. 2.10F). Pervasive chlorite alteration increases from the intermediate to proximal zone, and typically exhibits anomalous purple-blue birefringence; locally chlorite also occurs as veinlets. This alteration assemblage occurs in close association with the quartz-chlorite-calcite±albite±pyrite breccia-vein swarms, and extends from 1 to 25 meters from Au mineralization. Accessory minerals, such as apatite and monazite, are also common in this assemblage. Hematite along fractures is typically absent in the proximal alteration zone, although Ti-magnetite is locally replaced by bladed hematite.

Proximal muscovite-rutile-carbonate-chlorite±pyrite alteration is also widespread in the phyllonite below the ore lenses, which contains abundant folded and/or boudinaged quartz veins but typically lacks Au mineralization. The altered phyllonite is truncated in its footwall by 1 to 2 m of deformed wall rock and clay gouge that separate the phyllonite from the underlying amphibolite. Amphibolite was only observed in two drill holes, but generally lacks the alteration observed in the hangingwall rocks. Titanite occurs in minor gabbro intrusions and weak calcite±chlorite alteration is present locally. Up to 5% pyrrhotite and pyrite are disseminated along foliation, and quartz±carbonate±pyrite-pyrrhotite veins locally have pyrite alteration selvages, but are devoid of Au mineralization. Minor tan sericite-carbonate-pyrite alteration, where observed, is associated with quartz-carbonate veins but also lacks Au mineralization.

2.6 Lithogeochemistry

2.6.1 Methods and Data Treatment

Twenty-three drill holes were logged for lithology, alteration, and mineralization, and from these holes 253 representative core samples were collected at approximately 10 to 20 m intervals for geochemical analyses. Drill core samples were supplemented by 29 surface samples from areas of limited or absent drilling. Rock and alteration types with minimal vein density were specifically targeted to reduce the influence of vein volume on magmatic discrimination and mass balance calculations. Samples were analyzed at ALS Inc. Laboratory in Vancouver, Canada, using their complete characterization package (CCP-PKG01). Samples were crushed and pulverized in mild steel to create powders that were used in subsequent analyses. Major element concentrations were determined via lithium borate fusion preparation of the sample powders, followed by four-acid digestion of the fused bead, and analysis by inductively coupled plasma atomic emission spectroscopy (ICP-AES). Trace element concentrations, including rare earth elements (REE) and high field strength elements (HFSE), were acquired via a lithium borate fusion preparation, four-acid digestion of the fused bead of the sample powders, and analysis by inductively coupled plasma mass spectroscopy (ICP-MS). Base metal concentrations were determined via four-acid digestion of the sample powder and ICP-AES, and volatile elements were determined via an aqua regia digestion of the sample powder and ICP-MS. Samples were analysed for Au by fire assay pre-preparation of samples powders and ICP-AES (Au-ICP21 package); and CO_2 concentration was determined via $HClO_4$ digestion of the powder and coulometry (C-GAS05). Results of lithogeochemical analyses are shown in Appendix A.

Quality control and quality assurance was monitored using certified reference materials, duplicates, and blanks. After every 20 samples an internal reference material was analyzed to monitor laboratory performance. Precision of reference materials is reported as percent relative standard deviation (%RSD_i; Jenner, 1996; Piercey, 2014):

$$\mathrm{RSD}_i\ (\%) = 100 \times \frac{s_i}{\mu_i}$$

where s_i is the standard deviation of the mean from the series of analytical runs for element i, and μ_i is the mean value of element i over the series of analytical runs. Precision of duplicate samples is reported as percent average coefficient of variation (%CV_{avg}; Abzalov, 2008, Piercey, 2014):

$$\mathrm{CV}_{avg}\ (\%) = 100 \times \sqrt{\frac{2}{N}\sum_{i=1}^{N}\{\frac{(a_i-b_i)^2}{(a_i-b_i)^2}\}}$$

where N is the number of duplicate pairs, and a_i and b_i are the original and duplicate analyses of the i^{th} pair, respectively. Accuracy of reference materials is reported as percent relative difference (RD_i; Piercey, 2014):

$$\mathrm{RD}_i\ (\%) = 100 \times \left(\frac{\mu_i - c_i}{c_i}\right)$$

where μ_i is the mean of element *i* over the series of analytical runs, and c_i is the "known" or "certified" value of element i in the reference material.

Overall, accuracy and precision are within ± 10% RD and RSD, respectively, and sufficient for the interpretations herein. Precision as measured by $\%CV_{avg}$ is also better than 10%. However, precision and accuracy are typically poorer for quantities that approach the limit of quantification for a given element, and are most pronounced for Hg, Se, and Te.

For data censoring (e.g., Sanford et al., 1993), sample determinations of below detection limit (BDL) values were replaced with values of ½ the detection limit (e.g., Carranza, 2011). All values for Ge were below the detection limit, so this element was removed from further analysis. The following elements have > 30% of values near and/or below the detection limit: Sn, Ta, Hg, Re, Tl, Li, Ag, Mo, Bi, Te, Se, Pb, and Cd. Although these components are reported in mass balance calculations below, it is important to note that the interpretation of resulting gains and losses is limited by the abundance of censored data.

2.6.2 Immobile Element Monitors

Many samples at Pine Cove exhibit some degree of metamorphism and/or hydrothermal alteration, as evidenced by widespread D_2 mineral lineations and elevated CO_2 and/or K_2O values (Table 2.1). Immobile monitor elements are therefore necessary to determine magmatic affinity and calculate mass changes for the protolith units (MacLean, 1990). In addition, fine-grained volcanic and volcaniclastic rock units at Pine Cove can be difficult to distinguish, particularly where alteration and deformation are present. However, as described below, volcanic/volcaniclastic rocks from each formation can be readily distinguished geochemically using immobile elements.

The determination of immobile elements involved comparison of binary variation diagrams after MacLean and Barrett (1993). For samples from a single homogeneous protoliths, binary scatter plots of the concentrations of immobile-incompatible elements produce linear arrays that project through the origin, whereas samples from multiple precursors form additional distinct trend lines and multiple linear arrays that project through the origin (MacClean and Kranidotois, 1987; MacLean and Barrett, 1993). At Pine Cove, most of the high field strength elements (HFSEs) and rare earth elements (REEs) form linear arrays, and therefore display immobile behavior and are considered acceptable for magmatic affinity monitors. High field strength elements (HFSE) have been shown to be mobile in CO_2-rich fluids (Hynes, 1980; Murphy and Hynes, 1986), although they do not appear to have been significantly mobilized during alteration at Pine Cove, despite the abundance of HFSE-bearing alteration phases (e.g., rutile and titanite). HFSE-bearing alteration phases are interpreted to have formed from the reaction of pre-existing HFSE-bearing phases and hydrothermal fluids, without any addition or removal of HFSE. Similarly, components of the Jensen cation plot (Al_2O_3, MgO, and Fe_2O_3) also appear to have remained relatively immobile at Pine Cove, as shown by the mass balance calculations below.

2.6.3 Magmatic Affinity and Sedimentary Provenance

Jensen cation plots and immobile element ratios were used to attribute magmatic affinity of volcanic rocks at Pine Cove (Fig. 9) (e.g. MacLean and Barrett, 1993; Ross and Bédard, 2009). Nearly all the rock types at Pine Cove fall within the basalt field of the Zr/Ti versus Nb/Y volcanic rock discrimination diagram of Pearce (1996), modified after Winchester and Floyd (1977), with a few exceptions plotting with the andesite/basalt field (Fig. 2.11A). However, lithologic distinction is readily apparent on the tectonic discrimination diagrams of Ross and Bédard (2009) and Pearce (2014).

On the Th/Yb versus Zr/Y discrimination diagram of Ross and Bédard (2009), Venam's Bight Formation basalts and gabbros display tholeiitic to transitional values, whereas Bobby Cove Formation clinopyroxene crystal tuffs and lapilli tuffs (BCF-CCLT) have transitional values (Fig. 2.11B). Bobby Cove Formation tuffs containing amygdaloidal basalt fragments (BCF-ABLT) distinctively have a calc-alkaline signature, and samples from the amphibolite below the Scrape thrust fault exclusively fall within the tholeiitic field.

On the Th/Yb versus Nb/Yb discrimination diagram of Pearce (2014), Venam's Bight Formation rocks and gabbros have enriched mid-ocean ridge basalt signatures, although some of the Venam's Bight Formation samples plot close to the normal mid-ocean ridge basalt field (Fig. 2.11C). BCF-CCLT samples plot within overlapping oceanic arc and continental arc fields, whereas BCF-ABLT samples predominantly have a continental arc basalt signature. The amphibolite rocks exclusively have an oceanic arc signature.

Gabbros, and Venam's Bight Formation volcanic rocks can also be distinguished by their enrichment in Fe and Ti relative to Bobby Cove Formation rocks (Fig. 2.11D). Additionally, on a Jensen cation plot (Jensen, 1976), Venam's Bight Formation rocks exhibit a tholeiitic trend, whereas Bobby Cove Formation rocks have a calc-alkaline trend (Fig. 2.11E).

The sedimentary rocks were also compared on geochemical discrimination diagrams to determine the provenance of these units. The lithogeochemical signature of the maroon argillite predominantly overlaps with the Bobby Cove Formation (Fig. 2.11F), suggesting that this unit is derived from erosion of the Bobby Cove Formation. The greywacke exhibits a geochemical signature that overlaps with both the Venam's Bight Formation and Bobby Cove Formation; this overlap, and the occurrence of granitic fragments in the greywacke, indicate that this unit has a provenance from multiple lithologies.

2.6.4 Normalized Multi-Element Plots

Multi-element patterns for igneous and volcaniclastic rocks normalized to N-MORB of Sun and McDonough (1989) are shown in Figure 2.12. These diagrams exclude the mobile elements Rb, Ba, Cs, U, K, Sr, P, and Pb (e.g., Pearce, 2014). The variation within units is attributed to mass/volume changes rather than mobility of the plotted elements during hydrothermal alteration, due to the uniform shift of the elements (Barrett et al., 2008) and the lack of evidence of REE and HFSE mobilization from mass balance calculations. The Venam’s Bight Formation and gabbro sills exhibit similar trends, with slightly enriched light REE (LREE). Bobby Cove Formation rocks exhibit higher Th/Nb and steeper LREE trends than the Venam’s Bight Formation. BCF-CCLT rocks are less enriched in incompatible elements than BCF-ABLT rocks, and amphibolitic rocks exhibit relatively high Th/Nb but have distinctively flat REE trends.

Geochemical patterns of the maroon argillite predominantly overlap with Bobby Cove Formation rocks, particularly the BCF-CCLT unit.

2.6.5 Comparison to Snooks Arm Group

The geochemistry of units at Pine Cove were compared to data from the type sequence of the Snooks Arm Group at Betts Cove (Bédard, 2000) to determine whether units could be correlated with a defined regional stratigraphy. A comparison of Ti/V and Ti/Zr data from Bédard (2000) shows that Pine Cove basalts predominantly overlap with the Venam's Bight Formation (Fig. 2.13A-B). Pine Cove basalts also predominantly overlap with samples of the Venam's Bight Formation on the $MnO*10-TiO_2-P_2O_5*10$ tectonic discrimination diagram of Mullen (1983) (Fig. 2.13C). Pine Cove BCF-CCLT rocks share magmatic affinities with low-Ti lavas of the Bobby Cove Formation, whereas the BCF-ABLT unit does not easily correlate with samples from Betts Cove.

A similar comparison of data from a regional study of the Snooks Arm Group in the Baie Verte Peninsula by Skulski et al. (2010; 2015) data revealed there is less geochemical distinction between the Scrape Point Formation and Venam's Bight Formation. However, Pine Cove BCF-CCLT rocks are geochemically similar to the basal clinopyroxene tuff and tuff breccia (Prairie Hat Member) of Skulski et al. (2010; 2015). Amphibolitic rocks below the Scrape thrust fault have tholeiitic, oceanic arc basalt immobile element chemistry, and overlap with samples of the Mount Misery Formation on the Th/Yb-Nb/Yb discrimination diagram of Pearce (2014) (Fig. 2.13D). Thus, the amphibolite is herein suggested to correlate with rocks of the Mount Misery Formation.

2.6.6 Mobile Element Chemistry

Mass Balance Calculations: Subdivisions of the Venam's Bight Formation and gabbros were made for the purposes of mass balance calculations due to significant fractionation of Al_2O_3 relative to TiO_2 and Zr (Fig. 2.14). These subdivisions were made using variation diagrams, including Al_2O_3/TiO_2, Al_2O_3/Zr, Ti/Sc, La/Sm, and Th/Yb, to group geochemically similar subunits that are derived from a single precursor. However, subdivision designations (A, B, etc.) in Figure 2.14 are not intended to convey any timing or stratigraphic relationship as they are simply chemical subdivisions.

A least altered sample for each subgroup was selected based on minimal visible alteration minerals (e.g., sericite, carbonate, pyrite), Au < 6 ppb, and low concentrations of CO_2, K_2O, Rb, LOI, and Pb. Mass balance calculations were then applied using the single-precursor method of MacLean and Barrett (1990) to each subgroup. Due to the fractionation of Zr and TiO_2 and the potential for the HFSEs to be mobile in CO_2-rich fluids (Hynes, 1980; Murphy and Hynes, 1986), Al_2O_3 was used to calculate enrichment factors from least altered samples. Subgroup E of the Venam's Bight Formation was not included in mass balance calculations due to lack of a suitable least-altered sample. Results of mass balance calculations are shown in Appendix B.

To illustrate the mass transfer trends, median relative enrichment factors for each component in both distal and proximal mineral assemblages are show in Figure 2.15A-B. These diagrams show mass transfer at Pine Cove primarily involved mass changes in CO_2, K_2O, Na_2O, S, Au, Rb, W, In, Pb, Bi, Te, Se, Cs, Ba, As, Sb, and possibly Cr and Cu. Components that show the greatest (~10x) relative mass changes are CO_2, K_2O, Rb, Cs, W, As and Sb. Mass transfer of select components is considered below by grouping the elements according to their geochemical behaviour.

SiO_2: In general, relative gains and losses of SiO_2 are minor. Although ΔSiO_2 varies from approximately -10 to +10% in individual samples (Appendix B), SiO_2 does not show systematic variation with lithology or alteration facies. Some Si enrichment is due to abundant <1 cm wide quartz veinlets that were not possible to remove prior to geochemical analysis. Although abundant quartz veins have been added to the rocks, the silica does not appear to be sourced from depletion of immediate country rocks.

CO_2 and S: CO_2 values define the most widespread hydrothermal alteration at Pine Cove, reflecting the carbonate replacement of silicate minerals and emplacement of quartz-carbonate veins. In all rock types, CO_2 values increases progressively from distal to intermediate to proximal alteration facies. Median ΔCO_2 for distal, intermediate, and proximal alteration zones are 1.3%, 4.5%, and 5.5%, respectively.

Sulfur shows erratic mobility and is enriched in some altered rocks, and depleted in others. Sulfur generally shows relatively minor gains and losses, which reflects the low total sulphide content of the deposit and alteration zones. Sulfur enrichment (up to 2.5%) predominantly occurs in altered gabbro in the proximal zone, reflecting pyrite formation during hydrothermal alteration.

Alkali and alkaline-earth elements: Nearly all mineralized samples have elevated K_2O, and the highest ΔK_2O values occur in the proximal sericite-rutile alteration facies. Median ΔK_2O for distal, intermediate, and proximal alteration zones are 0.07%, 0.03%, and 0.8%, respectively. In sericite alteration K_2O enrichment ranges from 0.1 – 2.5%, whereas in carbonate alteration K_2O exhibits either mass gains up to 1.3% or mass loss up to 0.4%. In distal alteration, K_2O exhibits either mass gains up to 1% or mass loss up to 0.4%. The primary K_2O content of the mafic rocks is assumed to be low, so mass losses are attributed to least altered samples that contain minor K-alteration and not actual K_2O depletion (i.e., least altered samples that are not unaltered).

Similar to K_2O, ΔRb and ΔCs are controlled by alteration facies and are most enriched in the proximal sericite-rutile alteration facies. Mass changes in Rb vary from -6 to +42 ppm, and correlate positively with ΔK_2O. Cs generally exhibits similar behaviour to Rb and K_2O, but at much lower concentrations (-1 to +4 ppm).

ΔNa_2O varies from -5 to +2.5%, independent of alteration facies or lithology. However, rocks with the highest K_2O generally have low Na_2O, although not all samples with low Na_2O exhibit K_2O gains.

In individual samples, CaO and Sr exhibit significant mass losses and gains: -11 to +13.5 wt.% and -328 to +522 ppm, respectively. However, these mass changes do not correlate with changes in alteration, lithology, or mineralization. As shown in Figure 2.15, the median mass changes in CaO and Sr during hydrothermal alteration are relatively low, indicating that this variation is attributed to the redistribution of these elements into hydrothermal minerals (e.g., carbonate) during the replacement of Ca- and Sr-bearing minerals in the unaltered rocks. Variation in Ca may also be partially attributed to early seafloor alteration during the evolution of the volcanic sequence (Humphris and Thompson, 1978).

Ba typically exhibits a positive correlation with proximal sericite alteration, with changes in concentration of up to 269 ppm.

Metalloids: As and Sb are generally depleted in all but distal epidote-altered rocks. ΔAs is strongly dependent on both rock type and alteration facies. In epidote alteration, ΔAs varies from +45 to -55 ppm, but is dominantly depleted, particularly in the Bobby Cove Formation. In carbonate and sericite alteration, gabbros show the least mass change in As (0 to -15 ppm), whereas Venam's Bight Formation has stronger As depletion (0 to -45 ppm), and Bobby Cove Formation is the most depleted (-40 to -55 ppm). Mass changes of Sb vary by alteration facies but are not dependent on lithology. ΔSb varies from +1.4 to -0.4 ppm in epidote alteration, and 0 to -0.5 ppm in carbonate and sericite alteration. Sb values are overall relatively low (< 1.7 ppm), so Sb depletion measurements are restricted by precision and the limit of detection (0.05 ppm). Decreasing As and Sb values coincide with increasing K_2O and CO_2 (Fig. 2.16C-D), demonstrating that As-Sb depletion can be attributed to hydrothermal alteration. Depletion of As-Sb extends as much as 50 to 100 m, beyond the extent of anomalous Au or sericite alteration (Fig. 2.17).

Tungsten commonly exhibits mass gains in the 10s of ppm range within proximal alteration, but does not typically extend significantly beyond the occurrence of Au > 0.01 ppm. Indium shows mass gains up to 0.1 ppm within proximal alteration, and locally within distal alteration. Bi, Te, and Se sporadically exhibit minor mass gains from approximately 0 to 1 ppm proximal to Au mineralization, but do not extend beyond anomalous Au. Bi, Te, and Se display the highest correlation with Au: $R^2 = 0.9$, 0.81, and 0.43, respectively.

Transition and base metals: Pb and Zn do not typically show significant gains or losses, but are locally enriched within Au mineralized intervals. Copper shows mass losses up to -110 ppm and mass gains up to 161 ppm, but changes do not correlate with alteration or mineralization. Similarly, Cr also exhibits mass losses up to 745 ppm and mass gains up to 534 ppm which do not correlate with alteration or mineralization. Other transition metals (Ti, Sc, V, Mn, Co, Ni) do not show significant gains or losses.

Other immobile elements: REE and most HSFE do not show significant mass changes and observed variability in these elements does not correlate with alteration or mineralization. Although both Fe and Mg exhibit mass changes up to ± 5%, the median gains and losses show that these elements remained relatively immobile during alteration.

Molar Element Ratios: Alteration indices as molar ratios of major elements are commonly used to quantify alteration in ore deposits, including orogenic gold systems (Kishida and Kerrich, 1987; Gao and Kwak, 1997; Eilu et al., 1998; Eilu and Groves, 2001; Christie and Braithwaite, 2003). The most applicable indices to orogenic gold-related alteration are the carbonate [CO_2/(Fe + Mg + Ca)], sericite [3K/Al], and albite [Na/Al] alteration indices (Kishida and Kerrich, 1987; Eilu and Groves, 2001).

The carbonate index measures the degree of carbonate alteration expressed as Fe-, Mg-, and Ca-bearing carbonates. The 3K/Al and Na/Al alteration indices reflect the formation of K-mica and albite, respectively. Since muscovite and carbonate are not always the dominant alteration minerals, Bierlein et al. (2000) calculated an alteration index composed of the major elements typically involved in geochemical exchange. They propose that the alkali-carbonate ratio [$K_2O + CO_2 / K_2O + CO_2 + Na_2O + Al_2O_3$] is a more reliable indicator of alteration than the sericite or carbonate indices, particularly in siliceous rocks.

The molar ratios CO_2/Ca, 3K/Al, and $K_2O + CO_2 / K_2O + CO_2 + Na_2O + Al_2O_3$ (alkali-carbonate index) define the most consistent and widest of the alteration indices at Pine Cove (Fig. 2.16A and 2.17). $CO_2/Ca = 1$ (e.g., Eilu et al., 1998) defines a broad calcite alteration halo, extending as much as 50 m away from samples with ≥0.01 ppm Au. 3K/Al > 0.2 also extends up to >50 m from mineralization; however, it is important to note that elevated K in argillaceous rocks may in part be influenced by detrital clay minerals. Na/Al typically exhibits depletion within K-enriched rocks, reflecting the alteration of albite to sericite (Fig. 2.16B). However, Na/Al can also be enriched within mineralized zones, reflecting the formation of pink, hydrothermal albite. The combined alkali-carbonate index (ACI) provides the best alteration index at Pine Cove, with ACI > 0.2 extending up to 50 m from mineralization (Fig. 2.17).

2.7 Short-wave Infrared Spectroscopy

Reflectance spectroscopy is used in mineral exploration to map mineral assemblages and compositional changes of alteration minerals (Thompson et al., 1999). This technique measures the absorption of light when it interacts with minerals. Certain atomic and molecular bonds absorb light at characteristic wavelengths, and the positions and relative intensities of these absorptions can be used to interpret mineralogy and chemical composition. The short-wave infrared (SWIR) range is particularly useful for the identification of mineral species and variations in mineral chemistry of OH-bearing silicates, carbonates, and sulfates (Fig. 2.18). The wavelength position of absorption features is used to infer the composition of the mineral assemblage, and the depth of an absorption feature can be used as a proxy for the relative abundance of a given mineral (AusSpec International, 2008). SWIR-active minerals discussed here include white micas and carbonate species.

White micas have characteristic absorption features centred around 2200 nm (Fig. 2.18), which relate to stretching and bending of AlOH bonds (Clark et al. 1990; Yang et al. 2011). Variations in composition will cause the minimum of this AlOH absorption feature to vary between approximately 2180 and 2228 nm (AusSpec International, 2008). Longer minima wavelengths have been shown to correlate with increasing (Fe,Mg)-Si content in white micas via the Tschermak substitution ($Al^{VI} + Al^{IV} \leftrightarrow [Fe^{2+},Mg]^{VI} + Si^{IV}$) (Duke, 1994; Herrmann et al. 2001; Buschette and Piercey 2016). This substitution is the most common cause for compositional variations between the three end-member white micas: muscovite, paragonite, and phengite (Yang et al. 2011). Muscovite generally has an AlOH absorption feature between 2200 and 2204 nm, whereas wavelengths shorter than 2195 nm are typical of paragonite, and wavelengths longer than 2210 nm are typical of phengite (Herrmann et al. 2001; AusSpec International 2008). Intermediate wavelengths are either intermediate composition or mixed white mica phases (Herrmann et al. 2001).

Carbonates have a diagnostic SWIR absorption feature (also called band) at 2340 nm, due to vibration of the CO_3^- anion (Gaffey, 1986a). However, it is difficult to characterize fine-grained carbonates in samples containing phyllosilicates using the 2340 nm band because: 1) the carbonate 2340 nm band overlaps with the MgOH and secondary AlOH absorption bands; and 2) carbonates also have weaker absorption coefficients compared to the phyllosilicates (Herrmann et al. 2001; AusSpec International 2008). In addition, while the 2340 nm band has been used to differentiate calcite, dolomite, and magnesite, it is less useful for discriminating Fe-bearing carbonates (Gaffey, 1986a; AusSpec International 2008). However, Fe-bearing carbonates have absorption bands at ~1200 nm, due to electronic transitions of Fe^{2+} (Gaffey, 1986b). These absorption features commonly modify the spectra of the SWIR-active hydrous minerals by creating a wide down-sloped region between approximately 1350 and 1650 nm (Fig. 2.18). Due to this, the slope of the reflectance spectra between 1350 and 1650 nm wavelengths can be used to quantify the occurrence of Fe-carbonate minerals (i.e., Fe^{2+} response; AusSpec International 2008).

2.7.1 Methods

A total of 827 spectra were obtained from drill core with an ASD, Inc. TerraSpec^{TM} 2 mineral spectrometer, which records spectra in the 350- to 2,500 nm wavelength range with a spectral resolution of 10 nm. Sample measurements were collected at the mine site using a contact probe to ensure consistent illumination conditions in core samples. Since vein mineralogy was dominantly quartz, the analysis targeted mostly areas of wall rock and vein alteration halos. Optimization was done at the start of every analysis run, and white references were collected every ~ 20 minutes to monitor the effect of instrument drift.

Spectral processing was accomplished using The Spectral Geologist (TSG) software. Scalars for absorption feature positions and relative depths were extracted from hull quotient-corrected spectra (AusSpec International, 2008). The scalar for the AlOH absorption feature position was created using the TSG PFIT function to measure the wavelength at reflectance minimum by applying a 5th-order polynomial fitting curve to the reflectance spectrum over the range 2174-2230 nm and focused between 2184-2224 nm. A spectral feature depth filter of 0.02 was applied to remove background noise. The scalar for the MgOH-CO_3 absorption feature was created using the TSG PROFILE function to measure the wavelength at reflectance minimum centred at 2335 nm with a search radius of 35 nm. The scalar for the FeOH absorption feature was created using the PROFILE function to measure the wavelength at reflectance minimum centred at 2255 nm with a search radius of 15 nm.

Both white mica crystallinity and Fe-slope scalars are unit-less quantities derived from reflectance values of measured spectra. White mica crystallinity was calculated from the relative depth of the 2200 nm feature divided by the relative depth of the 1900 nm feature taken from the hull quotient-corrected reflectance spectrum (Fig. 2.18) (AusSpec International, 2008). The Fe-slope scalar was calculated from the mean reflectance value at 1650 nm divided by the mean reflectance value at 1350 nm taken from the reflectance spectrum with no hull correction (AusSpec International, 2008). SWIR scalars are reported in Appendix A.

2.7.2 Results

The wavelength position of the 2200nm AlOH absorption features at Pine Cove varies from 2190 to 2222 nm (Fig. 2.19A). Samples are broadly grouped by AlOH wavelength position: < 2195 nm have paragonitic mica, 2195 – 2208 nm have muscovitic mica, and > 2208 nm have phengitic mica (Fig. 2.19B). Gold mineralization is associated with mixed paragonitic-muscovitic to muscovitic AlOH absorption features (~ 2195 to 2205 nm). Samples with Au > 0.02 ppm display minima between 2192 and 2205 nm, whereas samples with Au > 0.5 ppm exclusively display minima between 2196 and 2201 nm (Fig. 2.19B). White mica crystallinity varies from 0.007 to 5.7 and generally increases with proximity to mineralization; however, there are exceptions to this pattern in argillaceous rocks. The wavelength position of the FeOH (2255 nm) and MgOH-CO_3 (2335 nm) SWIR absorption features do not show systematic variation with alteration indices or mineralization, and were not used in further analysis. However, the relative depths of both the FeOH and MgOH-CO_3 features decrease with increasing CO_2 and K_2O, likely indicating pyroxene and/or chlorite replacement by carbonate and/or sericite.

Carbonate SWIR features are commonly not detectable in the fine-grained alteration assemblage at Pine Cove, but increasing Fe-slopes generally coincide with sericite alteration. Fe-bearing calcite also produces a relatively weak Fe^{2+} response, so this parameter alone does not define a good vector at Pine Cove. Instead, Au-mineralized samples generally have an increase in Fe^{2+} response (Fe-slope) and a decrease in the depth of the MgOH absorption feature at 2335 nm (Fig. 2.19C). This results in elevated

Fe-slope/MgOH-depth ratios, which can be correlated to increasing alteration as measured by $K_2O + CO_2/K_2O + CO_2 + Na_2O + Al_2O_3$ (ACI; Fig. 2.19D). Figure 2.20 shows that Fe-slope/MgOH-depth > 5.5 commonly coincides with Au ore zones. This suggests that the Fe-slope/MgOH-depth SWIR parameter can potentially be used as a proxy for carbonate-sericite alteration in certain districts, and further that it reflects the combination of white mica alteration and ferro-calcite.

2.8 Electron Microprobe Analysis

Electron microprobe analysis (EMPA) of 11 polished thin sections was conducted to investigate the relationship of white mica and carbonate compositional changes to variations in SWIR spectral parameters. Results of the electron microprobe analyses are reported in Appendix C. White mica compositions were calculated assuming 11 oxygens in the mineral formula and all Fe as Fe^{2+} (Buschette and Piercey, 2016). White mica compositions at Pine Cove are predominantly controlled by the Tschermak substitution ($Al^{VI} + Al^{IV} \leftrightarrow [Fe^{2+},Mg]^{VI} + Si^{IV}$) (Fig. 2.21A) and the simple substitution of Na^+ for K^+. The chemical compositions of white mica as measured by EMPA show that Fe, Mg, Al^{VI}, K, and Na vary systematically with AlOH absorption feature wavelengths and Au content (Fig. 2.21B-F). Longer wavelengths are associated with higher Fe and Mg, whereas shorter wavelengths are associated with higher Na and Al^{VI}. Micas associated with Au mineralization have low Fe+Mg+Si+Mn contents, and are K-rich white micas (i.e., muscovite).

Chlorite compositions were calculated assuming 14 oxygens in the mineral formula and all Fe as Fe^{2+} (Buschette and Piercey, 2016). Chlorites do not show systematic changes in composition with alteration; however, chlorites in the Bobby Cove Formation have higher Mg and Cr relative to chlorites in the Venam's Bight Formation and gabbros.

Due to the prevalence of calcite at Pine Cove, carbonate compositions were calculated assuming 3 oxygens in the mineral formula. Calcite at Pine Cove typically contains approximately 0.2 to 2 wt.% Mn+Fe+Mg. The maximum Mn, Fe, and Mg composition of calcite at Pine Cove are 0.15, 0.08, and 0.015 atoms per formula unit, respectively. Overall, Au >0.5 ppm mineralization is associated with calcite and ferro-calcite. Fe and Mg generally increase with increasing Fe-slope and CO_2/Ca (Fig. 2.22A-D). Ankerite from intermediate to proximal alteration is not associated with Au >0.5 ppm mineralization (Fig. 2.22C-D).

Rutile and titanite were also analysed to determine whether changes in composition of these phases correlates with alteration or gold mineralization. No conclusive systematic changes in either of these phases were identified from the EMPA analyses; however, the small grain size in some samples limited the number of suitable analyses. Additionally, Na and Al were not analysed for a few titanite samples, further limiting interpretation of this data. As such, data from these phases are reported in Appendix C but are not discussed further in this study.

Pyrite and chalcopyrite are the predominant sulphides at Pine Cove as measured by EMPA, though a sample of least-altered Bobby Cove Formation contains a sulphide mineral comprising approximately 33% arsenic and which is here interpreted to be a variety of arsenian pyrite. However, the EMPA analyses also show that approximately

40-45% of the composition of this mineral is unidentified (Appendix C.6). This mineral shows that arsenian sulphides occur in least-altered volcaniclastic rocks at Pine Cove, but further analyses is required to determine the complete composition of the mineral and to determine its role in the apparent depletion of As at Pine Cove.

2.9 Discussion

2.9.1 Comparison to Regional Stratigraphy

Skulski et al. (2010) showed that the stratigraphy of the Snooks Arm Group defined at the Betts Cove Complex can be correlated across the Baie Verte Peninsula. Results of core logging and lithogeochemical analyses at Pine Cove suggest that the deposit is hosted within correlative units of the Snooks Arm group, with most mineralization hosted in the Venam’s Bight Formation and lesser mineralization occurring within the Bobby Cove Formation. At Betts Cove, the Bobby Cove Formation overlies the Venam's Bight Formation; however, at Pine Cove, lithology textures, mineralogy, and geochemistry indicate that this sequence is overturned. Due to the textural, mineralogical, and geochemical similarity of the Venam’s Bight Formation with other tholeiitic basalt sequences in the Snooks Arm Group, it is instructive to also evaluate the stratigraphy of the Bobby Cove Formation.

The stratigraphy of the Bobby Cove Formation is broadly defined by a calc-alkaline volcaniclastic lower member overlain by a turbiditic upper member that is capped by red argillite or iron formation locally (Cousineau and Bédard, 2000; Skulski et al., 2010). However, at Pine Cove, turbiditic greywacke typically occurs structurally below argillite, which itself occurs below calc-alkaline volcaniclastic rocks. The calc-alkaline to transitional volcaniclastic rocks at Pine Cove correlate well with the lower member of the Bobby Cove Formation, and clinopyroxene-phyric lapilli tuff at Pine Cove is herein interpreted to correlate with the regional marker unit in the Bobby Cove Formation known as the East Pond Member (Skulski et al., 2010). The maroon argillite is interpreted to correlate with the intermediate mudstone-tuffaceous sandstone facies of the Bobby Cove Formation; a bulk composition reflecting possible derivation from the Bobby Cove Formation supports this interpretation (Fig. 2.11F and 2.12). The greywacke at Pine Cove likely represents the sedimentary rock-dominated intermediate and upper members of the Bobby Cove Formation (Cousineau and Bédard, 2000).

The lithogeochemistry of the Venam's Bight Formation, internal stratigraphy of the Bobby Cove Formation, and inverse-graded beds in the greywacke of the Bobby Cove Formation confirm that the stratigraphic sequence at Pine Cove is overturned. Immobile element geochemistry of tholeiitic basaltic rocks at Pine Cove correlate with the signature of the Venam's Bight Formation, but occur below the Bobby Cove Formation. In addition, volcanic and sedimentary units within the Bobby Cove Formation at Pine Cove occur in reverse order to the typical Bobby Cove Formation sequence. The Scrape thrust fault truncates this sequence and juxtaposes Venam's Bight Formation over amphibolitic rocks interpreted to correlate with the Mount Misery Formation.

2.9.2 Genetic Model

Previous studies have attributed gold mineralization at Pine Cove to deformation along the Scrape thrust fault during Silurian transpression (Calon and Weick, 1990;

Castonguay et al., 2009; Skulski et al., 2010; Kerr & Selby, 2011), and results from this study are in agreement with this interpretation. Gold mineralization is spatially associated with deformed phyllonite in the hanging wall of the Scrape thrust fault, suggesting that mineralization is coupled to the processes that formed the phyllonite. Figure 2.23 shows the schematic spatial relationships between rock types, alteration, and mineralization. The phyllonite exhibits strong sericite-rutile-carbonate alteration and contains abundant folded±boudinaged±brecciated quartz veins, although significant Au mineralization is rare to absent in the phyllonite. A majority of veins and mineralization are located at lithologic contacts in the hanging wall of the phyllonite. This suggests that, at the time of Au mineralization, strain was too high within the phyllonite zone to allow the brittle injection of auriferous fluids. Instead, hydrofracturing was assisted by the rheological contrast between adjacent units in the hanging wall of the Scrape thrust fault. Porosity likely developed as a result of the rheological anisotropy between relatively rigid gabbros and softer volcano-sedimentary rocks during shearing, allowing injection of the CO_2-H_2O-Si-K-Au-rich fluids (Ridley, 1993; McCuaig and Kerrich, 1998; Dubé and Gosselin, 2007). Variably deformed quartz breccia-veins enveloped by ductile alteration halo fabrics indicate that cyclic fluctuations between brittle hydraulic fracturing and ductile deformation (McCuaig and Kerrich, 1998) occurred during progressive deformation along the Scrape thrust fault. Moreover, precipitation of Au was driven by the sulfidation of the surrounding high-Fe basalts and syn-volcanic gabbros (e.g., Williams-Jones et al., 2009). Similar processes have been observed in the nearby Stog'er Tight deposit (Ramezani et al., 2000), deposits in Western Australia (Phillips et al., 1996), and other orogenic gold provinces globally (Ropchan et al., 2002; Mernagh and Bierlein, 2008).

Continued post-mineralization deformation is evidenced by strongly folded and/or brecciated quartz veins within the hanging wall of the Scrape thrust fault. Although the Scrape thrust fault zone exhibits south-directed reverse-sense shear indicators (Castonguay et al., 2009), it juxtaposes greenschist-grade rocks over amphibolite-grade rocks. This low over high metamorphic grade relationship across the Scrape thrust fault suggests that it was reactivated as an extensional fault, likely during Devonian transtension (Anderson et al., 2001; Castonguay et al., 2009). Amphibolitic rocks immediately below the Scrape thrust fault commonly contain barren disseminated pyrrhotite and pyrite. Assuming a metamorphic devolatization model for the source of mineralizing fluids (i.e., Groves et al., 1998; Goldfarb et al., 2001; Pitcairn, 2006; Phillips and Powell, 2010; Pitcairn, 2014), this raises the possibility that mineralized rocks have been juxtaposed against original source rocks during later extensional faulting. However, further data is necessary to assess the geochemistry and regional context of the amphibolitic rocks.

2.9.3 Controls on Alteration and Mineralization

Although epidote and titanite often occur as metamorphic minerals in greenschist-grade rocks, we propose that the majority of epidote and titanite observed in the Pine Cove deposit is of hydrothermal origin. For distal alteration, mineral assemblages and mass balance calculations suggest that reactions were isochemical with the exception of the addition of CO_2 and H_2O. The formation of the distal alteration assemblages can be modelled by the following equations that reflect the addition of CO_2 and H_2O:

(1) $5Ca_{0.6}Na_{0.4}AlSi_3O_{8\ (plagioclase)} + CO_2 + 2H_2O$

$= Ca_2Al_3Si_3O_{12}(OH)_{(epidote)} + 2NaAlSi_3O_{8\ (albite)} + 6SiO_{2\ (quartz)} + CaCO_{3\ (calcite)} + H^+$

(2) $4CaMgAl_{0.5}Si_{1.5}O_{6\ (augite)} + Fe_3O_{4\ (magnetite)} + FeTiO_{3\ (ilmenite)} + 3CO_2 + 4H_2O =$ $Mg_{2.5}Fe_{2.5}Al_2Si_3O_{10}(OH)_{8\ (chlorite)} + CaTiSiO_{5\ (titanite)} + 3CaCO_{3\ (calcite)} + 2SiO_{2\ (quartz)} +$ $1.5Fe^{2+} + 1.5Mg^{2+} + 2O^{2-}$

With increasing proximity to mineralization, alteration of mafic and oxide minerals in the host rocks coincided with increased deformation and progressively increased CO_2 to form a rutile-calcite-chlorite assemblage:

(3) $4CaMgAl_{0.5}Si_{1.5}O_{6\ (augite)} + Fe_3O_{4\ (magnetite)} + FeTiO_{3\ (ilmenite)} + 4CO_2 + 4H_2O =$ $Mg_2Fe_3Al_2Si_3O_{10}(OH)_{8\ (chlorite)} + TiO_{2\ (rutile)} + 4CaCO_{3\ (calcite)} + 3SiO_{2\ (quartz)} + Fe^{2+}$ $+ 2Mg^{2+} + 5O^{2-}$

and

(4) $CaTiSiO_{5\ (titanite)} + CO_2 = TiO_{2\ (rutile)} + CaCO_{3\ (calcite)} + SiO_{2\ (quartz)}$

Further, the addition of K to the Pine Cove host rocks results in the formation of sericite (and calcite) proximal to mineralization:

(5) $6Ca_{0.5}Na_{0.5}AlSi_3O_{8\ (plagioclase)} + 3K^+ + 6H^+ + 3CO_2 = 3KAl_2AlSi_3O_{10}(OH)_2$ $_{(muscovite)} + 9SiO_{2\ (quartz)} + 2CaCO_{3\ (calcite)} + Ca^{2+} + 3Na^+$

and/or

(6) $3NaAlSi_3O_{8\ (albite)} + K^+ + 2H^+ = KAl_2AlSi_3O_{10}(OH)_{2\ (muscovite)} + 6SiO_{2\ (quartz)} + 3Na^+$

Excess Fe, Mg, and O generated from equations 2 and 3 were likely consumed during the formation of chlorite, pyrite, and minor dolomite and phengite.

Despite the abundance of albite in both distal and proximal rocks, a comparison of Na content relative to background values in the Snooks Arm Group (Bédard et al., 2000) shows that no significant amount of Na was added during albitization. In fact, Na is commonly depleted in proximal alteration (Fig. 2.15B), likely reflecting the replacement of albite by sericite (Eq. 6); the exception is the addition of Na to form pink albite in quartz veins and/or vein selvages.

The process that resulted in a net loss of As and Sb is not fully understood. The As-Sb depletion patterns at Pine Cove are atypical of orogenic gold systems, which are commonly enriched in As-Sb relative to background abundances (McCuaig and Kerrich, 1998). It is possible that the depletion of As and Sb is attributed to the dissolution of previously formed As±Sb-bearing sulphides and/or remobilization of As-Sb from other phases (such as apatite).

Cr has been shown to be mobile in CO_2-rich fluids (Dinel et al., 2008; Emam and Zoheir, 2012), and the apparent local depletion in Cr from mass balance calculations at Pine Cove (Fig. 2.15B) is attributed to the dissolution of accessory chromite in Bobby Cove Formation tuffs during hydrothermal alteration. During this process, some of the remobilized Cr substituted into sericite, producing fuchsite (e.g., sample PC-180-025; Appendix C.1) and local minor mass gains of Cr.

The strong textural association of pyrite and Au mineralization in high-Fe-Ti altered wall rock indicates that wall rock sulfidation was the primary mechanism for Au deposition at Pine Cove (Mikucki, 1998; Williams-Jones et al., 2009). Tuffs of the Bobby Cove Formation are comparatively Fe-poor, relative to the Venam's Bight Formation and gabbro sills, and generally lack gold mineralization. However, no direct evidence of sulfidation of Fe-Ti oxides is observed at Pine Cove (e.g., pyrite rimming magnetite). This can be explained, however, by the close spatial association of pyrite with skeletal rutile, which is interpreted to have formed from pre-existing Fe-Ti oxides. Iron was likely re-mobilized during the breakdown of Ti-bearing magnetite (Eq. 2 and 3) on a mm to m scale, where it bonded with S to form pyrite via the reaction:

(7) $FeTiO_{3\ (ilmenite)} + 2H_2S = FeS_{2\ (pyrite)} + TiO_{2\ (rutile)} + H_2O + 2H^+$

Similarly, magnetite porphyroblasts in distal to intermediate rocks are interpreted to have formed from excess Fe liberated during the destruction of Ti-magnetite.

Since gold was likely transported as a bisulfide complex (Mikucki, 1998; Williams-Jones et al., 2009), precipitation of gold was driven by an activity decrease in the HS^- ligand during pyritization outlined in equation (7) above:

(8) $Au(HS)_2^- + H^+ + 1/2H_{2\ (g)} = Au_{(s)} + 2H_2S$

Wall rock sulfidation may also have been complimented by flash vaporization (i.e., phase separation) during episodic brittle deformation (Weatherley and Henley, 2013). Sudden decreases in pressure would have resulted in the rapid precipitation of silica and dissolved metals, as well as lowering the activity of HS^-, promoting the precipitation of gold (Williams-Jones et al., 2009). The presence of abundant quartz veining coupled with gold-hosting pyrite is consistent with both wall rock sulfidation accompanied by flash vapourization/pressure release during deformation leading to gold deposition.

2.9.4 Mineral Chemistry

White micas: The various physicochemical controls that can affect the composition of white micas in the orogenic gold environment include fluid composition, temperature, pressure, pH, and wall rock composition (Henley, 1970; Duke, 1994; Bierwirth et al, 2002; Yang et al., 2011; Halley et al., 2015; Wang et al., 2017). In the metamorphic environment, high-Al^{VI} (Duke, 1994) and high-Na (Henley, 1970) white mica has been related to increasing metamorphic grade. In hydrothermal environments, Tschermak substitution in the muscovite-phengite solid solution series is attributed to changes in pH and the activity of Fe, Mg, and Si in the ore-forming fluids (Yang et al., 2011; Halley et al. 2015; Wang et al., 2017). In general, muscovite is more stable in acidic environments with relatively low activity of Fe+Mg+Si, whereas phengitic compositions are favored in more neutral environments and higher activity of Fe+Mg+Si (Halley et al. 2015; Wang et al., 2017). In addition, wall rock composition and fluid/rock also influence the composition of white micas. The geochemical buffering capacity of the wall rocks increases with decreasing fluid/rock away from the central fluid conduits; this increases pH and consequently favors phengitic compositions (Halley et al. 2015).

White mica compositions at Pine Cove are controlled by both the Tschermak substitution ($Al^{VI} + Al^{IV} \leftrightarrow [Fe^{2+},Mg]^{VI} + Si^{IV}$) and the simple substitution of Na^+ for K^+ (Fig. 2.21A). Integration of SWIR and EPMA results confirms that white micas with shorter wavelength AlOH absorption features are more Na-rich, whereas micas with longer wavelength AlOH absorption features contain more Fe+Mg+Si (Fig. 2.21A-F). Overall, muscovite and mixed muscovite-paragonite are the dominant white mica species at Pine Cove. White mica (sericite) alteration is generally restricted to proximally-altered rocks, but minor sericite in distal volcanic and sedimentary rocks is typically phengitic (i.e., high Fe+Mg+Si). Approaching mineralization, sericite compositions vary from paragonitic to muscovitic, whereas ore samples contain exclusively muscovite.

The progression from phengite → paragonitic muscovite → muscovite with decreasing distance to mineralization is likely a reflection of decreasing pH at higher fluid/rock with proximity to the Scrape thrust fault. Distal phengitic micas are interpreted to reflect a more neutral pH environment due to rock-buffering at low fluid/rock. With increasing deformation and moderate fluid/rock, fluids were partially buffered by albite in wall rock and paragonitic muscovite was stable. At the highest fluid/rock along the centers of fluid flow channels, the buffering capacity of wall rocks was overcome, and white mica phases evolved toward the inferred composition of the fluid (relatively high K-activity, relatively low-pH). The predominance of high-Al white mica associated with abundant quartz veins in high-Fe wall rocks suggests that the activity of Fe+Mg+Si had a relatively minor role in determining white mica compositions at Pine Cove.

Chlorite: At Pine Cove, the composition of chlorites is predominantly controlled by wall-rock composition. Chlorite lacks the systematic changes in composition with proximity to mineralization that is seen in white micas. Although chlorites in other deposits may show Mg-enrichment proximal to mineralization, due to sulfidation of Fe-silicates (e.g., McCuaig and Kerrich, 1998), proximal chlorites at Pine Cove are not Mg-rich relative to distal chlorites. Fe-rich chlorite exhibiting anomalous purple-blue birefringence occurs in proximal alteration, but this phase seems to be minor relative to FeMg-chlorite. Variations in chlorite SWIR parameters are primarily due to rock composition and/or formation of sericite (e.g., the depth of the MgOH absorption feature decreases with increasing sericite abundance), rather than due to variations associated with physicochemical conditions of chlorite formation during Au deposition.

Carbonate: Although gold mineralization in greenschist facies orogenic gold systems is typically associated with Fe-carbonate minerals (e.g., ankerite; McCuaig and Kerrich, 1998; Dubé and Gosselin, 2007), the predominant carbonate in all rock types at Pine Cove is calcite. Electron probe microanalysis confirms that calcite is the dominant carbonate mineral associated with Au mineralization (Fig. 2.22), which commonly contains trace amounts of Fe ± Mn (Appendix C.3). The Fe^{2+}-slope SWIR index generally correlates with Fe+Mg content in carbonates; however, Au values do not increase with increasing Fe^{2+}-slope SWIR index, reflecting the association of calcite with mineralization, rather than Fe-carbonates. Nevertheless, ankerite does occur as carbonate alteration in the Bobby Cove Formation and early-formed (pre-mineralization?) carbonate porphyroblasts. The Fe-carbonate porphyroblasts may be the product of

Silurian regional metamorphism, as is reported in other parts of central Newfoundland (e.g. van Staal, 2007; Piercey et al., 2014). High Fe^{2+}-slope values (>1.3) are associated with mixed muscovite-paragonitic muscovite in proximal alteration, indicating that at least some FeMg-carbonate is likely concurrent with both sericite alteration and Au mineralization. The minor amounts of FeMg-carbonate in proximal alteration possibly formed from excess Fe-Mg liberated during calcite-chlorite-leucoxene alteration (Eq. 2 and 3).

Ankerite alteration in the Bobby Cove Formation and early carbonate porphyroblasts are interpreted to have formed nearer to equilibrium with the wall rock at lower fluid/rock (i.e., buffered by rock composition). Later calcite alteration is likely the result of increasing fluid/rock but at relatively low Fe-Mg activities. Although the high-Fe±Mg rocks at Pine Cove should favour formation of FeMg-carbonates during alteration, the predominance of calcite indicates that Fe-Mg activity was buffered by the formation of pyrite and chlorite. This interpretation is supported by the relatively low-Fe+Mg+Si composition of white micas in proximal alteration.

2.9.6 Vectors

There is an extensive alteration halo associated with CO_2+K-rich fluid flow during protracted deformation along the Scrape thrust fault. Defining gradients towards ore is complicated by variations in lithology, overlapping multi-generational mineralizing structures, and post-mineral deformation. However, consistent vectors can be identified. In particular, the mineralogy and geochemical patterns displayed in the least structurally-disrupted drill hole PC-14-236 are interpreted to be representative of alteration around mineralizing structures (Fig. 2.17). Schematic spatial changes in mineral assemblages, geochemistry, and SWIR indices are illustrated in Figure 2.23.

Geochemistry: The most consistent geochemical parameters that define haloes around mineralization at Pine Cove are enrichment of CO_2+K+Rb, and depletion of As+Sb±Na. Although As and Sb have low overall concentrations, these elements appear to be important to exploration for Pine Cove-type mineralization. The alkali-carbonate index [$K_2O + CO_2 / K_2O + CO_2 + Na_2O + Al_2O_3$] is considered the best geochemical measure of carbonate and sericite alteration. Additionally, the calcite saturation index [$CO_2/Ca = 1$] typically defines a halo of calcite alteration up to 50 m from mineralization, whereas other carbonate alteration indices are less consistent or show similar patterns to CO_2. W, Bi, Se, Te, and Pb are commonly enriched proximal to mineralization, but generally do not significantly extend beyond the zones of anomalous Au enrichment. The generalized sequence from the spatially distal to proximal to mineralization is: CO_2 enrichment + As-Sb depletion → K-Rb enrichment → Na depletion → W±Pb±Ba enrichment → Au.

Visual mineralogy: The distal epidote-titanite assemblage may extend up to 500 m from ore, but this is not well constrained and is likely variable. Regional metamorphism complicates the spatial relation of distal alteration assemblages to mineralization and presents difficulties in discerning hydrothermal alteration. Since distal alteration assemblages are similar to regional greenschist mineralogy, the best indicator of hydrothermal alteration in distal mineral assemblages is bulk geochemistry (i.e., As-Sb depletion coincident with CO_2 enrichment).

Beige-colored sericite along foliation and orange-weathering skeletal rutile are typically good indications of proximity to mineralization, though the extent of this assemblage is highly variable. Sericite-rutile alteration extends as much as 25 m from mineralizing quartz veins, but in some locations extends less than 5 m from mineralization. The extent of sericite alteration is commonly more visually apparent in porous sedimentary units, such as the greywacke member of the Bobby Cove Formation.

SWIR parameters: SWIR spectrometry is a reliable technique for mapping the composition of white micas, and is particularly useful where sericite alteration is too fine-grained to identify by hand lens. The identification of sericite alteration in ambiently greenschist facies metabasic rocks is a potential indicator of proximity to potential ore-forming fluid conduits in orogenic Au systems. For deposits similar to Pine Cove, the progression from phengite → paragonitic muscovite → muscovite approaching mineralization may be a useful exploration vector. However, due to the complex interplay of various parameters that determine white mica compositions, care should be taken during interpretation of patterns. Alternative patterns may be present in deposits that formed under different physicochemical conditions (e.g., Wang et al., 2017).

Since calcite is associated with mineralization at Pine Cove, the Fe-slope SWIR index alone is not a useful vector. However, a positive correlation exists between the Fe-slope/MgOH-depth and the alkali-carbonate alteration index (ACI) of Bierlein et al. (2000) (Fig. 2.19D). Additionally, alkali-carbonate alteration index > 0.2 and Fe-slope/MgOH-depth > 5.5 commonly overlap with anomalous to ore grade Au mineralization (Fig. 2.20). The Fe-slope/MgOH-depth is interpreted to be controlled by the relative proportions of Fe-bearing carbonate and sericite versus chlorite. We propose that the Fe-slope/MgOH-depth may be useful as a SWIR index for carbonate+sericite alteration in greenschist facies rocks. However, the influence of other factors (e.g., other ferric minerals) on this index should also be assessed before applying it blindly to exploration programs.

2.10 Conclusions

New geochemical data and logging of volcano-sedimentary stratigraphy at Pine Cove demonstrates that the deposit is situated within an overturned sequence of Venam's Bight Formation and Bobby Cove Formation of the Snooks Arm Group, Baie Verte region, Newfoundland Appalachians. The deposit is predominantly hosted in gabbro sills and basalts of the Venam's Bight Formation. Venam's Bight volcanic rocks can readily be distinguished from Bobby Cove volcanic rocks by immobile lithogeochemistry (e.g., Ti/Zr, V/Ti ratios).

Mineralized quartz veins were emplaced along lithologic contacts in response to anisotropic deformation of rigid gabbros and surrounding volcano-sedimentary rocks in the hanging wall of the Scrape thrust fault, likely during Silurian (Salinic) orogenesis (Calon and Weick, 1990; Castonguay et al., 2009; Skulski et al., 2010; Kerr & Selby, 2011). Episodic fluctuations between brittle hydraulic fracturing and ductile deformation resulted in overlapping, multi-generational quartz-calcite-chlorite±albite breccia veins with sericite-rutile-calcite-pyrite alteration selvages. Gold precipitation was driven by sulfidation of high-Fe-Ti gabbros and basalts of the Venam's Bight Formation.

Integrated visible alteration, geochemistry, EMPA, and SWIR analyses significantly extend the footprint beyond what has been previously identified. Alteration assemblages broadly consist of distal epidote-titanite-chlorite-carbonate, intermediate carbonate-chlorite, and proximal sericite-rutile-chlorite-carbonate. The dominant carbonate phase associated with mineralization is calcite. Distal alteration assemblages may extend as much as 500 m from ore, whereas sericite-rutile alteration generally extends less than 25 m from mineralization.

Hydrothermal alteration primarily involved the enrichment of CO_2-K-Rb±S±Au ±W±Pb±Ba±In and depletion of As-Sb-Na. REEs, HFSEs, Al, and most transition metals were generally immobile during alteration, although Cr and Cu may be slightly depleted. The most extensive geochemical signature is As-Sb depletion + CO_2 enrichment, which extends up to ~50 m from mineralization. The molar ratio $CO_2/Ca = 1$ also defines a halo of calcite alteration up to 50 m from mineralization. The generalized distal to proximal variation in alteration geochemistry is: CO_2 enrichment + As-Sb depletion → K-Rb enrichment → Na depletion → W±Pb±Ba enrichment → Au. In general, the alkali-carbonate index $K_2O + CO_2 / K_2O + CO_2 + Na_2O + Al_2O_3$ of Bierlein et al. (2000) coupled with As-Sb depletion is considered the most consistent metric of ore-related alteration at Pine Cove. However, the overall concentrations of As and Sb are low and these elements are not typically depleted in orogenic gold systems, so application of this vector may be limited to Pine Cove-type mineralization.

SWIR data show distinct trends that correlate with mineralization, alteration assemblages, and geochemistry. Comparison to EMPA data shows that the wavelengths of AlOH absorption features are coupled to the Tschermak substitution and K/Na content in white micas. White micas in ore zones at Pine Cove are dominated by muscovite (high-K, high-Al) with AlOH-wavelengths between 2195 and 2202 nm. In contrast, white micas in surrounding proximal sericite alteration are typically paragonitic muscovite (relatively high-Na, high-Al) with AlOH-wavelengths between 2190 and 2205 nm. Distal white micas are generally phengitic (high-Fe+Mg, Al-poor) and have AlOH-wavelengths >2205 nm. The progression from phengite → paragonitic muscovite → muscovite at Pine Cove is interpreted to reflect decreasing pH with increasing fluid/rock ratios approaching fluid flow channels. Mapping of white mica compositions can be a valuable tool for orogenic gold exploration, but it is important to understand that the physicochemical factors that influence white mica compositions may vary from deposit to deposit.

A potential SWIR index that is sensitive to both Fe-carbonate and sericite alteration is the Fe-slope/MgOH-depth. At Pine Cove, this index measures the relative proportion of (Fe-carbonate + sericite)/chlorite. The Fe-slope/MgOH-depth index may be a useful metric for combined carbonate+sericite alteration in greenschist facies rocks; however, further studies are warranted to demonstrate the reliability of this index.

Table 2.1 Representative Geochemical Analyses Results

Hole ID		PC-14-225	PC-14-236	PC-13-198	Surface	PC-14-225	Surface	Surface	PC-04-148	PC-14-227	PC-11-185	PC-13-204	PC-13-209
Sample ID		PC-225-004	PC-236-006	PC-198-010	PCM-012	PC-225-002	PCM-017	PCM-005	PC-148-002	PC-227-001	PC-185-013	PC-204-002	PC-209-016
Depth (m)		38.85	81.4	139.75		12.8			28.6	9.2	102	42.6	192.4
UTM NAD 83 Zone 21		-	-	-	562951 E 5534747 N	-	562976 E 5534809 N	562617 E 5534626 N	-	-	-	-	-
Lithology		BCF-ABLT	BCF-CCLT	gabbro - A	gabbro - B	gabbro - C	VBF-A	VBF-B	VBF-C	VBF-D	amphibolite	greywacke	maroon argillite
Alteration		Least Altered Epid-Tit	Least Altered Epid-Tit	Least Altered Epid-Tit	Least Altered Epid-Tit	Least Altered Epid-Tit	Least Altered Epid-Tit	Least Altered Epid-Tit	Least Altered Epid-Tit	Least Altered Epid-Tit	Distal Epid-Tit	Distal Epid-Tit	Distal Epid-Tit
SiO_2	%	55.6	50	47.3	48.6	50	47.5	47.2	49.6	46.9	47.3	56.8	61.4
Al_2O_3	%	17.15	15.05	15.2	13.65	13.95	15.65	14.65	13.9	13.75	14.6	14.05	13.05
Fe_2O_3	%	6.75	9.64	11.5	12.5	14.65	10.95	12.35	13.45	15.15	12.85	8.92	10.65
CaO	%	6.18	7.16	10.35	10.8	5.17	7.73	12.4	10.05	8.51	10.65	3.73	1.46
MgO	%	4.9	9.44	6.11	7.42	3.89	8.43	7.63	5.49	5.35	7.05	5.08	4.26
Na_2O	%	6.28	4.15	2.17	2.46	5.23	3.3	1.24	2.04	2.97	2.57	4.91	2.7
K_2O	%	0.04	0.41	0.05	0.06	0.15	0.12	0.03	0.04	0.14	0.19	0.18	1.38
TiO_2	%	1.15	0.65	1.46	1.69	3.69	1.12	1.58	1.84	2.19	1.2	1.38	1.07
MnO	%	0.07	0.17	0.17	0.19	0.21	0.16	0.17	0.19	0.23	0.19	0.15	0.12
P_2O_5	%	0.19	0.07	0.17	0.17	0.37	0.1	0.16	0.3	0.25	0.08	0.18	0.16
SrO	%	0.02	0.02	0.04	0.05	0.02	0.03	0.04	0.04	0.03	0.03	0.01	<0.01
LOI	%	3.45	3	3.52	2.63	2.77	3.8	3.36	4.05	3.75	1.57	4.97	3.51
Total	%	101.8	99.83	98.06	100.24	100.11	99.01	100.85	101	99.24	98.3	100.39	99.8
S	%	0.01	0.01	0.16	<0.01	0.01	0.01	0.15	0.23	0.17	0.16	<0.01	0.01
Ba	ppm	19	81.2	12.4	14.9	64.7	33.1	7.3	18.5	109	16.3	28.1	207
Ce	ppm	32.3	11	14.7	17.8	44.9	10.4	16.5	26.8	26.8	6.2	20	35.5
Cr	ppm	120	410	140	180	10	900	270	90	50	160	240	130
Cs	ppm	0.69	1.01	0.08	0.06	0.89	0.08	0.02	0.07	0.72	0.05	0.09	0.83
Dy	ppm	3.8	2.72	4.22	5.09	7.89	3.25	4.55	6.3	6.82	4.4	4.89	4.68
Er	ppm	2.3	1.83	2.34	3.41	4.13	1.8	2.68	3.94	4.3	2.85	3.32	3.04
Eu	ppm	1.27	0.63	1.08	1.45	2.46	0.97	1.28	1.75	1.87	1.02	1.2	1.11
Ga	ppm	15.8	15.5	16.1	17.7	23	16.2	16.6	17.6	20.8	16.9	15	17.7
Gd	ppm	4	2.45	3.8	4.89	7.87	3.03	4.2	6.25	6.53	3.73	4.55	4.26
Ge	ppm	<5	<5	<5	<5	<5	<5	<5	<5	<5	<5	<5	<5
Hf	ppm	3.1	1.2	2.1	3.4	6.2	1.9	2.5	3.9	4	1.7	3.5	3.9
Ho	ppm	0.8	0.59	0.84	1.01	1.58	0.65	0.94	1.31	1.55	0.99	1.05	0.99
La	ppm	15.3	4.7	5.8	6.7	17.9	4.1	6.1	10.7	10.6	1.9	8.6	16.8
Lu	ppm	0.31	0.27	0.36	0.43	0.59	0.25	0.33	0.51	0.58	0.4	0.43	0.45
Nb	ppm	8.9	0.9	3.3	4.5	17.8	2.6	4	6.1	7.8	0.4	6.8	10.2
Nd	ppm	15.3	6.7	11	13.8	29.1	8.2	12.7	19	20.1	6.7	13.3	19.7
Pr	ppm	3.92	1.42	2.18	2.71	6.3	1.61	2.46	3.84	3.91	1.15	2.74	4.37
Rb	ppm	0.6	6.9	0.5	0.5	3	1.7	0.3	0.7	1.9	0.8	3	30.9
Sm	ppm	4.06	1.83	3.1	4.28	7.69	2.53	3.78	5.16	5.44	2.36	3.54	4.57
Sn	ppm	2	<1	1	1	2	1	1	1	1	1	1	1
Sr	ppm	170.5	168.5	328	401	199.5	294	347	371	304	208	94.5	51.1
Ta	ppm	0.5	0.1	0.2	0.3	1.1	0.2	0.2	0.2	0.4	<0.1	0.2	0.6
Tb	ppm	0.63	0.39	0.68	0.82	1.29	0.57	0.74	1.07	1.15	0.67	0.81	0.71
Th	ppm	3.68	1.06	0.54	0.52	1.44	0.29	0.5	0.93	0.98	0.11	1.34	3.47
Tm	ppm	0.31	0.27	0.35	0.47	0.62	0.25	0.38	0.54	0.57	0.41	0.44	0.41
U	ppm	2.66	0.48	0.21	0.17	0.58	0.12	0.15	0.39	0.37	0.06	0.81	1.58
V	ppm	172	223	339	410	323	290	368	372	459	377	218	184
W	ppm	1	1	<1	1	1	<1	<1	1	2	<1	2	1
Y	ppm	22	15.3	22.4	26.3	41.2	16.2	23.3	32.1	36.6	24.1	27.9	24.8
Yb	ppm	2.22	1.72	2.32	3.06	3.84	1.73	2.39	3.71	3.59	2.59	3.07	2.93
Zr	ppm	134	40	83	123	266	69	102	134	164	53	122	140
As	ppm	44.6	56.7	5.3	17	2.3	0.9	39.9	2.6	21.1	1.3	1.4	1
Bi	ppm	0.04	0.03	0.01	<0.01	<0.01	<0.01	0.01	0.04	0.02	<0.01	0.02	0.04
Hg	ppm	<0.005	<0.005	<0.005	<0.005	<0.005	<0.005	<0.005	<0.005	<0.005	<0.005	0.008	<0.005
In	ppm	0.022	0.005	0.011	0.012	0.038	0.015	0.012	0.018	0.016	0.014	0.061	0.032
Re	ppm	<0.001	<0.001	0.002	<0.001	0.002	<0.001	0.001	0.001	0.001	0.002	0.001	<0.001
Sb	ppm	0.37	0.16	0.26	0.13	0.5	0.16	0.41	0.32	0.42	0.14	0.12	0.13
Se	ppm	0.2	0.3	0.2	0.2	<0.2	<0.2	0.2	0.9	0.2	<0.2	0.4	0.2
Te	ppm	<0.01	<0.01	<0.01	<0.01	0.01	<0.01	0.03	0.01	0.02	0.01	0.02	0.03
Tl	ppm	<0.02	0.03	<0.02	<0.02	<0.02	<0.02	<0.02	<0.02	<0.02	<0.02	<0.02	0.03
Ag	ppm	<0.5	<0.5	<0.5	<0.5	<0.5	<0.5	<0.5	<0.5	<0.5	<0.5	<0.5	<0.5
Cd	ppm	<0.5	<0.5	<0.5	<0.5	<0.5	<0.5	<0.5	0.6	<0.5	<0.5	<0.5	<0.5
Co	ppm	17	41	35	28	34	43	42	38	38	46	28	26
Cu	ppm	34	93	71	72	42	157	130	47	79	74	122	64
Li	ppm	10	30	20	10	10	20	20	10	10	10	20	20
Mo	ppm	1	<1	1	<1	2	<1	1	<1	<1	1	1	1
Ni	ppm	48	160	44	35	2	101	61	23	26	66	68	66
Pb	ppm	3	<2	8	<2	3	3	5	4	3	<2	2	5
Sc	ppm	20	37	44	59	29	54	47	43	40	50	29	27
Zn	ppm	38	86	82	80	116	65	74	106	119	97	61	109
Au	ppm	<0.001	0.002	<0.001	<0.001	<0.001	<0.001	0.001	0.002	0.003	<0.001	0.003	<0.001
C	%	0.22	<0.05	0.18	<0.05	0.22	0.07	0.13	0.29	0.28	0.18	0.55	0.11
CO_2	%	0.8	<0.2	0.7	<0.2	0.8	0.3	0.5	1.1	1	0.7	2	0.4
AlOH-WL	nm	-	-	-	-	-	-	-	-	-	-	-	2218
AlOH-depth	%	-	-	-	-	-	-	-	-	-	-	-	0.14
FeOH-WL	nm	2254	2253	2255	2255	2254	2254	2255	2255	2257	2255	2257	2255
MgOH-WL	nm	2333	2338	2343	2328	2336	2332	2341	2341	2338	2318	2343	2344
Fe-slope/MgOH-depth		3.9	4.4	3.0	3.1	7.0	3.7	2.7	4.0	3.6	5.2	4.1	6.1

Abbreviations:
VBF = Venam's Bight Formation
BCF = Bobby Cove Formation
CCLT = clinopyroxene crystal-lapillil tuff
ABLT = amygdaloidal basalt lapilli tuff
Epid = epidote
Tit = titanite
Carb = carbonate
Ser = sericite
Rt = rutile

Table 2.1 Representative Geochemical Analyses Results

Hole ID		PC-14-225	PC-11-180	PC-05-166	PC-11-180	PC-13-200	PC-04-146	PC-89-020	PC-14-236	PC-14-236	PC-11-185	PC-12-193	PC-05-166
Sample ID		PC-225-007	PC-180-001	PC-166-004	PC-180-011	PC-200-010	PC-146-004	PC-20-004	PC-236-016	PC-236-019	PC-185-011	PC-193-001	PC-166-002
Depth (m)		69.25	13.7	70.85	118	97.5	37.25	77.75	264.9	303.2	91.4	5.7	37.7
UTM NAD 83 Zone 21		-	-	-	-	-	-	-	-	-	-	-	-
Lithology		BCF-ABLT	BCF-CCLT	gabbro - A	gabbro - B	gabbro - C	VBF-A	VBF-B	VBF-C	VBF-D	amphibolite	greywacke	maroon argillite
Alteration		Proximal Ser-Rt	Proximal Ser-Rt	Proximal Ser-Rt	Proximal Ser-Rt	Proximal Ser-Rt	Proximal Ser-Rt	Proximal Ser-Rt	Proximal Ser-Rt	Proximal Ser-Rt	Proximal Ser-Rt	Proximal Ser-Rt	Proximal Ser-Rt
SiO_2	%	40.4	40.9	46	43.4	38.2	43.1	43	45.2	41.3	45.3	51.8	60.8
Al_2O_3	%	12.6	14.5	15.2	15.65	14.7	16.1	14.6	12.35	11.8	14.35	13.55	15.6
Fe_2O_3	%	6.06	8.75	11.4	11.35	14.65	7.77	9.07	11.9	16.85	14.9	9.02	7.04
CaO	%	14.3	8.23	8.13	7.1	8	10.65	10.25	8.8	9.54	5.18	7.49	2.18
MgO	%	3.96	7.72	6.18	5.91	5.6	7	5.79	5.76	4.57	5.1	4.78	2.74
Na_2O	%	2.51	3.01	1.26	3.2	1.6	1.39	1.54	0.9	0.59	1.94	2.08	1.57
K_2O	%	1.24	1.6	0.78	1.33	1.45	0.65	1.67	1.22	1.55	0.67	1.24	3.51
TiO_2	%	0.72	0.76	1.29	1.86	3.94	1.01	1.18	1.57	2.57	1.49	1.32	0.56
MnO	%	0.13	0.15	0.15	0.18	0.22	0.13	0.13	0.18	0.23	0.16	0.15	0.23
P_2O_5	%	0.13	0.12	0.15	0.23	0.78	0.1	0.11	0.21	0.43	0.12	0.19	0.23
SrO	%	0.02	0.02	0.04	0.04	0.02	0.05	0.04	0.05	0.05	0.01	0.04	0.01
LOI	%	18.45	14.6	10.05	9.2	9.6	13	11.95	10.85	10.55	9.85	9.21	4.4
Total	%	100.58	100.42	100.66	99.49	98.78	100.98	99.38	99	100.04	99.07	100.92	98.91
S	%	<0.01	0.01	<0.01	0.02	0.15	0.04	0.07	0.08	0.25	0.51	0.06	<0.01
Ba	ppm	118	165	31	285	109	41.2	177	129	106.5	28.3	123	355
Ce	ppm	20.2	19.1	14	24.3	59.7	9.1	8.5	22.6	30.6	8.2	24	31.1
Cr	ppm	340	340	180	100	40	220	230	30	10	30	280	20
Cs	ppm	0.63	0.58	1.41	0.82	0.74	0.86	1.06	0.54	0.96	1.36	0.52	1.52
Dy	ppm	2.71	2.57	3.32	4.93	8.14	3.09	3.36	5.24	7.53	6	5.06	4.74
Er	ppm	1.73	1.47	2.11	2.95	4.19	1.82	2.09	3.23	4.73	3.96	3.1	2.99
Eu	ppm	0.77	0.84	0.96	1.64	2.98	0.91	0.88	1.49	2.15	0.81	1.38	1.21
Ga	ppm	10	15.8	16.9	21.8	23	15	15	17.5	22.3	19.6	15.1	16
Gd	ppm	2.78	2.6	3.59	5.06	9	2.88	3.09	4.88	7.48	4.67	4.53	4.74
Ge	ppm	<5	<5	<5	<5	<5	<5	<5	<5	<5	<5	<5	<5
Hf	ppm	1.9	2	2.1	3.2	7.1	1.8	2.3	3.4	4.4	2.2	3.1	2.7
Ho	ppm	0.57	0.51	0.69	1.07	1.7	0.63	0.67	1.11	1.64	1.29	1.13	0.99
La	ppm	9.6	8.8	5.3	9.7	24	3	2.8	9.5	12.3	2.5	10.3	12.6
Lu	ppm	0.23	0.23	0.31	0.39	0.57	0.28	0.27	0.49	0.66	0.56	0.39	0.39
Nb	ppm	5.1	5.3	2.8	6.5	22.3	1.7	2	4.4	6.5	0.6	7.7	3
Nd	ppm	9.8	10.7	10.4	16.5	38.7	7.2	7.7	15	21	8.9	14.2	18.5
Pr	ppm	2.46	2.36	2.11	3.45	8.17	1.47	1.4	3.18	4.47	1.5	3.24	3.97
Rb	ppm	20.7	27.6	18.1	24.4	24.2	12.8	30.3	23.9	29.3	15.9	20.8	85.7
Sm	ppm	2.36	2.37	3.1	4.47	9.31	2.45	2.34	4.26	6.13	3.29	4.12	4.29
Sn	ppm	1	1	1	1	2	1	1	1	2	1	1	1
Sr	ppm	189.5	154	338	330	202	391	388	424	451	69.2	355	88.6
Ta	ppm	0.3	0.3	0.2	0.3	1.5	0.1	0.1	0.3	0.5	<0.1	0.5	0.1
Tb	ppm	0.43	0.42	0.54	0.8	1.5	0.47	0.59	0.87	1.26	0.94	0.78	0.78
Th	ppm	2.11	2.22	0.56	0.75	1.48	0.11	0.14	1.26	1.24	0.18	1.34	2.99
Tm	ppm	0.24	0.21	0.3	0.4	0.62	0.26	0.28	0.51	0.65	0.58	0.43	0.44
U	ppm	1.71	0.82	0.19	0.29	0.55	0.07	0.1	0.51	0.52	0.1	0.85	0.66
V	ppm	117	217	296	370	378	188	208	320	472	446	259	116
W	ppm	10	10	3	12	14	2	5	30	21	1	2	3
Y	ppm	15.7	13.6	18.9	27.6	40.2	16.9	16.5	27.8	40	33.1	27.9	25.7
Yb	ppm	1.34	1.43	2.09	2.7	3.91	1.79	1.85	2.98	4.08	3.51	3	3.09
Zr	ppm	76	64	71	134	333	73	81	126	165	73	121	85
As	ppm	1.8	0.2	0.3	0.4	2	4.8	2	0.5	0.5	7.9	1.6	1
Bi	ppm	0.01	<0.01	0.03	0.01	0.05	0.01	0.02	0.03	0.05	0.07	0.03	0.03
Hg	ppm	<0.005	<0.005	0.005	<0.005	<0.005	<0.005	<0.005	<0.005	<0.005	<0.005	<0.005	0.007
In	ppm	0.024	0.024	0.03	0.028	0.077	0.03	0.028	0.033	0.065	0.071	0.028	0.017
Re	ppm	<0.001	<0.001	<0.001	0.001	0.001	<0.001	<0.001	0.001	0.007	0.002	<0.001	<0.001
Sb	ppm	0.09	0.09	0.06	0.08	<0.05	<0.05	<0.05	<0.05	0.06	0.12	<0.05	0.09
Se	ppm	0.2	<0.2	0.6	<0.2	<0.2	<0.2	0.6	0.7	0.8	0.2	0.4	0.3
Te	ppm	<0.01	0.03	0.08	<0.01	0.02	<0.01	0.01	0.03	0.03	0.03	0.03	<0.01
Tl	ppm	0.02	<0.02	0.02	<0.02	0.02	<0.02	0.02	<0.02	0.02	0.02	0.02	0.04
Ag	ppm	<0.5	<0.5	<0.5	<0.5	<0.5	<0.5	<0.5	<0.5	<0.5	<0.5	<0.5	<0.5
Cd	ppm	<0.5	<0.5	0.7	<0.5	<0.5	<0.5	<0.5	0.5	0.5	<0.5	<0.5	<0.5
Co	ppm	28	35	40	35	36	34	39	33	36	34	26	19
Cu	ppm	36	106	106	51	24	62	78	75	20	83	39	2
Li	ppm	10	20	50	30	30	40	30	30	40	30	30	20
Mo	ppm	1	<1	<1	1	2	<1	<1	<1	2	<1	1	<1
Ni	ppm	146	78	56	27	30	88	77	23	9	16	73	12
Pb	ppm	5	6	<2	5	7	2	5	4	3	<2	2	2
Sc	ppm	17	35	40	35	34	22	33	39	44	42	30	18
Zn	ppm	41	73	82	100	124	55	60	91	179	102	91	131
Au	ppm	<0.001	0.003	0.041	<0.001	0.003	<0.001	0.036	0.044	0.064	0.001	0.003	0.001
C	%	4.73	3.1	1.6	1.46	1.45	2.18	2.14	1.86	1.86	1.72	1.59	0.4
CO_2	%	17.3	11.3	5.9	5.3	5.3	8	7.8	6.8	6.8	6.3	5.8	1.5
AlOH-WL	nm	2195	2200	2192	2213	2199	2193	2196	2202	2202	2202	2199	2203
AlOH-depth	%	0.33	0.24	0.13	0.14	0.13	0.21	0.26	0.12	0.04	0.20	0.24	0.41
FeOH-WL	nm	-	2253	2255	2255	2255	2253	2253	2254	2257	2255	2251	-
MgOH-WL	nm	2339	2343	2344	2344	2343	2338	2345	2342	2347	2342	2340	2348
Fe-slope/MgOH-depth		8.8	5.5	7.2	4.5	6.7	5.5	5.2	6.8	11.5	5.4	5.1	4.6

Abbreviations:
VBF = Venam's Bight Formation
BCF = Bobby Cove Formation
CCLT = clinopyroxene crystal-lapillil tuff
ABLT = amygdaloidal basalt lapilli tuff
Epid = epidote
Tit = titanite
Carb = carbonate
Ser = sericite
Rt = rutile

Table 2.2 Averages of Electron Microprobe Analyses - White Micas

Hole ID	PC-14-236	PC-12-187	PC-12-293	PC-14-225	PC-11-180	PC-11-180	PC-14-236	PC-14-232	PC-89-029
Sample ID	PC-236-011	PC-187-010	PC-193-003	PC-225-007	PC-180-025	PC-180-002	PC-236-023	PC-232-010	PC-29-006
Depth (m)	168.4	136	23.65	69.25	244.5	18.9	309.1	66.7	83.4
Lith	maroon argillite	sediments and tuffs	greywacke	BCF-ABLT	VBF-B	BCF-CCLT	quartz breccia-veins	quartz breccia-veins	quartz breccia-veins
Alteration	distal	distal	proximal	proximal	proximal	proximal	proximal	proximal	proximal
Mineral	sericite	sericite	sericite	sericite	sericite	sericite	sericite	sericite	sericite
Analytical Spots	*n=6*	*n=6*	*n=9*	*n=10*	*n=7*	*n=11*	*n=10*	*n=9*	*n=5*
Major element (wt %)									
SiO_2	54.08	49.91	54.73	52.03	51.23	51.74	49.10	50.88	51.28
Al_2O_3	26.85	31.62	33.43	35.75	34.30	33.87	34.49	35.11	35.56
TiO_2	0.15	0.19	0.08	0.09	0.08	0.10	0.19	0.12	0.10
Cr_2O_3	0.01	0.01	0.94	0.35	1.97	0.18	0.01	0.00	0.01
V_2O_3	0.04	0.06	0.10	0.05	0.21	0.22	0.20	0.13	0.26
FeO	6.03	4.45	1.33	1.45	2.20	2.96	3.06	2.59	2.33
MnO	0.12	0.01	0.00	0.03	-0.02	0.01	0.00	0.00	0.00
CuO	0.00	0.01	0.00	0.00	0.03	0.00	-0.01	0.00	0.00
MgO	2.59	2.08	1.24	0.78	0.36	0.94	0.68	0.57	0.40
BaO	0.26	0.09	0.22	0.07	0.05	0.23	0.09	0.12	0.10
NiO	-0.01	0.00	0.00	0.01	0.02	0.00	-0.01	0.01	0.00
Na_2O	0.15	0.26	1.01	0.95	1.18	0.73	0.73	0.82	1.51
K_2O	9.82	9.27	8.79	8.59	8.56	9.15	9.40	8.98	8.53
F	-0.08	-0.10	0.00	-0.07	-0.12	-0.14	-0.07	-0.13	-0.13
Cl	0.01	0.01	0.02	0.01	0.00	0.00	0.01	0.01	0.00
Total	100.05	97.90	101.88	100.11	100.10	100.06	97.89	99.25	100.03
Atom per formula unit									
Si	3.48	3.25	3.35	3.24	3.25	3.27	3.18	3.23	3.22
Al^{VI}	1.51	1.68	1.77	1.87	1.79	1.79	1.81	1.85	1.86
Al^{IV}	0.52	0.75	0.65	0.76	0.75	0.73	0.82	0.77	0.78
Ti	0.01	0.01	0.00	0.00	0.00	0.00	0.01	0.01	0.00
Cr	0.00	0.00	0.05	0.02	0.04	0.01	0.00	0.00	0.00
V	0.00	0.00	0.00	0.00	0.01	0.01	0.01	0.01	0.01
Fe	0.32	0.25	0.07	0.08	0.14	0.16	0.17	0.14	0.12
Mn	0.01	0.00	0.00	0.00	0.00	0.00	0.00	0.00	0.00
Cu	0.00	0.00	0.00	0.00	0.00	0.00	0.00	0.00	0.00
Mg	0.25	0.21	0.11	0.07	0.07	0.09	0.07	0.05	0.04
Ba	0.01	0.00	0.01	0.00	0.00	0.01	0.00	0.00	0.00
Ni	0.00	0.00	0.00	0.00	0.00	0.00	0.00	0.00	0.00
Na	0.02	0.03	0.12	0.11	0.11	0.09	0.09	0.10	0.18
K	0.81	0.77	0.69	0.68	0.72	0.74	0.78	0.73	0.68
F	-0.02	-0.02	0.00	-0.01	-0.02	-0.03	-0.01	-0.03	-0.02
Cl	0.00	0.00	0.00	0.00	0.00	0.00	0.00	0.00	0.00

Abbreviations:

VBF = Venam's Bight Formation

BCF = Bobby Cove Formation

CCLT = clinopyroxene crystal-lapillil tuff

ABLT = amygdaloidal basalt lapilli tuff

IV = tetrahedral site

VI = octahedral site

Table 2.3 Averages of Electron Microprobe Analyses - Carbonates

Hole ID	PC-14-225	PC-13-204	PC-14-236	PC-12-187	PC-12-193	PC-14-225	PC-11-180	PC-11-180	PC-14-236	PC-14-232	PC-89-029
Sample ID	PC-225-002	PC-204-002	PC-236-011	PC-187-010	PC-193-003	PC-225-007	PC-180-025	PC-180-002	PC-236-023	PC-232-010	PC-29-006
Depth (m)	12.8	42.6	168.4	136	23.65	69.25	244.5	18.9	309.1	66.7	83.4
Lith	gabbro	greywacke	maroon argillite	sediments and tuffs	greywacke	BCF-ABLT	VBF-B	BCF-CCLT	quartz breccia-veins	quartz breccia-veins	quartz breccia-veins
Alteration	least altered	distal	distal	distal	proximal	proximal	proximal	proximal	proximal	proximal	proximal
Mineral	carbonate	carbonate	carbonate	carbonate	carbonate	carbonate	carbonate	carbonate	carbonate	carbonate	carbonate
Analytical Spots	*n=5*	*n=7*	*n=3*	*n=5*	*n=5*	*n=9*	*n=8*	*n=10*	*n=10*	*n=7*	*n=11*
Major element (wt %)											
FeO	0.15	0.31	0.19	0.62	4.55	9.35	0.63	6.69	9.13	0.56	0.57
MnO	0.34	0.72	1.55	1.44	1.71	0.60	0.67	0.57	0.58	0.65	0.56
MgO	0.08	0.18	0.01	0.31	4.50	12.97	0.28	15.69	2.17	0.19	0.06
CaO	54.61	53.40	52.03	52.90	41.36	29.73	53.65	29.74	43.31	53.31	54.31
SrO	0.06	0.15	0.08	0.53	0.15	0.05	0.07	0.05	0.13	0.14	0.16
BaO	-0.01	0.01	0.02	0.00	0.00	-0.01	-0.02	-0.01	0.00	0.02	0.00
Total	55.23	54.79	53.89	55.79	52.27	52.68	55.28	52.74	55.33	54.87	55.67
Atom per formula unit											
Fe	0.01	0.01	0.01	0.03	0.24	0.39	0.03	0.27	0.43	0.02	0.02
Mn	0.01	0.03	0.07	0.06	0.07	0.03	0.03	0.02	0.03	0.03	0.02
Mg	0.01	0.01	0.00	0.02	0.42	0.97	0.02	1.14	0.18	0.01	0.00
Ca	2.97	2.94	2.92	2.87	2.27	1.61	2.92	1.56	2.36	2.93	2.94
Sr	0.00	0.00	0.00	0.02	0.00	0.00	0.00	0.00	0.00	0.00	0.00
Ba	0.00	0.00	0.00	0.00	0.00	0.00	0.00	0.00	0.00	0.00	0.00

Abbreviations:

VBF = Venam's Bight Formation

BCF = Bobby Cove Formation

CCLT = clinopyroxene crystal-lapillil tuff

ABLT = amygdaloidal basalt lapilli tuff

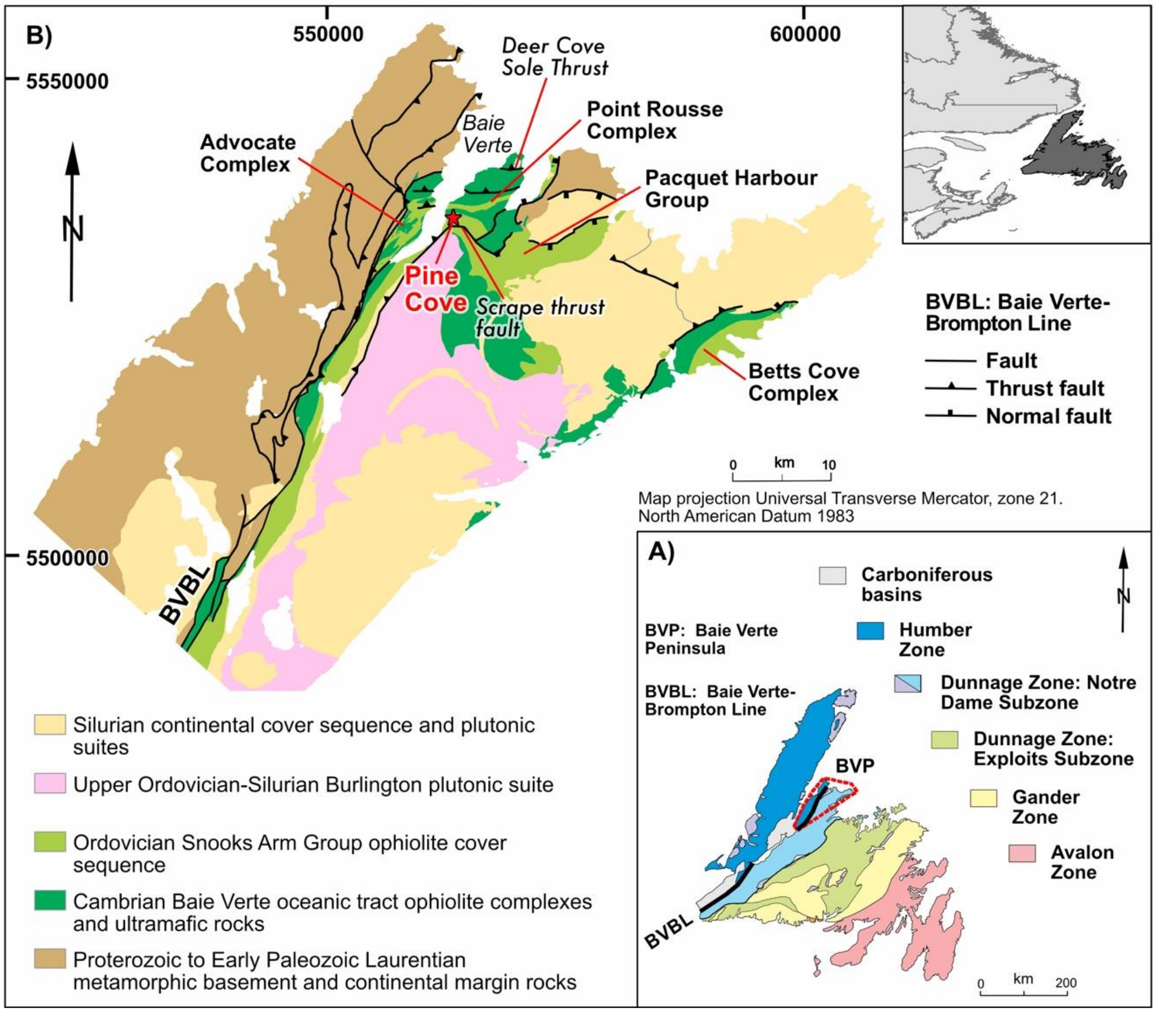

Figure 2.1. A) Simplified geologic map of Newfoundland. Modified from Skulksi et al. (2017). B) Geologic map of the Baie Verte Peninsula. Modified from Skulksi et al. (2017).

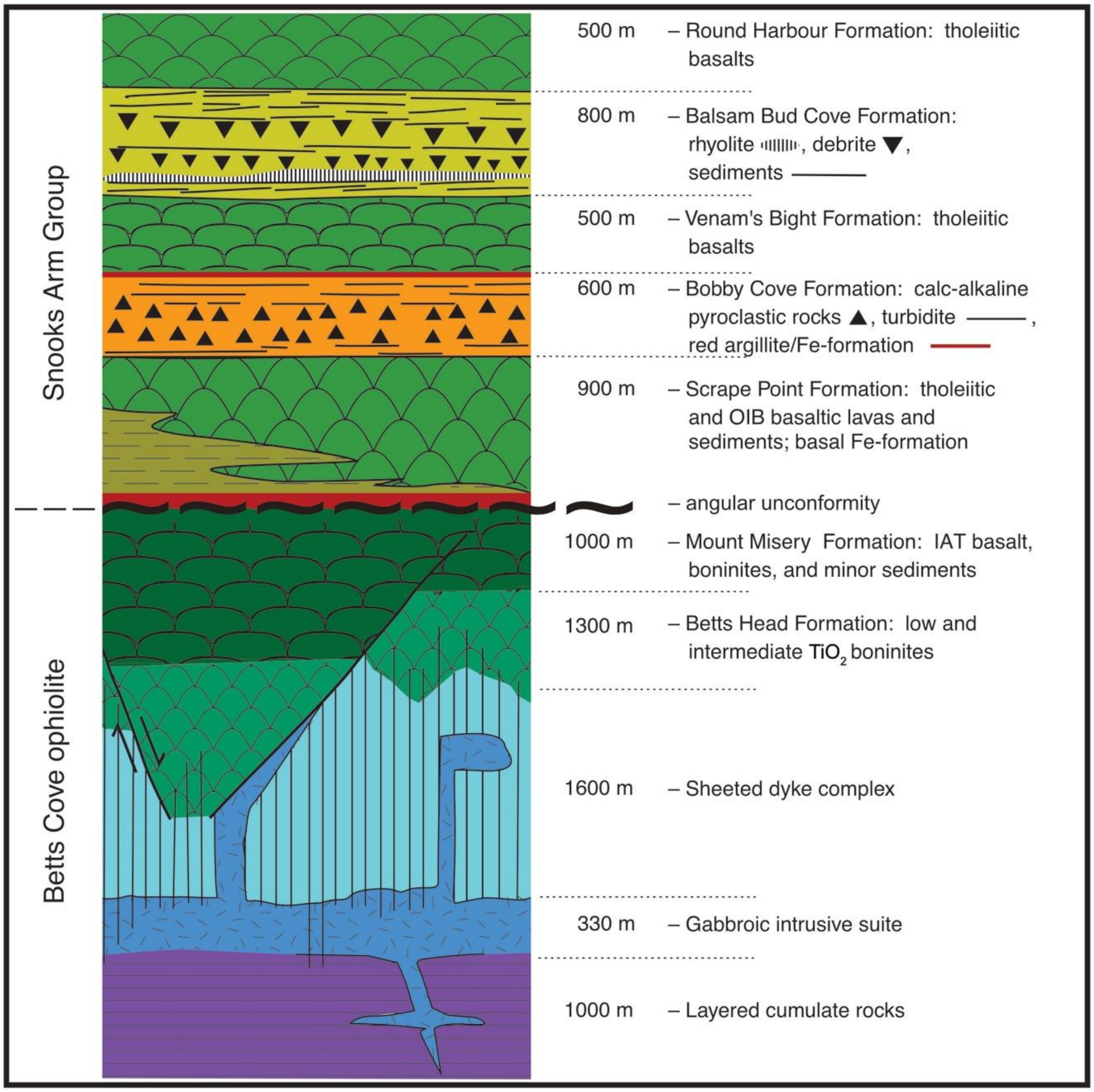

Figure 2.2. Schematic stratigraphic column through the Betts Cove ophiolite and Snooks Arm Group. IAT = island arc tholeiite; OIB = ocean island basalt. Maximum thicknesses are listed. Modified from Bédard et al. (2000) and Skulski et al. (2009, 2010).

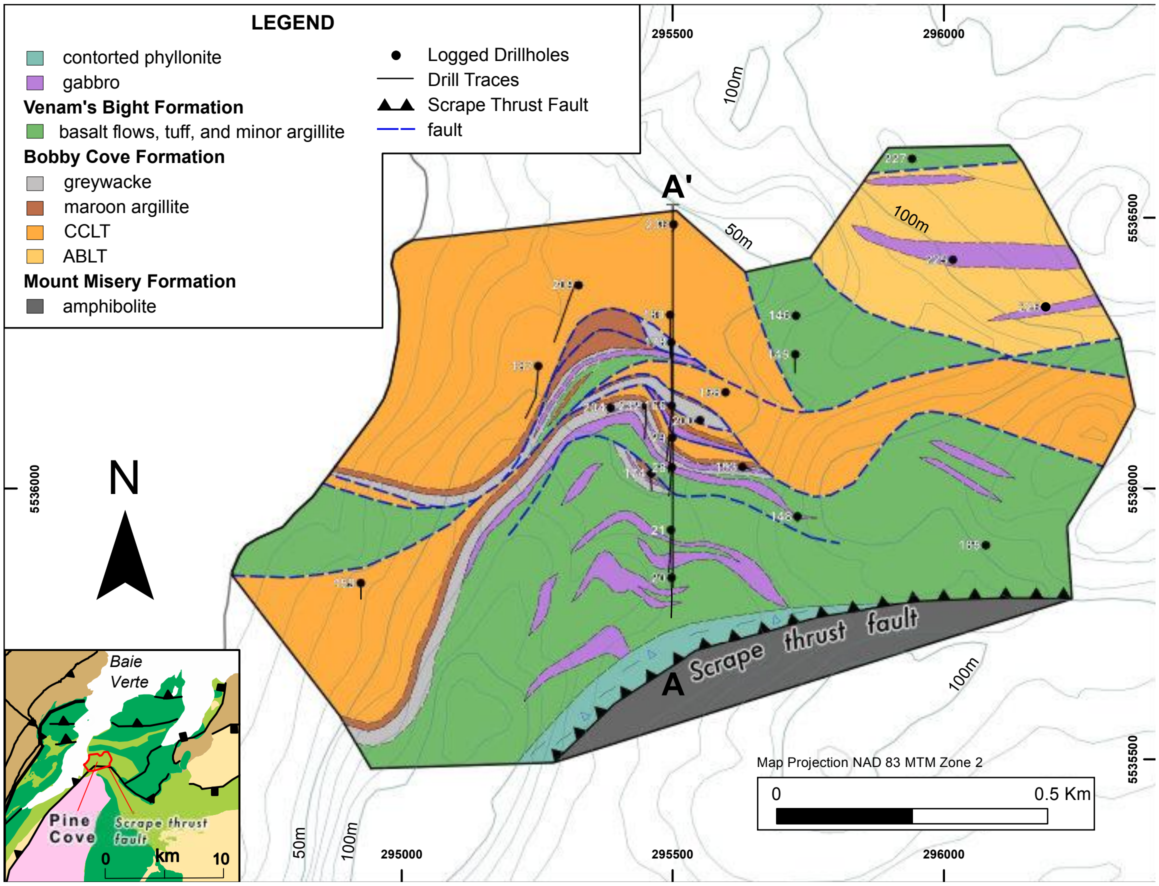

Figure 2.3. Pine Cove deposit geology plan map with mineralization lenses projected vertically to pre-mine surface and location of cross section in Figure 2.4. Drill holes shown on map were selected for logging and lithogeochemical analysis. Modified from unpublished mapping by Anaconda Mining. Extent of geology map shown with red outline in inset figure at bottom left. Legend for inset on Figure 1.

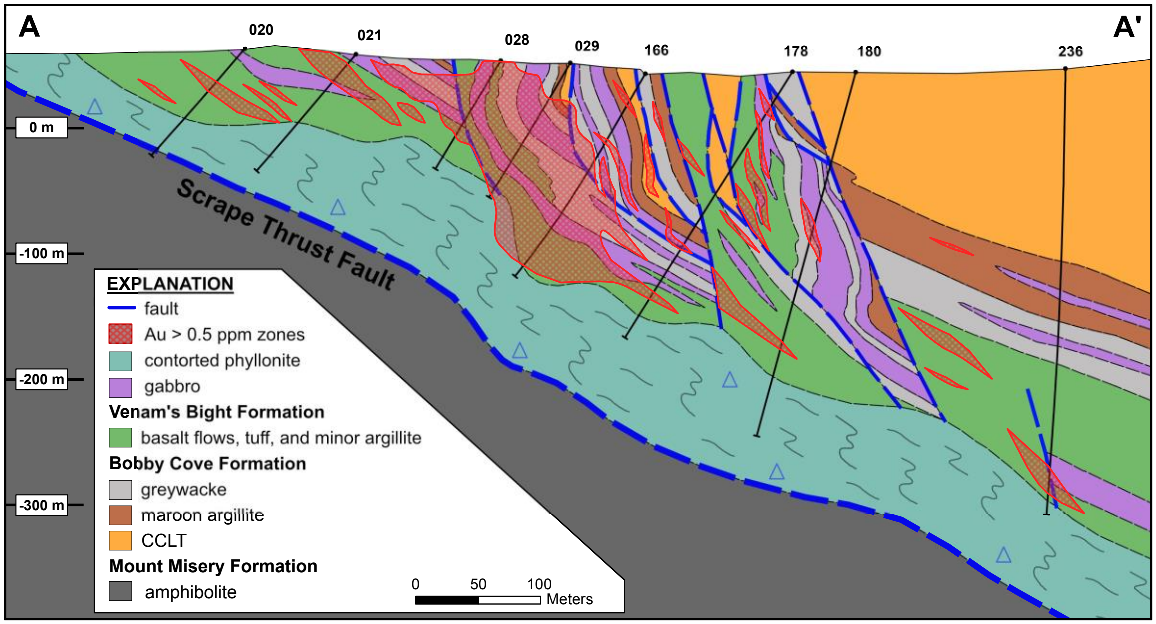

Figure 2.4. North-South geologic cross section along A-A'.

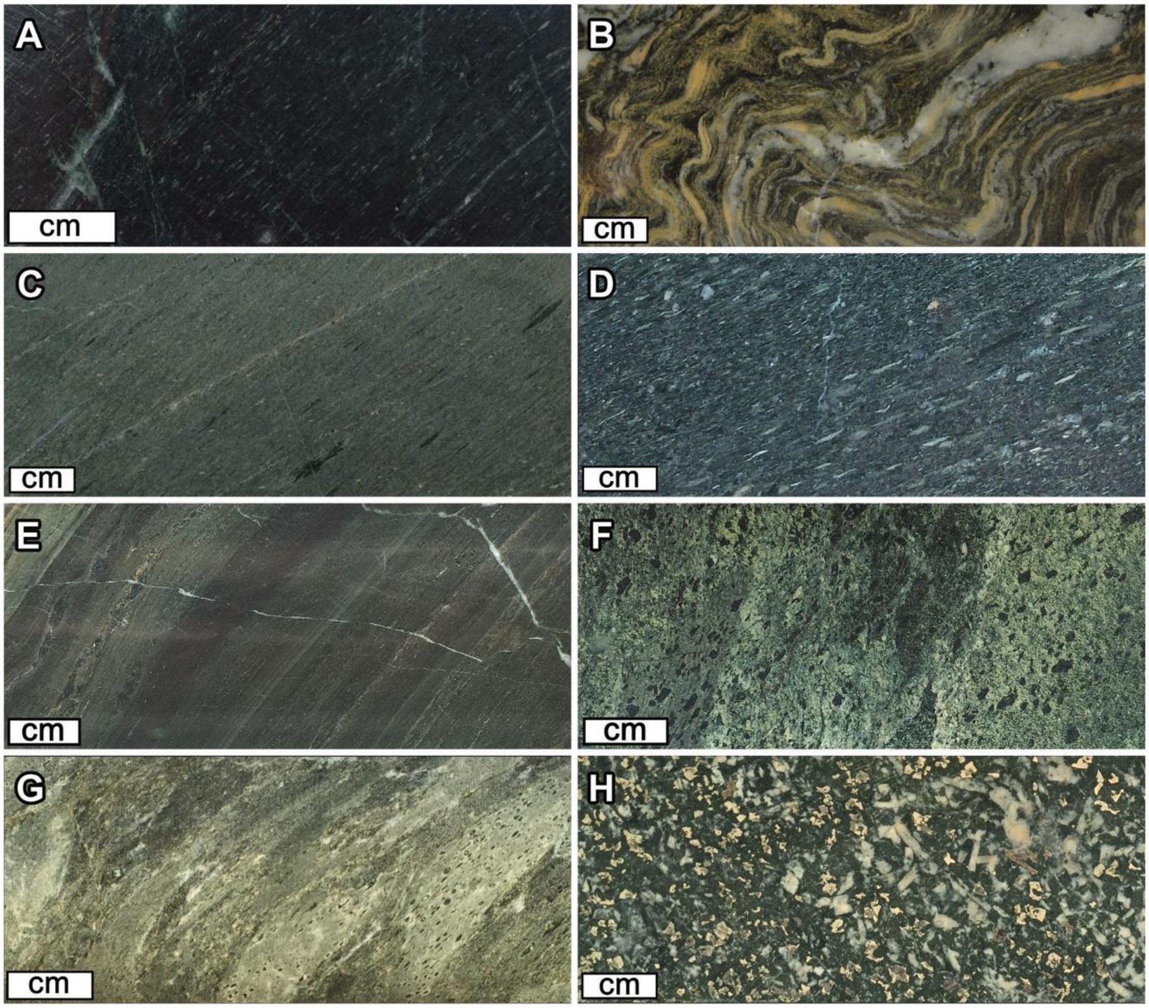

Figure 2.5. Lithologies of the Pine Cove deposit. A) Amphibolite in the footwall of the Scrape Thrust fault. PC-89-020 @ 109.5m. B) Contorted phyllonite in hanging wall of Scrape Thrust fault. PC-89-021 @ 75.5m. C) High Fe-Ti basalt of Venam's Bight Formation. PC-13-204 @ 75.5m. D) Greywacke with mm-scale lithic fragments. PC-13-204 @ 42.6m. E) Maroon-coloured hematitic, siliceous argillite. PC-12-187 @ 63.8m. F) Clinopyroxene crystal-lapilli tuff of Bobby Cove Formation (BCF-CCLT). PC-13-200 @ 24.5m. G) Lapilli tuff of Bobby Cove Formation containing amygdaloidal basaltic clasts (BCF-ABLT). PC-14-226 @ 50.5m. H) High Fe-Ti gabbro. PC-14-226 @ 7.7m.

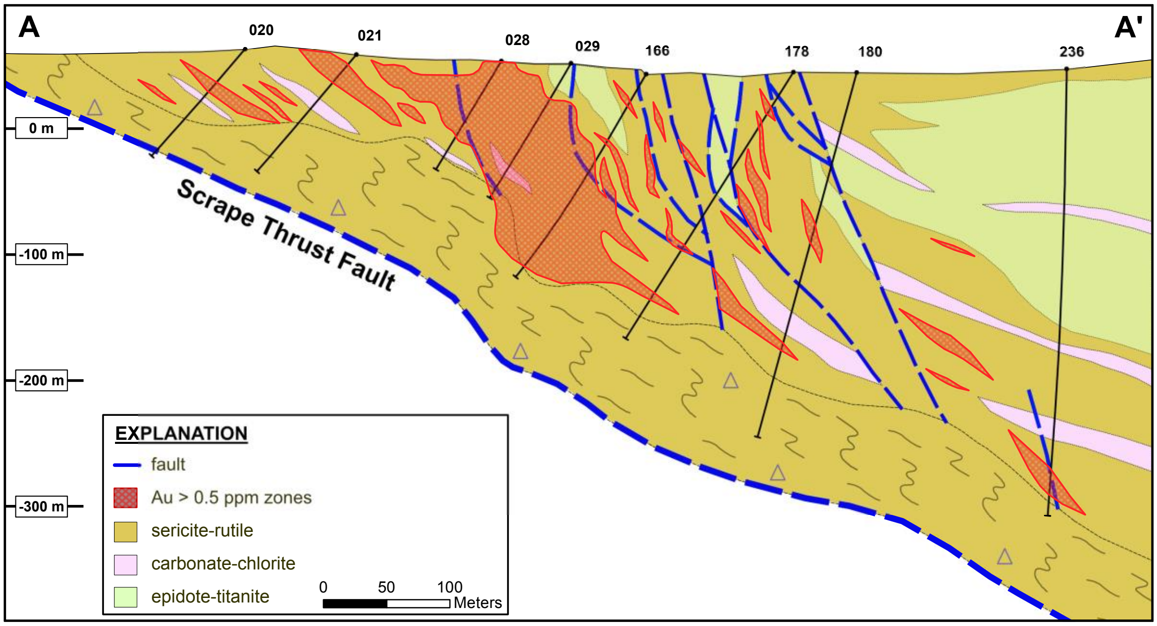

Figure 2.6. Alteration cross section along A-A’.

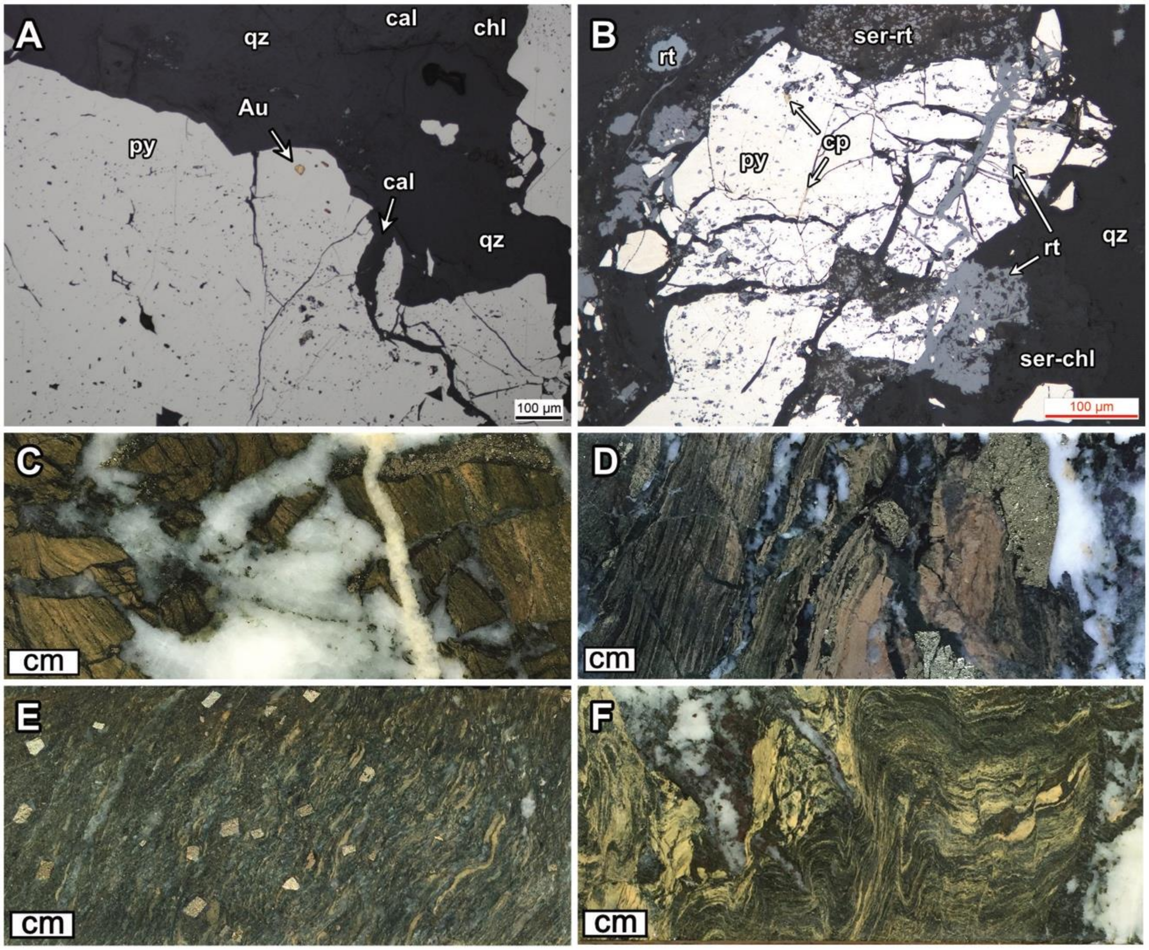

Figure 2.7. Gold mineralization at Pine Cove. A) Reflected light microphotograph of gold inclusion in pyrite grain that is fractured by quartz and calcite veinlets. PC-89-029 @ 83.5m. B) Reflected light microphotograph of pyrite with rutile-quartz-chlorite filled fractures and abundant inclusions of rutile and quartz. Chalcopyrite occurs as both inclusions in pyrite and fracture filling. PC-14-236 @ 309.1m. C) Quartz veins showing brittle brecciation and tan sericite-chlorite-pyrite alteration selvages. Vein is cut by late calcite veinlet. PC-14-232 @ 67.9m. D) Quartz-chlorite veins with sericite-chlorite-calcite-rutile-pyrite-pink albite alteration selvage. PC-14-236 @ 308.8m. E) Disseminated pyrite in sericite-chlorite altered greywacke. PC-13-200 @ 75m. F) Quartz-chlorite-calcite breccia veins with chlorite-tan sericite alteration haloes cut folded D_2 foliation. Some veins are sub-parallel to axial planes of folds. PC-13-204 @ 118.3m.

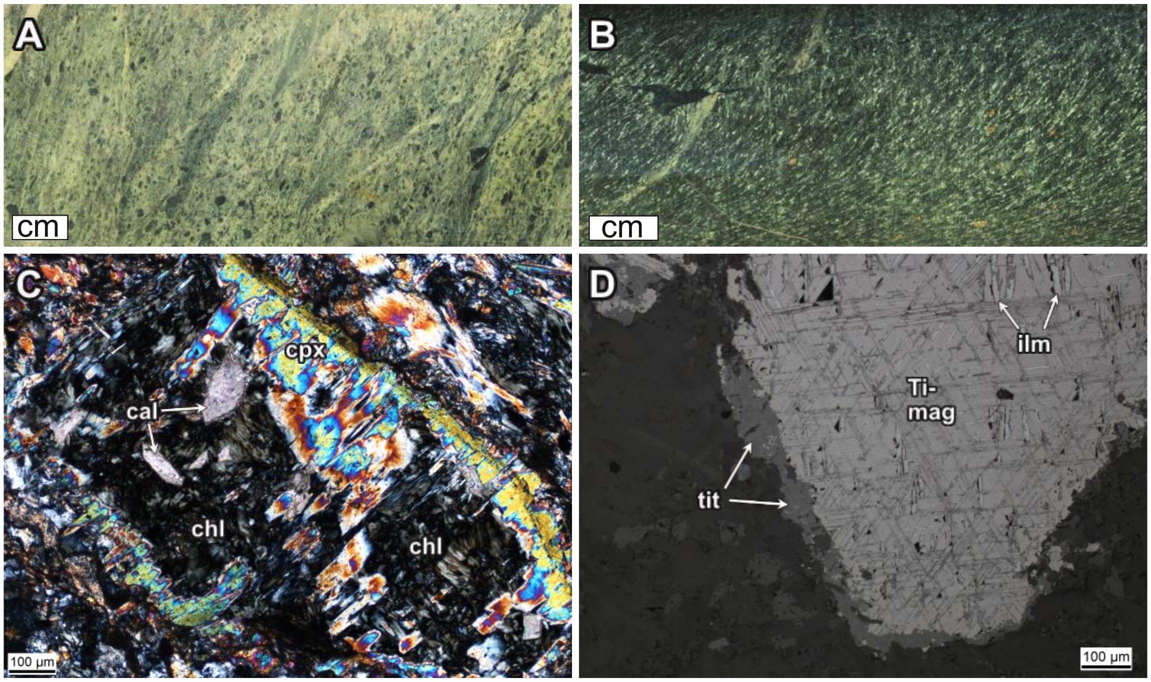

Figure 2.8. Distal mineral assemblage at Pine Cove. A) Epidote-chlorite altered lapilli tuff of the Bobby Cove Formation. PC-11-180 @ 67.5m. B) Chlorite-titanite-epidote-pyrite altered gabbro. PC-13-204 @ 48.2m. C) Cross-polarized light microphotograph of Bobby Cove Formation clinopyroxene-phyric tuff altered to chlorite and calcite. PC-14-236 @ 91.1m. D) Reflected light microphotograph of titanite rimming titaniferous magnetite with ilmenite exsolution lamellae in gabbro. PC-14-225 @ 14.8m.

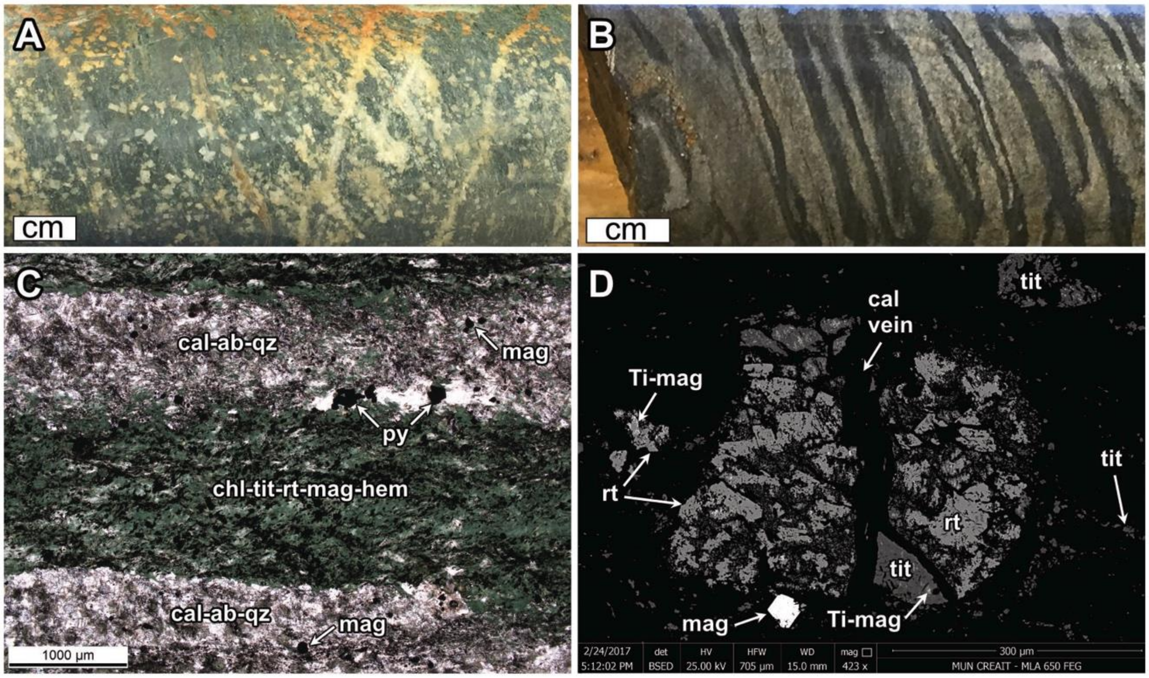

Figure 2.9. Intermediate mineral assemblage at Pine Cove. A) Fe-dolomite porphyroblasts and veinlets in fine-grained tuffaceous unit of the Bobby Cove Formation. PC-11-180 @ 19m. B) Banding of carbonate-quartz-albite and chlorite-leucoxene-magnetite parallel to foliation in basalt(?) of the Venam's Bight Formation. PC-14-236 @ 279.5m. C) Cross-polarized light microphotograph of alternating banding of calcite-albite-quartz and chlorite±titanite±rutile±magnetite in basalt(?) of the Venam's Bight Formation. PC-14-236 @ 279.4m. D) Scanning electron microscope back scatter electron (SEM-BSE) image of detrital Ti-magnetite grain in greywacke that is cut by a calcite veinlet. Ti-magnetite in sample is predominantly altered to titanite, but titanite is converted to rutile proximal to calcite veinlet. PC-13-204 @ 42.6m.

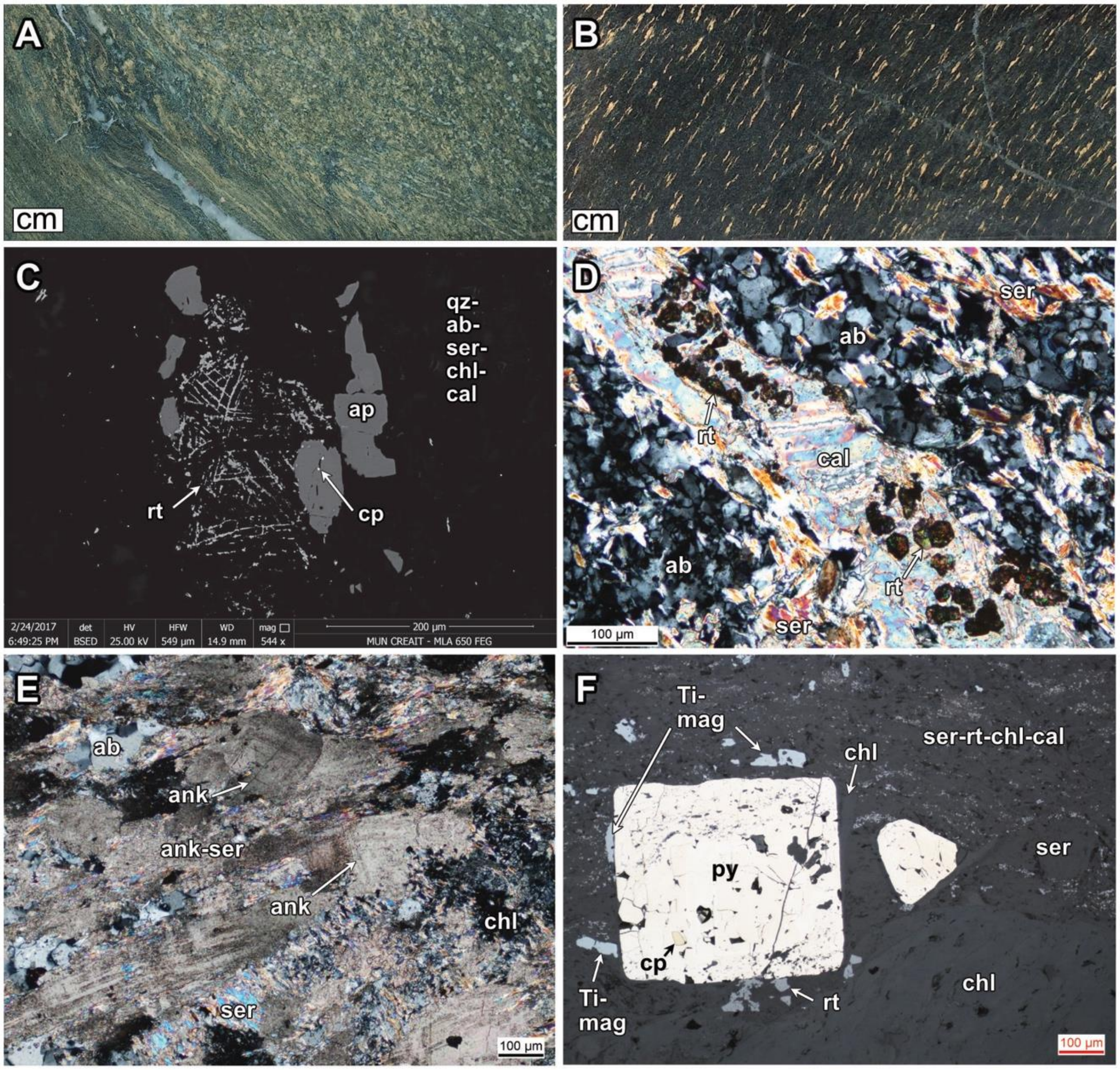

Figure 2.10. Proximal mineral assemblage at Pine Cove. A) Tan sericite-chlorite-carbonate-rutile altered tuff of the Venam's Bight Formation. PC-13-204 @ 134.4m. B) Rutile-chlorite-sericite-carbonate altered gabbro. PC-13-198 @ 134.1m. C) SEM-BSE image of skeletal rutile after Ti-magnetite. PC-05-166 @ 70.9m. D) Cross-polarized light microphotograph of calcite-rutile veinlet. PC-14-232 @ 66.7m. E) Cross-polarized light microphotograph showing ankerite porphyroblasts that are overprinted by finer-grained ankerite-sericite-chlorite alteration. PC-14-225 @ 69.3m. F) Reflected light microphotograph of pyrite porphyroblast with abundant calcite-rutile inclusions and chlorite pressure shadow. PC-14-236 @ 309.1m.

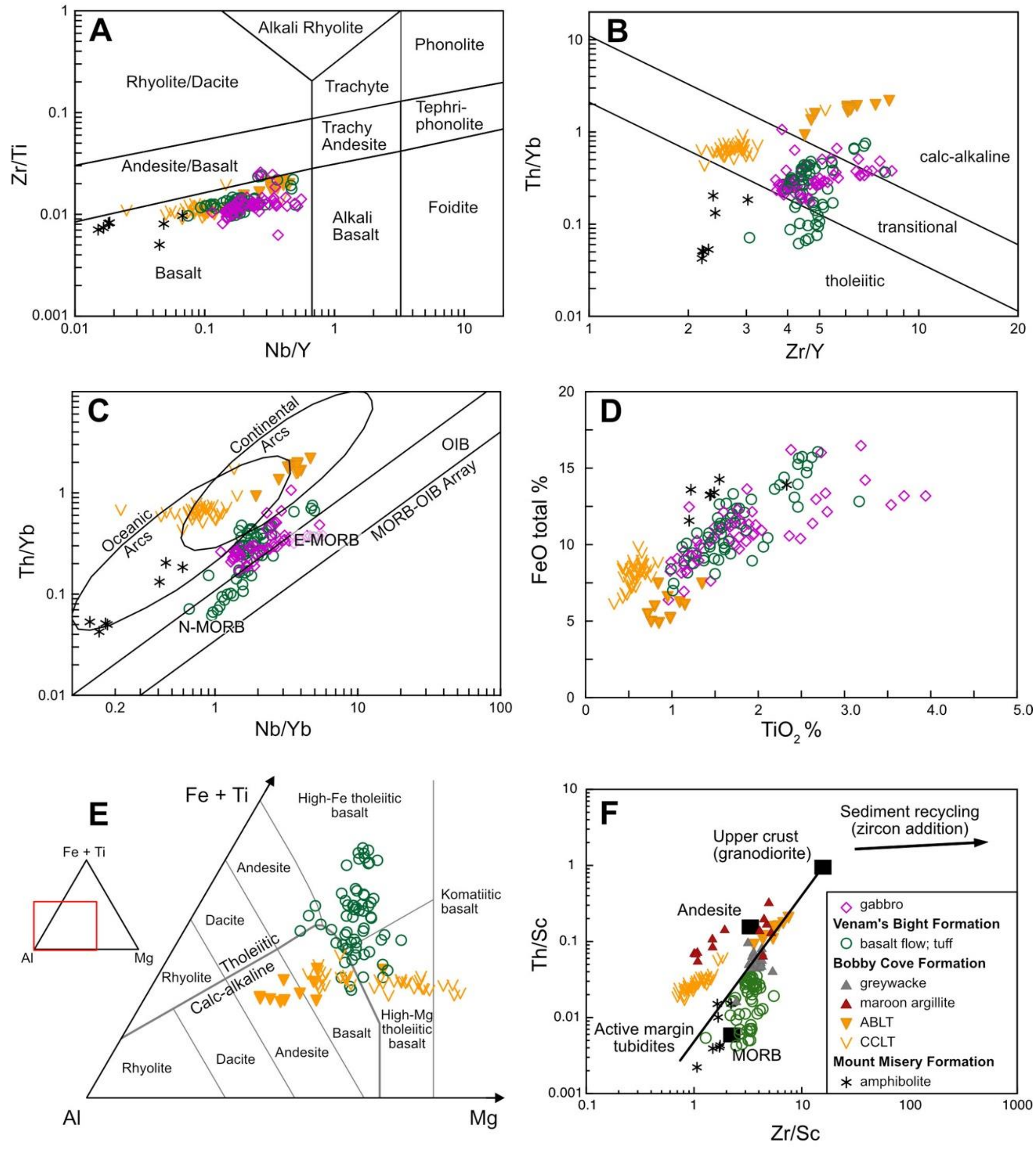

Figure 2.11. A) Winchester and Floyd (1977) Zr/Ti-Nb/Y discrimination diagram for rock classification (modified from Pearce, 1996). B) Th/Yb-Zr/Y discrimination diagram of Ross and Bédard (2009). C) Th/Yb-Nb/Yb discrimination diagram of Pearce (2014). D) FeO-TiO_2 plot showing the Fe-Ti enrichment in gabbros and Venam's Bight basalts relative to Bobby Cove Formation volcaniclastic rocks. E) Cation plot of Jensen (1976) showing tholeiitic trend of Venam’s Bight Formation basalts and calc-alkaline trend of Bobby Cove Formation volcaniclastic rocks. F) Th/Sc-Zr/Sc diagram for modern turbidites from active and passive margins illustrating the lithogeochemical similarity of the maroon argillite with Bobby Cove Formation rocks (modified from McLennan et al., 2003). Both ratios increase for turbidites from active margins, whereas Zr/Sc ratios increase relative to Th/Sc ratios in more mature sediments due to sorting and concentration of the heavy mineral zircon.

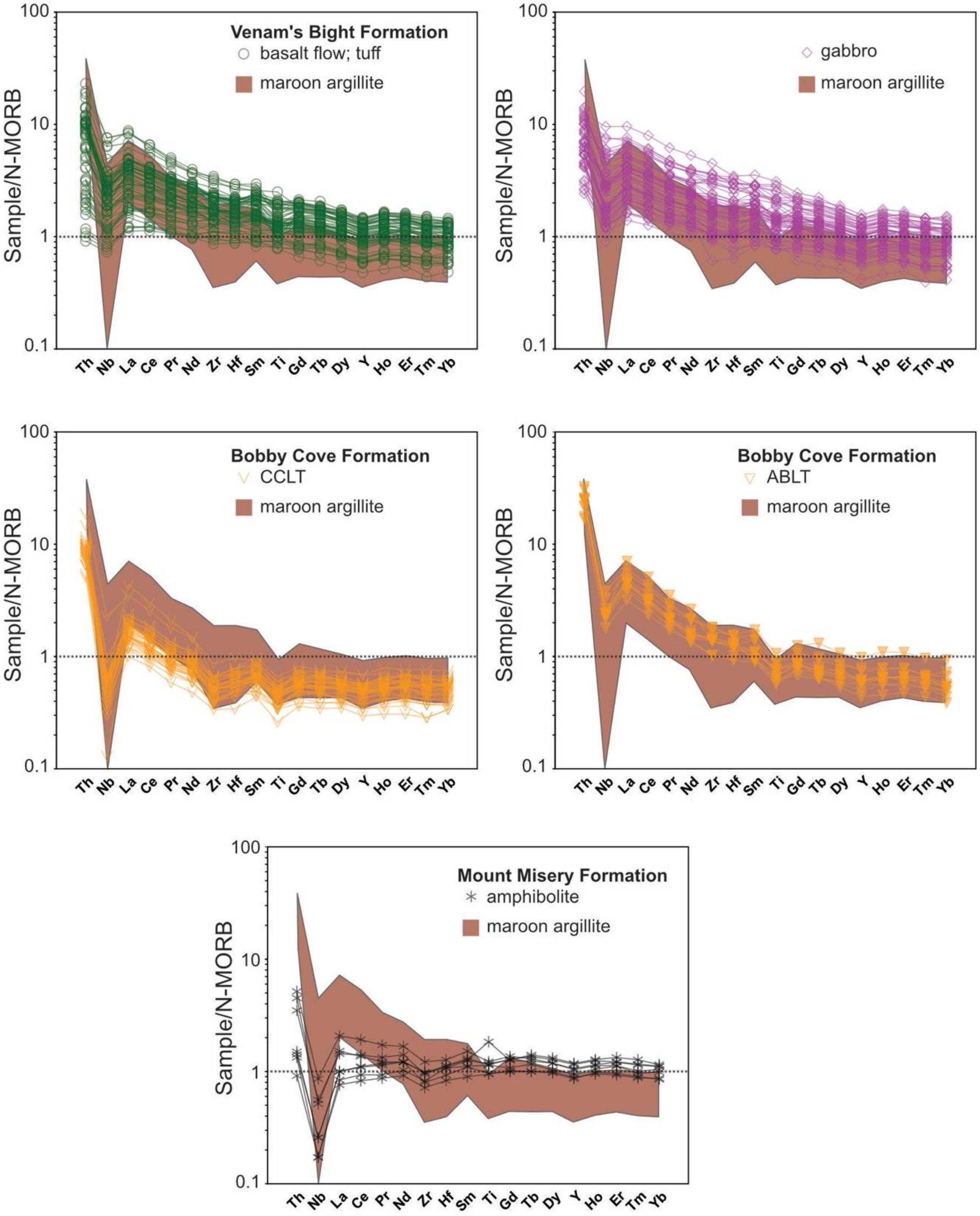

Figure 2.12. REE + HFSE plots of Pine Cove lithologies normalized to N-MORB of Sun and McDonough (1989) after Pearce (2014). Shaded areas represent values from the maroon argillite, which predominantly overlap with Bobby Cove Formation rocks.

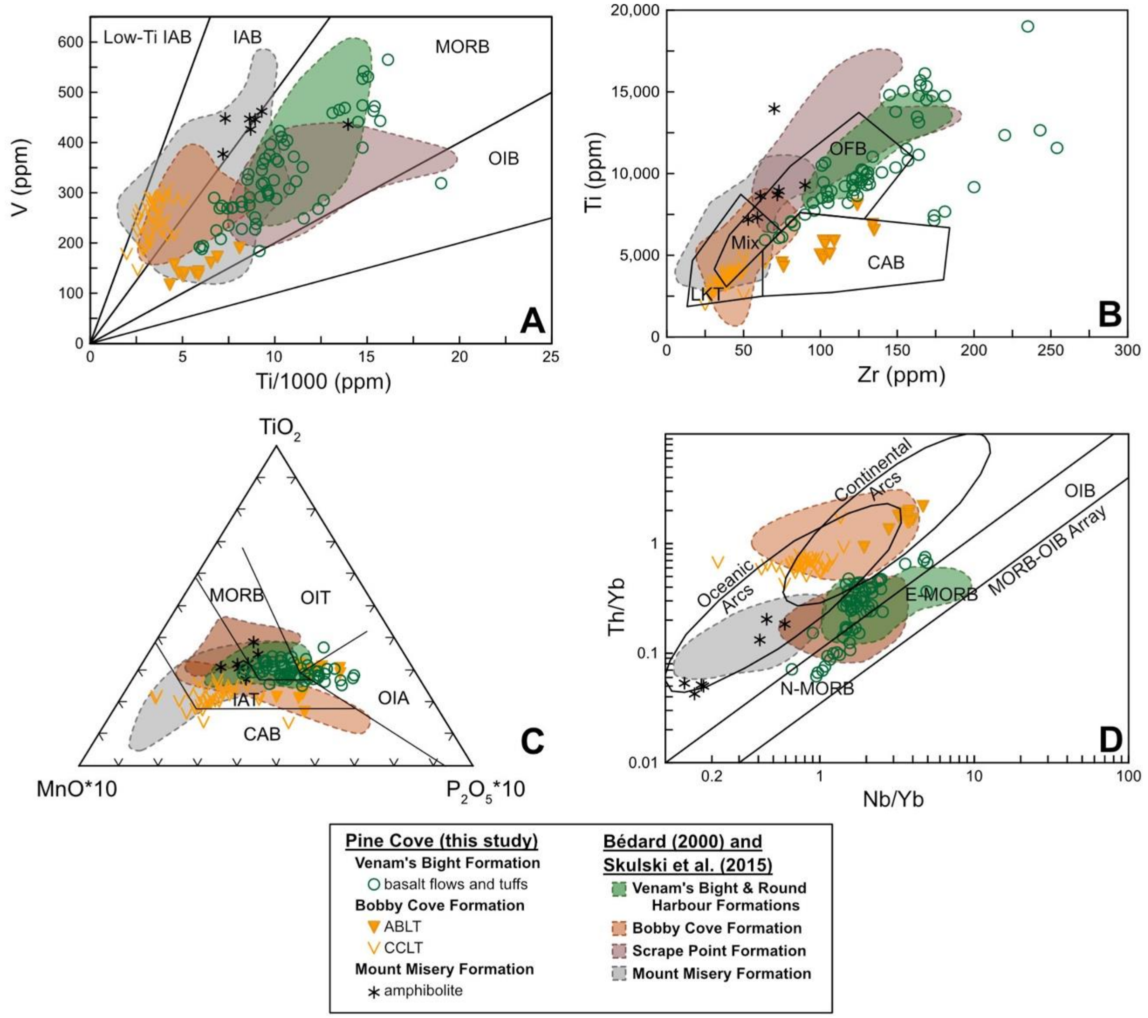

Figure 2.13. Comparison plots to geochemical data from the Snooks Arm Group. A) Ti-V tectonic discrimination diagram of Shervais (1982). IAB = island arc basalt, MORB = mid-ocean ridge basalt, OIB = ocean island basalt. Fields for comparison to the Snooks Arm Group at the Betts Cove Complex are from Bédard (2000). B) Ti-Zr tectonic discrimination diagram of Pearce and Cann (1973). LKT = low-K tholeiites, OFB = ocean floor basalts, CAB = calc-alkaline basalts. Fields for comparison to the Snooks Arm Group at the Betts Cove Complex are from Bédard (2000). C) MnO*10-TiO$_2$-P$_2$O$_5$*10 tectonic discrimination diagram of Mullen (1983). CAB = calc-alkaline basalt. IAT = island-arc tholeiite, MORB = mid-ocean ridge basalt, OIA = ocean-island andesite, OIT = ocean-island tholeiite. Fields for comparison to the Snooks Arm Group at the Betts Cove Complex are from Bédard (2000). D) Th/Yb-Nb/Yb discrimination diagram of Pearce (2014). Fields for comparison to the Snooks Arm Group are from Skulski et al. (2015).

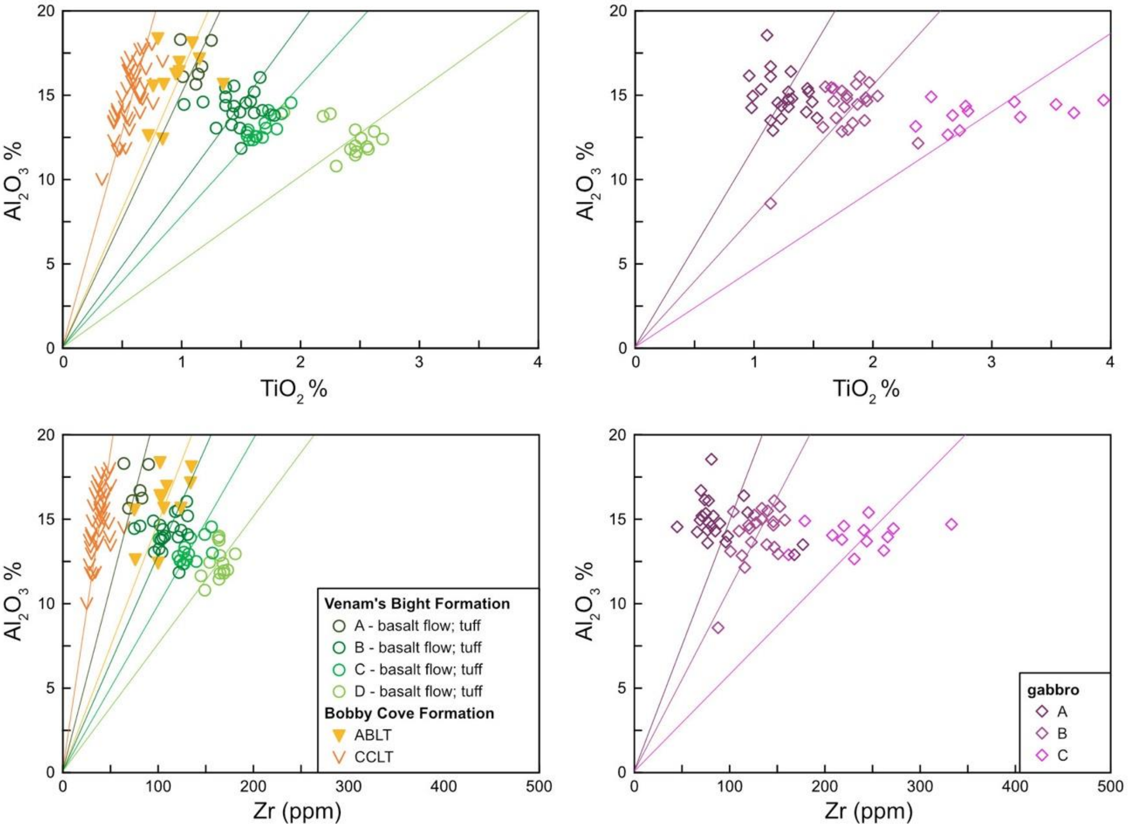

Figure 2.14. Selected variation diagrams showing the fractionation trends of the gabbros and Venam's Bight Formation volcanic units. Subdivision designations (A, B, etc.) for mass balances calculations are based on geochemical affinities, and are not intended to convey any timing or stratigraphic relationship. Solid diagonal lines define the trends where samples from a single precursor ideally plot if the considered elements are immobile.

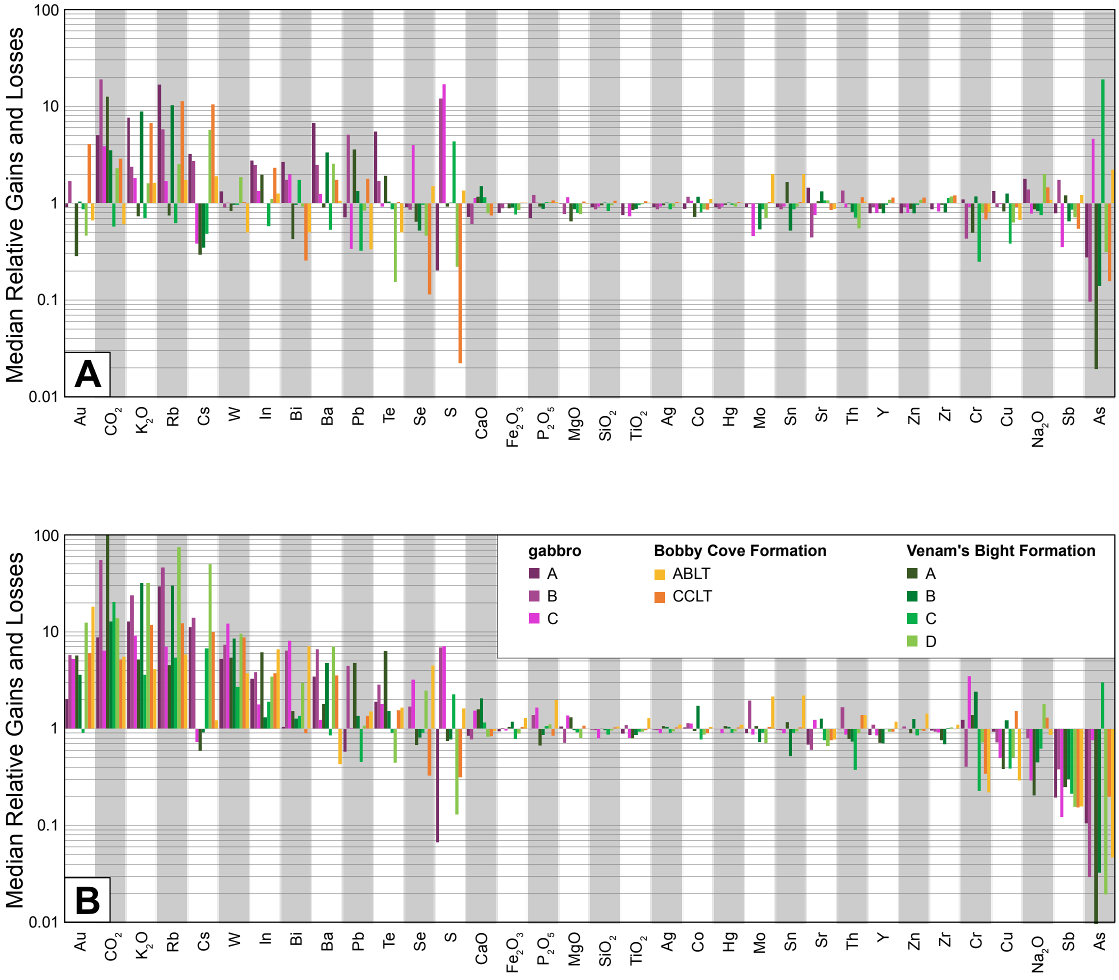

Figure 2.15. A) Median relative gains and losses, calculated by the method of MacLean and Barrett (1990), of select components in distal (epidote-titanite-chlorite±carbonate) altered units. B) Median relative gains and losses in proximal (sericite-rutile-chlorite-carbonate) altered units. The least altered composition has values equal to 1; values below 1 indicate depletion and values above 1 indicate enrichment. Subdivision designations (A, B, etc.) are based on geochemical affinities, and are not intended to convey any timing or stratigraphic relationship.

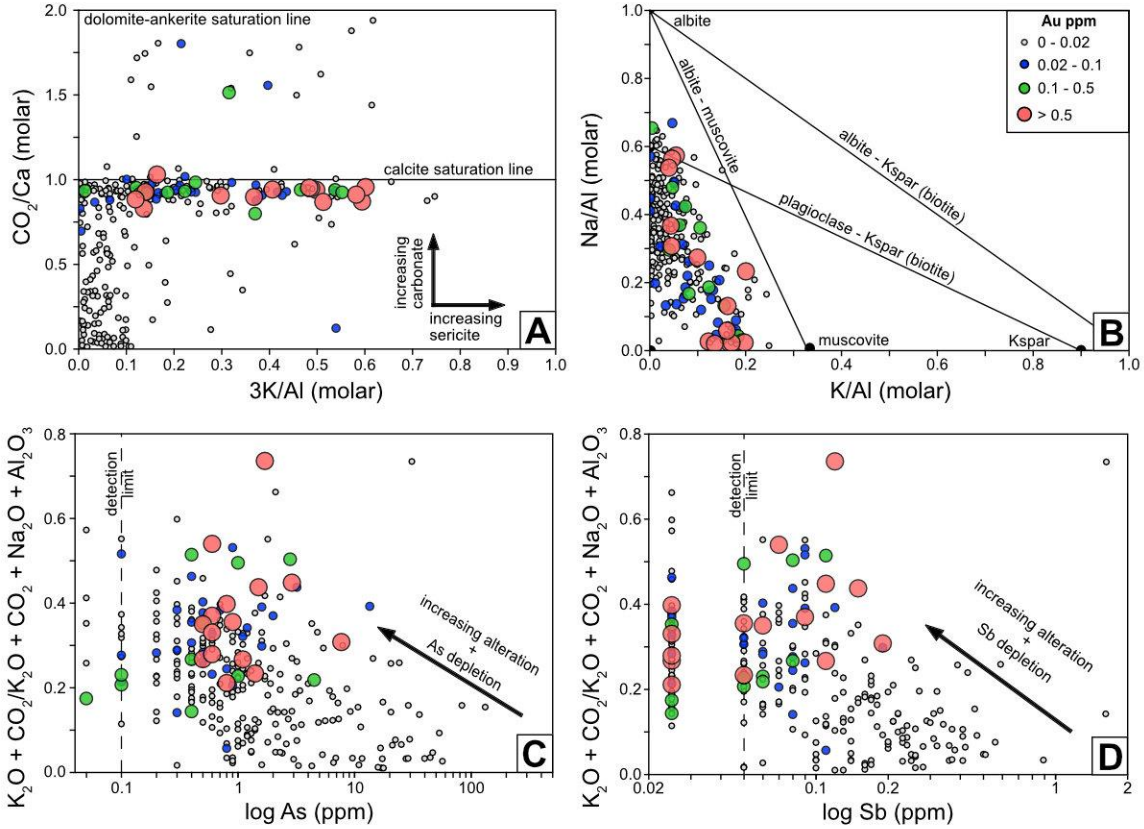

Figure 2.16. A) Carbonate alteration index versus sericite alteration index (e.g. Eilu et al., 1998). The line CO_2/Ca = 1 represents all available Ca has been used to form calcite. Samples that plot above the line CO_2/Ca = 1 contain Fe-, Mg-, and/or Mn-bearing carbonates, such as ankerite. B) Na/Al versus K/Al molar ration plot showing relationship between sericite, albite, and Au mineralization. Modified from Davis and Whitehead (2006). C) Alkali + carbonate alteration index (e.g. Bierlein et al. 2000) versus As variation diagram, illustrating depletion of As with increasing alteration and Au mineralization. D) Alkali + carbonate alteration index versus Sb variation diagram.

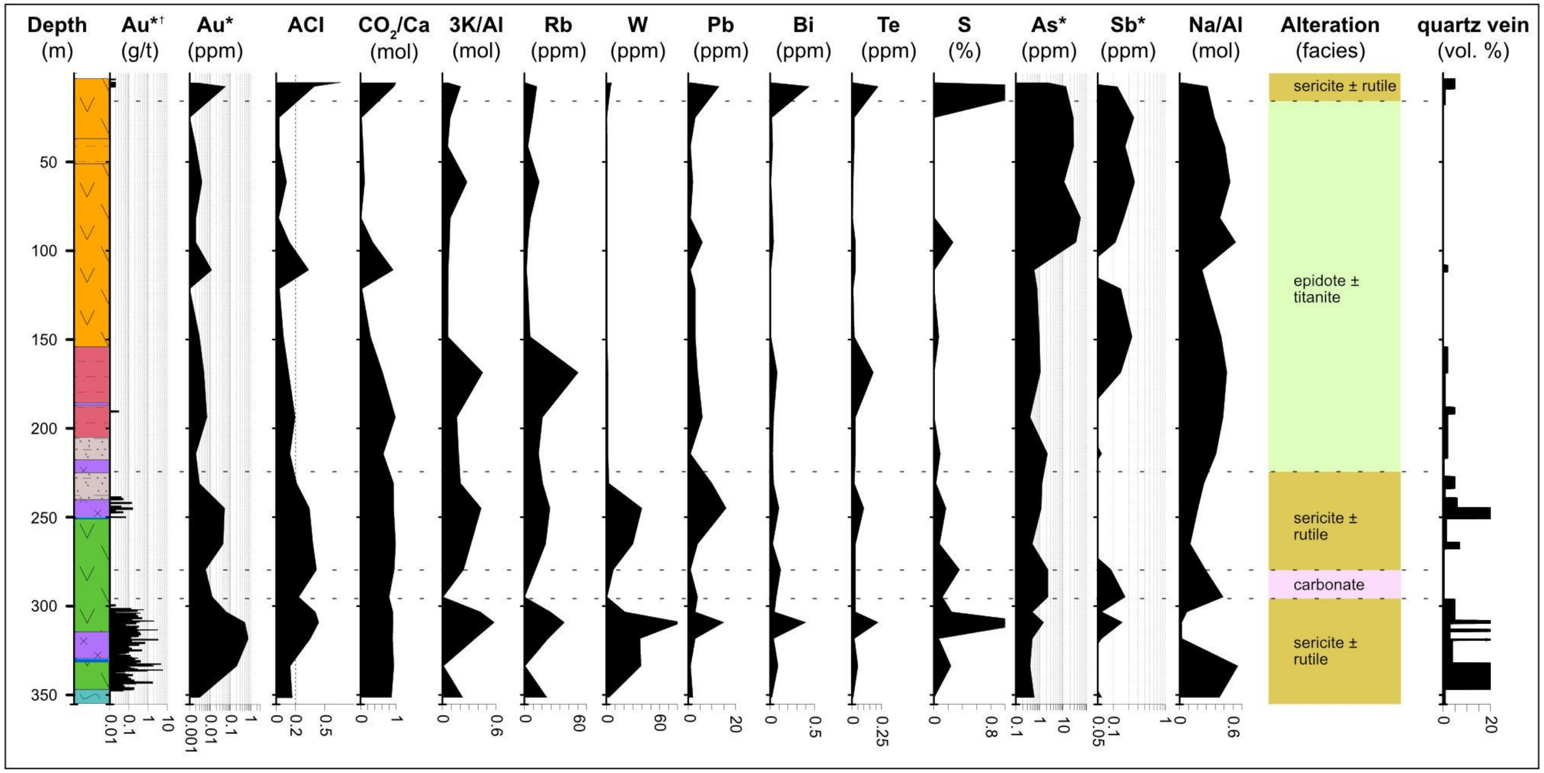

Figure 2.17. Strip log of representative drill hole, PC-14-236, showing key alteration components. ACI = alkali-carbonate alteration index [$K_2O + CO_2/K_2O + CO_2 + Na_2O + Al_2O_3$] of Bierlein et al., (2000). * denotes log scale; † denotes Anaconda Mining Inc. assay data. Lithology legend is same as Figures 3 and 5.

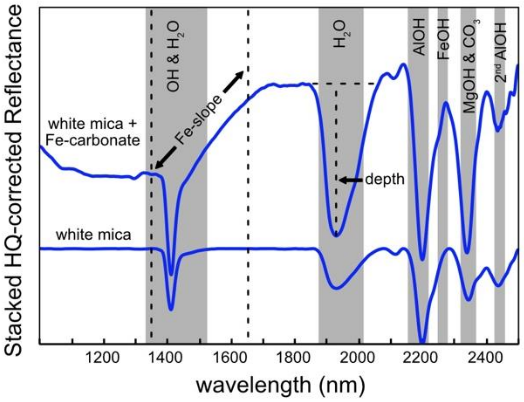

Figure 2.18. Examples of hull quotient-corrected spectra of white mica (PC-14-236 @ 308.8m) and mixed white mica-ferroan carbonate (PC-14-225 @ 69.3m). Major absorption bands in the SWIR spectrum are highlighted in grey. The presence of Fe-bearing carbonate minerals produces a down-warping of the spectra hull between 1650 and 1350 nm (AusSpec International, 2008). Modified from Herrmann et al. (2001).

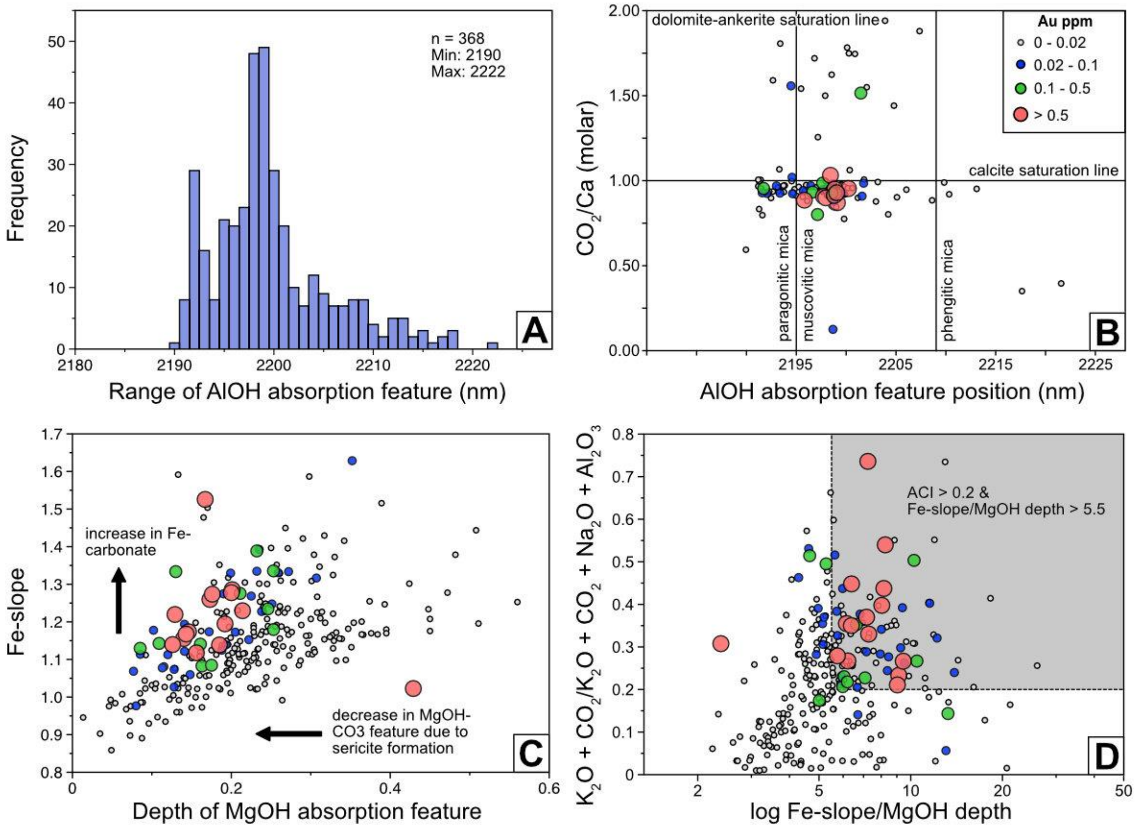

Figure 2.19. Short wave infrared spectroscopy results. A) Histogram of AlOH absorption feature wavelengths present at Pine Cove. B) Plot of molar CO_2/Ca versus the position of the AlOH absorption feature. C) Plot of Fe^{2+} slope versus the MgOH (2335 nm) absorption feature depth. D) Plot of $K_2O + CO_2$ / $K_2O + CO_2 + Na_2O + Al_2O_3$ alteration index versus Fe^{2+} slope/2335 (MgOH) depth.

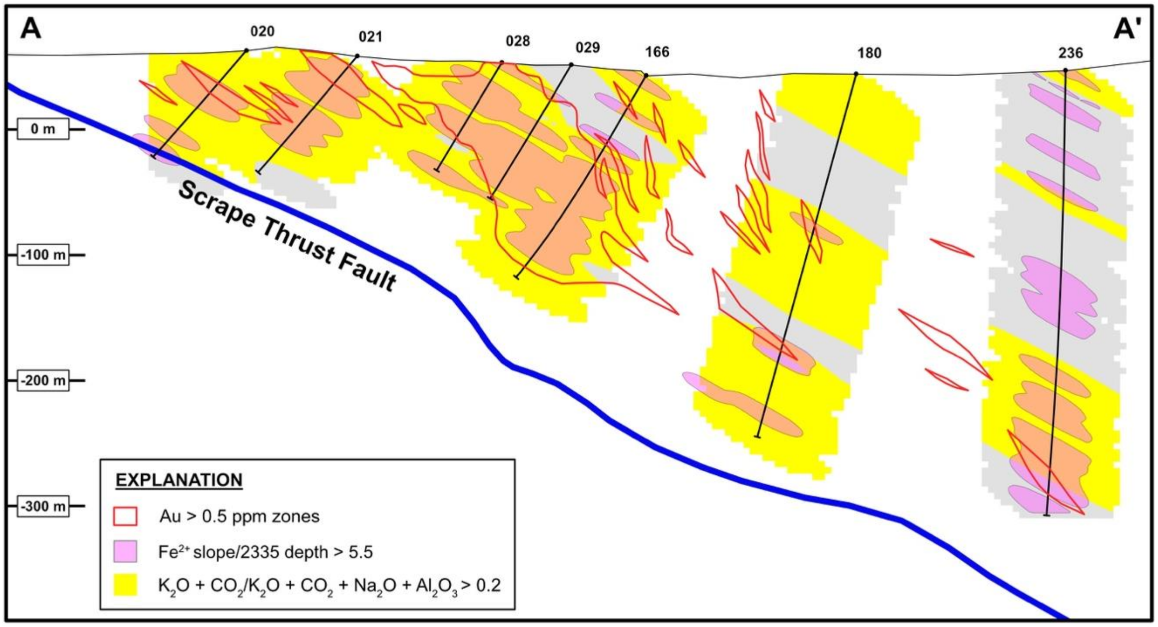

Figure 2.20. Cross section showing kriging interpolation of $K_2O + CO_2 / K_2O + CO_2 + Na_2O + Al_2O_3$ alteration index and Fe^{2+} slope/MgOH depth.

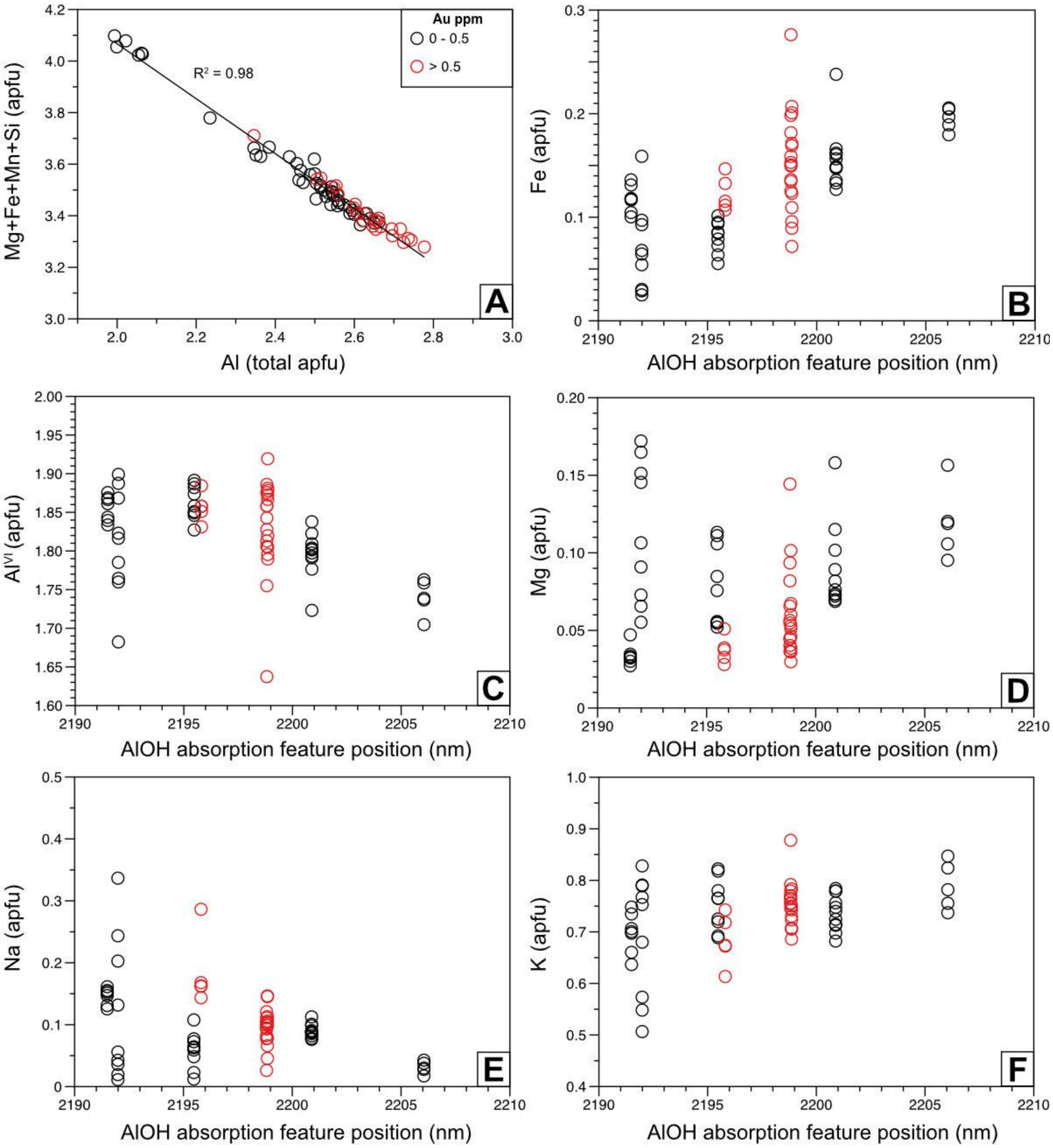

Figure 2.21. Electron microprobe analysis and SWIR spectroscopy of white micas from Pine Cove.

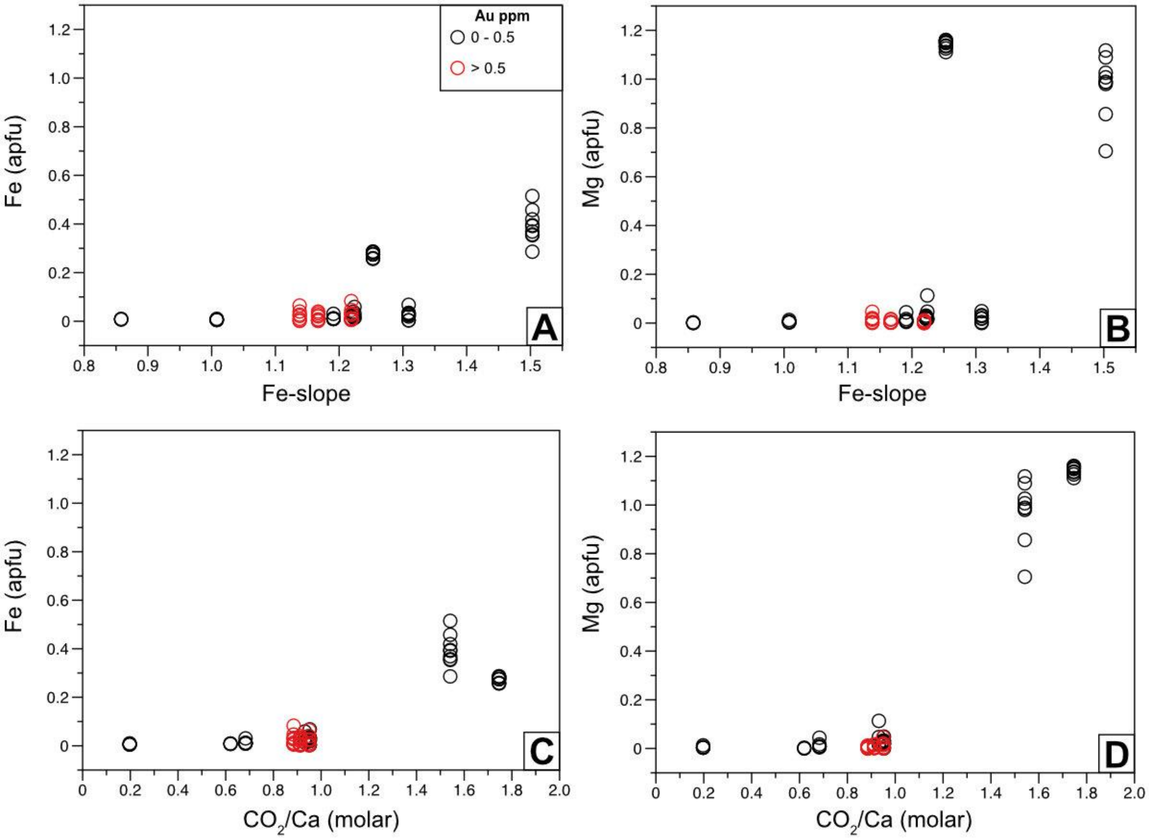

Figure 2.22. Electron microprobe analysis and SWIR spectroscopy of carbonate minerals from Pine Cove.

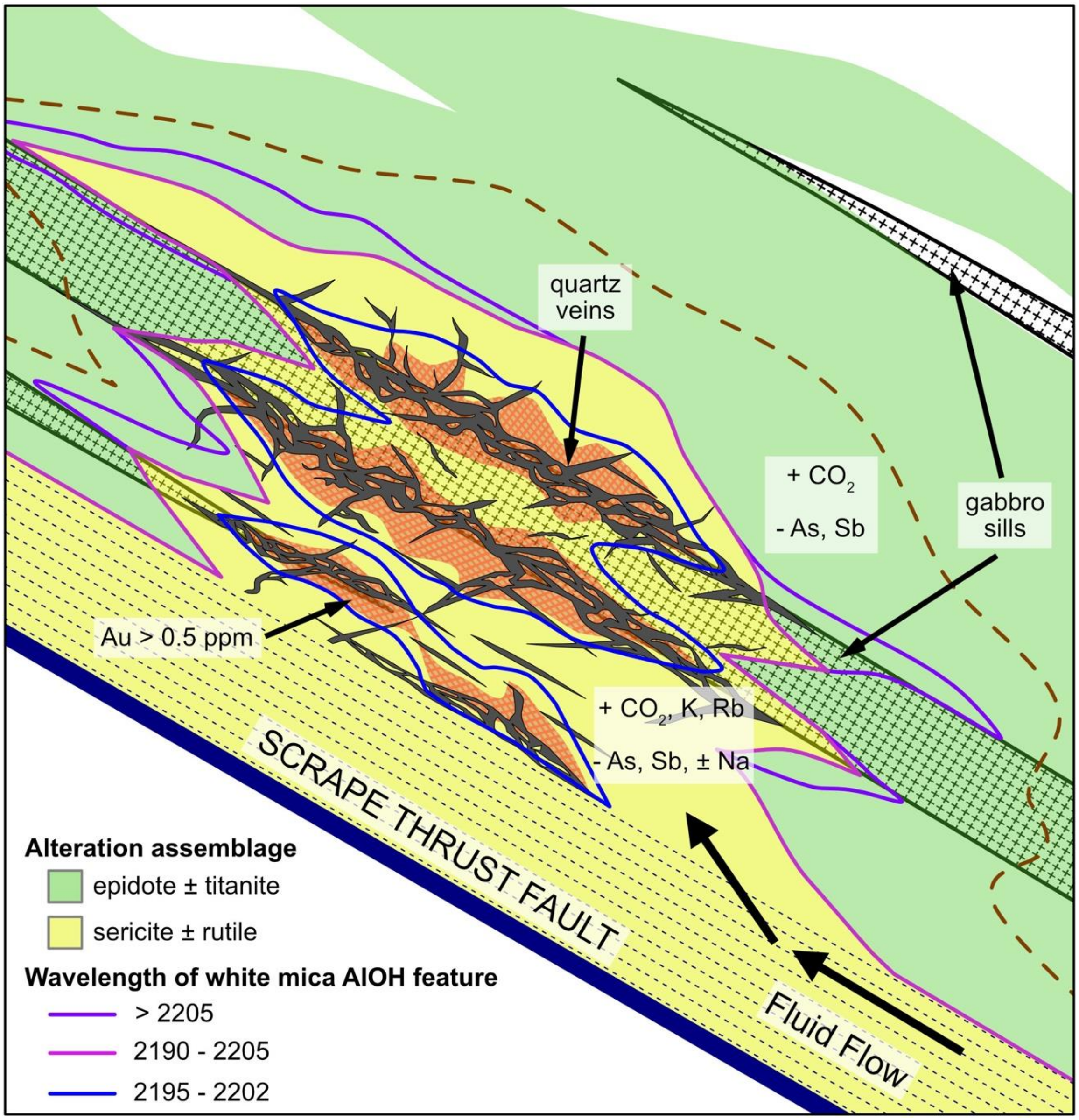

Figure 2.23. Schematic changes in predominant hydrothermal alteration assemblages, pathfinder elements, and SWIR white mica absorption wavelengths at Pine Cove. Not to scale.

Chapter 3: Summary and Future Research

3.1 Summary

This thesis has documented a multi-method examination of the Pine Cove gold deposit in the Baie Verte Peninsula, Newfoundland, Canada. The past-producing Pine Cove gold mine provides an ideal location to better understand productive orogenic gold systems on the Baie Verte Peninsula and elsewhere in the Appalachian-Caledonide orogen. Integrated core logging, geologic mapping, lithogeochemistry, petrography, electron microprobe analysis, and hyperspectral data provide descriptive and genetic insights to alteration and mineralization processes at Pine Cove. Furthermore, these new data provide mineralogical, geochemical, and hyperspectral criteria useful for exploration targeting and evaluation. The major conclusions from this study are as follows:

1) the Pine Cove deposit is predominantly hosted within high Fe-Ti basalts of the Venam's Bight Formation and gabbro sills of the Snooks Arm Group, with lesser mineralization occurring within sedimentary units of the Bobby Cove Formation;
2) the lithogeochemistry of the Venam's Bight Formation, internal stratigraphy of the Bobby Cove Formation, and inverse-graded beds in the greywacke of the Bobby Cove Formation indicate that the stratigraphic sequence at Pine Cove is overturned;
3) gold mineralization occurs as microscopic inclusions within micro-fractured pyrite in sericite-rutile-calcite-chlorite±albite altered wall rock around quartz veins emplaced along lithologic contacts in the hanging wall of the Scrape thrust fault;

4) gold deposition and auriferous pyrite mineralization was driven by both: a) sulfidation of Fe-rich gabbros and basalts; and b) hydrofracturing assisted by anisotropic deformation of rigid gabbro sills within surrounding volcano-sedimentary rocks;
5) the Pine Cove deposit contains three alteration assemblages: proximal sericite-rutile-chlorite-calcite (1 to 25 m extent), intermediate carbonate-chlorite (0 to 25 m extent), and distal epidote-titanite-chlorite-calcite (1 to >50 m extent);
6) mass balance calculations for altered wall rock show enrichments in CO_2, K_2O, S, Rb, W, In, Pb, Bi, Te, Se, Cs, and Ba, and depletions in As, Sb, and Na_2O. Depletion of As and Sb, albeit at very low concentrations, is atypical of orogenic gold systems, and may be unique to Pine Cove and possibly other gold deposits in the Baie Verte Peninsula;
7) combined short wave infrared (SWIR) spectrometry and electron microprobe analysis (EMPA) of white micas show that Tschermak substitution ($Al^{VI} + Al^{IV} \leftrightarrow [Fe^{2+},Mg]^{VI} + Si^{IV}$) and K/Na content correlate with AlOH absorption wavelengths. White mica compositions, as measured by the wavelength position of the AlOH absorption feature, progress from phengite (>2205 nm) → paragonitic muscovite (2190 – 2205 nm) → muscovite (2195 – 2202 nm) approaching mineralization; and
8) a new potential SWIR index for orogenic gold exploration in greenschist facies rocks is the Fe^{2+} slope/MgOH-depth. At Pine Cove, this index measures the relative proportion of (Fe-carbonate + sericite)/chlorite, and correlates with the

alkali-carbonate alteration index $K_2O + CO_2/K_2O + CO_2 + Na_2O + Al_2O_3$ and Au mineralization.

3.2 Future Research

Although this research provides a detailed examination of the lithostratigraphy and alteration footprint of the Pine Cove deposit, there is still additional work that could further our understanding of the ore-forming processes and better define exploration vectors in the Baie Verte Peninsula. Recommended areas of interest for future work include:

1) a detailed study to determine the main sources of mineralizing fluids using mass balance, mineralogy, and thermodynamic modeling could help constrain the predicted occurrence of productive gold systems in the Baie Verte Peninsula. Assuming a metamorphic devolatization model for the source of fluids, mineralization was likely sourced from mafic and ultramafic rocks of the stratigraphically-lower Betts Cove ophiolite. Alternatively, metamorphism of the amphibolite in the footwall of the Scrape thrust fault may have contributed mineralizing fluids, presenting a unique case where post-mineral deformation has resulted in mineralization being juxtaposed immediately above source rocks. Testing the source of mineralizing fluids should focus on the roots of the Betts Cove ophiolite and the amphibolites in the footwall of the Scrape thrust;
2) the character and extent of the distal epidote-chlorite-titanite assemblage is not fully constrained at Pine Cove. This assemblage is common in greenschist-

grade metamorphic rocks, and therefore difficult to distinguish from hydrothermal alteration associated with gold mineralization. Although SWIR data from chlorite and epidote did not yield vectors at Pine Cove, additional EMPA and hyperspectral studies of chlorite ± epidote from similar deposits may delineate systematic changes in the composition of these minerals with distance from mineralization.

3) this study shows that As and Sb are depleted in rocks during alteration and mineralization at Pine Cove. This depletion is atypical of orogenic gold systems, but may be a useful exploration criteria for other gold deposits in the Baie Verte Peninsula. Due to low background concentrations of As and Sb in the host rocks, the minerals involved in this chemical process were not identified in this study. A targeted examination of possible As-Sb bearing phases in altered and unaltered rocks at Pine Cove, coupled with comparisons to nearby deposits, could help refine the application of As-Sb depletion as a potential geochemical vector; and
4) the Fe-slope/MgOH-depth index may be a useful metric for combined carbonate+sericite alteration in greenschist facies rocks; however, further studies are warranted to demonstrate the reliability of this index. A comparison with nearby orogenic gold deposits in the Baie Verte Peninsula, and globally, could show whether this index is applicable to other deposits.

References

Anaconda Mining Inc. https://www.anacondamining.com/pine-cove-mine-mill (Accessed: 21 August 2018).

Abzalov, M. (2008). Quality control of assay data: a review of procedures for measuring and monitoring precision and accuracy. Exploration and Mining Geology, 17(3-4), 131-144.

Anderson, S. D., Jamieson, R. A., Reynolds, P. H., & Dunning, G. R. (2001). Devonian Extension in Northwestern Newfoundland: 40Ar/39Ar and U-Pb Data from the Ming's Bight Area, Baie Verte Peninsula. The Journal of Geology, 109(2), 191-211.

AusSpec International, 2008, Spectral Interpretation Field Manual: GMEX, Edition 3, Volumes 1-10.

Barrett, T. J., Dawson, G. L., & MacLean, W. H. (2008). Volcanic stratigraphy, alteration, and sea-floor setting of the Paleozoic Feitais massive sulfide deposit, Aljustrel, Portugal. Economic Geology, 103(1), 215-239.

Bédard, J. H. (2000). Betts Cove ophiolite and its cover rocks, Newfoundland. Geological Survey of Canada, Bulletin 550, 76 pages.

Bierlein, F.P., Arne, D.C., McKnight, S., Lu, J., Reeves, S., Besanko, J., Marek, J. and Cooke, D. (2000). Wall-rock petrology and geochemistry in alteration halos associated with mesothermal gold mineralization, central Victoria, Australia. Economic Geology, 95(2), 283-311.

Bierwirth, P., Huston, D., & Blewett, R. (2002). Hyperspectral mapping of mineral assemblages associated with gold mineralization in the Central Pilbara, Western Australia. Economic Geology, 97(4), 819-826.

Buschette, M. J., & Piercey, S. J. (2016). Hydrothermal alteration and lithogeochemistry of the Boundary volcanogenic massive sulphide deposit, central Newfoundland, Canada. Canadian Journal of Earth Sciences, 53(5), 506-527.

Calon, T.J. and Weike, J. (1990). Structural study on the Pine Cove area. Structural evolution of the Pine Cove gold deposit. Preliminary report of a detailed structural analysis on behalf of Corona Corporation. Unpublished internal report to Corona Corporation, 25 pages.

Carranza, E. J. M. (2011). Analysis and mapping of geochemical anomalies using logratio-transformed stream sediment data with censored values. Journal of Geochemical Exploration, 110(2), 167-185.

Castonguay, S., Skulski, T., van Staal, C., & Currie, M. (2009). New insights on the structural geology of the Pacquet Harbour group and Point Rousse complex, Baie Verte peninsula, Newfoundland. Current Research, Newfoundland and Labrador Department of Natural Resources, Geological Survey, Report 09-1, 147-158.

Castonguay, S., van Staal, C. R., Joyce, N., Skulski, T., & Hibbard, J. P. (2014). Taconic Metamorphism Preserved in the Baie Verte Peninsula, Newfoundland Appalachians: Geochronological Evidence for Ophiolite Obduction and Subduction and Exhumation of the Leading Edge of the Laurentian (Humber) Margin During Closure of the Taconic Seaway. Geoscience Canada, 41(4), 459-482.

Christie, A. B., & Brathwaite, R. L. (2003). Hydrothermal alteration in metasedimentary rock-hosted orogenic gold deposits, Reefton goldfield, South Island, New Zealand. Mineralium Deposita, 38(1), 87-107.

Clark, R. N., King, T. V., Klejwa, M., Swayze, G. A., & Vergo, N. (1990). High spectral resolution reflectance spectroscopy of minerals. Journal of Geophysical Research: Solid Earth, 95(B8), 12653-12680.

Cousineau, P. A., & Bédard, J. H. (2000). Sedimentation in a subaqueous arc/back-arc setting: the Bobby Cove Formation, Snooks Arms Group, Newfoundland. Precambrian Research, 101(2-4), 111-134.

Dimmell, P., & Hartley, C. (1991). Gold Mineralization and Exploration Potential of the Pine Cove Property, Baie Verte Peninsula. Ore Horizons, 1, 51-62.

Dinel, E., Fowler, A. D., Ayer, J., Still, A., Tylee, K., & Barr, E. (2008). Lithogeochemical and stratigraphic controls on gold mineralization within the metavolcanic rocks of the Hoyle Pond mine, Timmins, Ontario. Economic Geology, 103(6), 1341-1363.

Dubé, B., Lauzière, K., & Poulsen, H. K. (1993). The Deer Cove deposit: an example of "thrust"-related breccia-vein type gold mineralization in the Baie Verte Peninsula, Newfoundland. Current Research, Part D; Geological Survey of Canada, Paper 93-1D, 1-10.

Dube, B., & Gosselin, P. (2007). Greenstone-Hosted Quartz-Carbonate Vein Deposits. Mineral Deposits of Canada: A synthesis of major deposit-types, district metallogeny, the evolution of geological provinces, and exploration methods: Geological Association of Canada, Mineral Deposits Division, Special Publication 5, 49-73.

Duke, E. F. (1994). Near infrared spectra of muscovite, Tschermak substitution, and metamorphic reaction progress: Implications for remote sensing. Geology, 22(7), 621-624.

Duncan, D.R. and Graves, R.M. (1992). 1992 Assessment Report (7th year work), Geology and diamond drilling on the Pine Cove property Baie Verte Peninsula, Newfoundland. Unpublished report to Novagold Resources Inc., Newfoundland Department of Mines and Energy, Geological Survey, 012H/16/1278, 43 pages.

Dunning, G. R., O'Brien, S. J., Colman-Sadd, S. P., Blackwood, R. F., Dickson, W. L., O'Neill, P. P., and Krogh, T. E. (1990). Silurian Orogeny in the Newfoundland Appalachians, The Journal of Geology, 98(6):895-913.

Eilu, P., & Mikucki, E. J. (1998). Alteration and primary geochemical dispersion associated with the Bulletin lode-gold deposit, Wiluna, Western Australia. Journal of Geochemical Exploration, 63(2), 73-103.

Eilu, P., & Groves, D. I. (2001). Primary alteration and geochemical dispersion haloes of Archaean orogenic gold deposits in the Yilgarn Craton: the pre-weathering scenario. Geochemistry: Exploration, Environment, Analysis, 1(3), 183-200.

Eilu, P., Mikucki, E. J., & Dugdale, A. L. (2001). Alteration zoning and primary geochemical dispersion at the Bronzewing lode-gold deposit, Western Australia. Mineralium Deposita, 36(1), 13-31.

Evans, D.T.W. (2004). Epigenetic gold occurrences, Baie Verte Peninsula, (NTS 12H/09, 16 and 12I/01), Newfoundland. Government of Newfoundland and Labrador, Department of Natural Resources, Geological Survey. Mineral Resource Report #11, 157 pages.

Gaffey, S. J. (1986). Spectral reflectance of carbonate minerals in the visible and near infrared (O. 35-2.55 microns); calcite, aragonite, and dolomite. American Mineralogist, 71(1-2), 151-162.

Gaffey, S. J. (1987). Spectral reflectance of carbonate minerals in the visible and near infrared (0.35–2.55 um): Anhydrous carbonate minerals. Journal of Geophysical Research: Solid Earth, 92(B2), 1429-1440.

Gao, Z. L., & Kwak, T. A. P. (1997). The geochemistry of wall rock alteration in turbidite-hosted gold vein deposits, central Victoria, Australia. Journal of Geochemical Exploration, 59(3), 259-274.

Goldfarb, R. J., Groves, D. I., & Gardoll, S. (2001). Orogenic gold and geologic time: a global synthesis. Ore Geology Reviews, 18(1-2), 1-75.

Groves, D. I., Goldfarb, R. J., Gebre-Mariam, M., Hagemann, S. G., & Robert, F. (1998). Orogenic gold deposits: a proposed classification in the context of their crustal distribution and relationship to other gold deposit types. Ore Geology Reviews, 13(1), 7-27.

Halley, S., Dilles, J. H., & Tosdal, R. M. (1999). Footprints: Hydrothermal Alteration and Geochemical Dispersion Around Porphyry Copper Deposits. SEG Newsletter, 100, 12-17.

Herrmann, W., Blake, M., Doyle, M., Huston, D., Kamprad, J., Merry, N., & Pontual, S. (2001). Short wavelength infrared (SWIR) spectral analysis of hydrothermal alteration zones associated with base metal sulfide deposits at Rosebery and Western Tharsis, Tasmania, and Highway-Reward, Queensland. Economic Geology, 96(5), 939-955.

Henley, K. J. (1970). Application of the muscovite-paragonite geothermometer to a staurolite-grade schist from Sulitjelma, north Norway. Mineralogical Magazine, 37(290), 693-704.

Hibbard, J. (1983). Geology of the Baie Verte Peninsula, Newfoundland. Mineral Development Division, Department of Mines and Energy, Government of Newfoundland and Labrador. Memoir 2, 279 pages.

Humphris, S. E., & Thompson, G. (1978). Trace element mobility during hydrothermal alteration of oceanic basalts. *Geochimica et Cosmochimica Acta*, *42*(1), 127-136.

Hynes, A. (1980). Carbonatization and mobility of Ti, Y, and Zr in Ascot Formation metabasalts, SE Quebec. Contributions to Mineralogy and Petrology, 75(1), 79-87.

Murphy, J. B., & Hynes, A. J. (1986). Contrasting secondary mobility of Ti, P, Zr, Nb, and Y in two metabasaltic suites in the Appalachians. Canadian Journal of Earth Sciences, 23(8), 1138-1144.

Jenner, G. A. (1996). Trace element geochemistry of igneous rocks: geochemical nomenclature and analytical geochemistry. In: Wyman, D.A. (ed.), Trace element geochemistry of volcanic rocks: applications for massive sulfide exploration. Geological Association of Canada, Short Course Notes, 12, 51-77, St. John's, NL, Canada.

Jensen, L. S. (1976). A New Cation Plot for Classifying Subalkalic Volcanic Rocks. Ontario Division of Mines, Ministry of Natural Resources, Miscellaneous Paper 66, 22 pages.

Kerr, A., & Selby, D. (2012). The timing of epigenetic gold mineralization on the Baie Verte Peninsula, Newfoundland, Canada: new evidence from Re–Os pyrite geochronology. Mineralium Deposita, 47(3), 325-337.

Kessler, L. G., & Bédard, J. H. (2000). Epiclastic volcanic debrites-evidence of flow transformations between avalanche and debris flow processes, Middle Ordovician, Baie Verte Peninsula, Newfoundland, Canada. Precambrian Research, 101(2-4), 135-161.

Kishida, A., & Kerrich, R. (1987). Hydrothermal alteration zoning and gold concentration at the Kerr-Addison Archean lode gold deposit, Kirkland Lake, Ontario. Economic Geology, 82(3), 649-690.

MacLean, W. H. (1990). Mass change calculations in altered rock series. Mineralium Deposita, 25(1), 44-49.

MacLean, W. H., & Kranidiotis, P. (1987). Immobile elements as monitors of mass transfer in hydrothermal alteration; Phelps Dodge massive sulfide deposit, Matagami, Quebec. Economic Geology, 82(4), 951-962.

MacLean, W. H., & Barrett, T. J. (1993). Lithogeochemical techniques using immobile elements. Journal of Geochemical Exploration, 48(2), 109-133.

McCuaig, T. C., & Kerrich, R. (1998). P—T—t—deformation—fluid characteristics of lode gold deposits: evidence from alteration systematics. Ore Geology Reviews, 12(6), 381-453.

Meade, J., Evans, D. T. W., & Wilton, D. H. C. (1998). Romeo and Juliet Prospect, Baie Verte Peninsula, Newfoundland. Current Research, Newfoundland Department of Mines and Energy, Geological Survey, Report 98-1, 77-83.

Mernagh, T. P., & Bierlein, F. P. (2008). Transport and precipitation of gold in Phanerozoic metamorphic terranes from chemical modeling of fluid-rock interaction. Economic Geology, 103(8), 1613-1640.

Mikucki, E. J. (1998). Hydrothermal transport and depositional processes in Archean lode-gold systems: a review. Ore Geology Reviews, 13(1), 307-321.

Patey, K. S., & Wilton, D. H. (1993). The Deer Cove deposit, Baie Verte Peninsula, Newfoundland, a Paleozoic mesothermal lode-gold occurrence in the northern Appalachians. Canadian Journal of Earth Sciences, 30(7), 1532-1546.

Phillips, G. N., Groves, D. I., & Kerrich, R. (1996). Factors in the formation of the giant Kalgoorlie gold deposit. Ore Geology Reviews, 10(3-6), 295-317.

Phillips, G. N., & Powell, R. (2010). Formation of gold deposits: a metamorphic devolatilization model. Journal of Metamorphic Geology, 28(6), 689-718.

Piercey, S. J. (2014). Modern Analytical Facilities 2. A review of quality assurance and quality control (QA/QC) procedures for lithogeochemical data. Geoscience Canada, 41(1), 75-88.

Pitcairn, I. K., Teagle, D. A., Craw, D., Olivo, G. R., Kerrich, R., & Brewer, T. S. (2006). Sources of metals and fluids in orogenic gold deposits: insights from the Otago and Alpine Schists, New Zealand. Economic Geology, 101(8), 1525-1546.

Pitcairn, I. K., Craw, D., & Teagle, D. A. (2015). Metabasalts as sources of metals in orogenic gold deposits. Mineralium Deposita, 50(3), 373-390.

Ramezani, J., Dunning, G. R., & Wilson, M. R. (2000). Geologic setting, geochemistry of alteration, and U-Pb age of hydrothermal zircon from the Silurian Stog'er Tight gold prospect, Newfoundland Appalachians, Canada. Exploration and Mining Geology, 9(3-4), 171-188.

Ridley, J. (1993). The relations between mean rock stress and fluid flow in the crust: with reference to vein-and lode-style gold deposits. Ore Geology Reviews, 8(1-2), 23-37.

Ritcey, D. H., Wilson, M. R., & Dunning, G. R. (1995). Gold mineralization in the Paleozoic Appalachian Orogen; constraints from geologic, U/Pb, and stable isotope studies of the Hammer Down Prospect, Newfoundland. Economic Geology, 90(7), 1955-1965.

Ropchan, J. R., Luinstra, B., Fowler, A. D., Benn, K., Ayer, J., Berger, B., ... & Amelin, Y. (2002). Host-rock and structural controls on the nature and timing of gold mineralization at the Holloway mine, Abitibi subprovince, Ontario. Economic Geology, 97(2), 291-309.

Ross, P. S., & Bédard, J. H. (2009). Magmatic affinity of modern and ancient subalkaline volcanic rocks determined from trace-element discriminant diagrams. Canadian Journal of Earth Sciences, 46(11), 823-839.

Sanford, R. F., Pierson, C. T., & Crovelli, R. A. (1993). An objective replacement method for censored geochemical data. Mathematical Geology, 25(1), 59-80.

Skulski, T., Castonguay, S., van Staal, C. R., Rogers, N., McNicoll, V., Kerr, A., & Escayola, M. (2009). Baie Verte Peninsula: an evolving geological story. Geological

Association of Canada, Newfoundland and Labrador Section Annual Fall Field Trip Guide. Geological Association of Canada, 60 pages.

Skulski, T., Castonguay, S., McNicoll, V., van Staal, C., Kidd, W., Rogers, N., Morris, W., Ugalde, H., Slavinski, H., Spicer, W. and Moussallam, Y. (2010). Tectonostratigraphy of the Baie Verte oceanic tract and its ophiolite cover sequence on the Baie Verte Peninsula. Current Research, Newfoundland and Labrador Department of Natural Resources, Geological Survey, Report 10-1, 315-337.

Skulski, T., Castonguay, S., Côté, N., McNicoll, V.J., Currie, M., Magee, A., Harris, B., and van Staal, C.R. (2017). Digital geoscience atlas of Baie Verte Peninsula, Newfoundland and Labrador. Geological Survey of Canada, Open File 7342, 1 .zip file. doi:10.4095/298754

Sun, S. S., & McDonough, W. S. (1989). Chemical and isotopic systematics of oceanic basalts: implications for mantle composition and processes. Geological Society, London, Special Publications, 42(1), 313-345.

Thompson, A. J., Hauff, P. L., & Robitaille, A. J. (1999). Alteration mapping in exploration: application of short-wave infrared (SWIR) spectroscopy. SEG Newsletter, 39:16-27.

van Staal, C. R. (2007). Pre-Carboniferous tectonic evolution and metallogeny of the Canadian Appalachians. Mineral deposits of Canada: a synthesis of major deposit-types, district metallogeny, the evolution of geological provinces, and exploration methods. Edited by WD Goodfellow. Geological Association of Canada, Mineral Deposits Division, Special Publication, (5), 793-818.

van Staal, C. R., & Barr, S. M. (2012). Lithospheric architecture and tectonic evolution of the Canadian Appalachians and associated Atlantic margin. Tectonic Styles in Canada: The LITHOPROBE perspective. Edited by JA Percival, FA Cook, and RM Clowes. Geological Association of Canada, Special Paper, 49, 55.

Wang, R., Cudahy, T., Laukamp, C., Walshe, J.L., Bath, A., Mei, Y., Young, C., Roache, T.J., Jenkins, A., Roberts, M. and Barker, A. (2017). White Mica as a Hyperspectral Tool in Exploration for the Sunrise Dam and Kanowna Belle Gold Deposits, Western Australia. Economic Geology, 112(5), 1153-1176.

Weatherley, D. K., & Henley, R. W. (2013). Flash vaporization during earthquakes evidenced by gold deposits. Nature Geoscience, 6(4), 294.

Williams, H. (1979). Appalachian orogen in Canada. Canadian Journal of Earth Sciences, 16(3), 792-807.

Williams, H., & St-Julien, P. (1982). The Baie Verte-Brompton Line: Early Paleozoic continent-ocean interface in the Canadian Appalachians. In Major structural zones and faults of the northern Appalachians. Edited by P. St-Julien and J. Bédard. Geological Association of Canada, Special Paper 24: 177-208.

Williams-Jones, A. E., Bowell, R. J., & Migdisov, A. A. (2009). Gold in solution. Elements, 5(5), 281-287.

Witt, W. K. (1993). Lithological and structural controls on gold mineralization in the Archaean Menzies-Kambalda area, Western Australia. Australian Journal of Earth Sciences, 40(1), 65-86.

Yang, K., Huntington, J. F., Gemmell, J. B., & Scott, K. M. (2011). Variations in composition and abundance of white mica in the hydrothermal alteration system at Hellyer, Tasmania, as revealed by infrared reflectance spectroscopy. Journal of Geochemical Exploration, 108(2), 143-156.

Zoheir, B., & Emam, A. (2012). Integrating geologic and satellite imagery data for high-resolution mapping and gold exploration targets in the South Eastern Desert, Egypt. Journal of African Earth Sciences, 66, 22-34.